NASA/TM-20250008885

Turbulent Shock-Wave/Boundary-Layer Interactions Without Sidewall Effects at Mach 2.5, 3.0, and 3.5—PIV Measurements From 2025 Test Entry

Heath H. Reising
Glenn Research Center, Cleveland, Ohio

September 2025

NASA STI Program Report Series

Since its founding, NASA has been dedicated to the advancement of aeronautics and space science. The NASA scientific and technical information (STI) program plays a key part in helping NASA maintain this important role.

The NASA STI program operates under the auspices of the Agency Chief Information Officer. It collects, organizes, provides for archiving, and disseminates NASA's STI. The NASA STI program provides access to the NTRS Registered and its public interface, the NASA Technical Reports Server, thus providing one of the largest collections of aeronautical and space science STI in the world. Results are published in both non-NASA channels and by NASA in the NASA STI Report Series, which includes the following report types:

- TECHNICAL PUBLICATION.
  Reports of completed research or a major significant phase of research that present the results of NASA programs and include extensive data or theoretical analysis. Includes compilations of significant scientific and technical data and information deemed to be of continuing reference value. NASA counterpart of peer-reviewed formal professional papers but has less stringent limitations on manuscript length and extent of graphic presentations.

- TECHNICAL MEMORANDUM.
  Scientific and technical findings that are preliminary or of specialized interest, e.g., quick release reports, working papers, and bibliographies that contain minimal annotation. Does not contain extensive analysis.

- CONTRACTOR REPORT.
  Scientific and technical findings by NASA-sponsored contractors and grantees.

- CONFERENCE PUBLICATION.
  Collected papers from scientific and technical conferences, symposia, seminars, or other meetings sponsored or cosponsored by NASA.

- SPECIAL PUBLICATION.
  Scientific, technical, or historical information from NASA programs, projects, and missions, often concerned with subjects having substantial public interest.

- TECHNICAL TRANSLATION.
  English-language translations of foreign scientific and technical material pertinent to NASA's mission.

Specialized services also include organizing and publishing research results, distributing specialized research announcements and feeds, providing information desk and personal search support, and enabling data exchange services.

For more information about the NASA STI program, see the following:

- Access the NASA STI program home page at http://www.sti.nasa.gov

NASA/TM-20250008885

Turbulent Shock-Wave/Boundary-Layer Interactions Without Sidewall Effects at Mach 2.5, 3.0, and 3.5—PIV Measurements From 2025 Test Entry

Heath H. Reising
Glenn Research Center, Cleveland, Ohio

National Aeronautics and
Space Administration

Glenn Research Center
Cleveland, Ohio 44135

September 2025

Acknowledgments

Support for this work was provided by NASA's Transformative Aeronautics Concepts Program through the Transformational Tools & Technologies (T^3) Project. These tests were facilitated by the tireless work of the facility staff. The assistance provided by Jason Bryant, Molly Fenik, John Friscat, Celia Otero, and Brent Seifert is gratefully acknowledged. Conceptualization of the axisymmetric configuration and implementation in the 225 cm^2 Wind Tunnel is credited to David Davis, who provided invaluable support in the planning and execution of the PIV measurements.

This work was sponsored by the
Transformative Aeronautics Concepts Program.

Level of Review: This material has been technically reviewed by technical management.

This report is available in electronic form at https://www.sti.nasa.gov/ and https://ntrs.nasa.gov/

NASA STI Program/Mail Stop 050
NASA Langley Research Center
Hampton, VA 23681-2199

Turbulent Shock-Wave/Boundary-Layer Interactions Without Sidewall Effects at Mach 2.5, 3.0, and 3.5 — PIV Measurements From 2025 Test Entry

Heath H. Reising
National Aeronautics and Space Administration
Glenn Research Center
Cleveland, Ohio 44135

Abstract

The High-Mach Validation Experiments (HMVE) campaign was initiated as a follow-on to shock-wave/boundary-layer interaction (SWBLI) experiments previously completed in the NASA GRC 225 cm^2 Wind Tunnel at a freestream Mach number of 2.5. Data were collected at Mach 3.0 and 3.5 freestream conditions using the same set of three angles for the conical shock generators in the axisymmetric test section. Select cases from Mach 2.5 testing were also duplicated to verify repeatability. Particle image velocimetry (PIV) measurements were applied to collect large ensembles of velocity data which were stitched together to form a quasi-continuous view of the mean and turbulent flowfield behavior. Densely-spaced wall pressure measurements were concurrently acquired to supplement the flowfield information from PIV. The primary purpose of this report is to summarize the data obtained in this entry and assess the quality and repeatability relative to previous entries. Herein, velocity data is visualized component-by-component in contour plot form to visually assess the ability of the PIV technique to capture detailed flow features. Shock-fitting is used to quantify and correct for small displacements in the shock generator tip which occur due to the long cantilevered support. Since the novelty of this entry comes from the addition of new test cases at reduced Reynolds number, results are presented in a fashion which highlights trends in the flowfield behavior with variation in that parameter. Slices at select streamwise stations are extracted and compared quantitatively across test conditions to identify trends. Data files containing wall-normal profiles of each measured quantity at spacing which matches the companion probe measurements are attached to this report for wider use in comparisons.

Nomenclature

c_f = boundary layer friction coefficient
ℓ = shock generator offset distance from test section axis
M = Mach number
P = pressure
r = radial coordinate
R_{TS} = test section radius, 8.5 cm
Re_D = core flow Reynolds number based on test section hydraulic diameter
Re_{δ_2} = boundary layer characteristic Reynolds number using wall viscosity, $\frac{\overline{u}_\infty \theta}{\nu_w}$
u = axial velocity (aligned with $\vec{x}$)
u_τ = turbulent boundary layer friction velocity
v = vertical velocity (aligned with $\vec{y}$)
w = spanwise velocity (aligned with $\vec{z}$)
x = axial coordinate, $x = 0$ at leading edge of test section
y = vertical coordinate, $y = 0$ on test section axis
$\overline{y}$ = wall-normal coordinate, $\overline{y} = 0$ at $(r, \theta) = (R_{TS}, 180°)$
z = spanwise coordinate, $z = 0$ on test section axis
α = shock generator cone half-angle

β = shock wave angle
$\delta_{99.5}$ = boundary layer thickness based on $\overline{y}(\overline{u} = 0.995\overline{u}_\infty)$
δ^* = boundary layer displacement thickness
δ_v = turbulent boundary layer viscous scale, $\frac{\mu_w}{\rho_w} u_\tau$
Δ = Rotta-Clauser integral boundary layer thickness
θ = boundary layer momentum thickness or azimuth in cylindrical coordinate system, $\theta = 0$ at 12 o'clock and is clockwise positive looking upstream
ρ = density

Subscripts

i = inviscid shock impingement
w = wall

Special Notations

0 = facility nozzle exit station
1 = station at which incoming boundary layer is evaluated
∞ = freestream or boundary layer edge
$\overline{(\ )}$ = time average (Reynolds average)
$(\ )'$ = deviation of instantaneous value from the time average
$(\ )^*$ = van Driest transform

I. Introduction

Validation of turbulence models is paramount in the pursuit of accurate computational fluid dynamics (CFD) predictions in the complex flowfields present in realistic aerospace vehicle and propulsion designs. Typically, methods which rely on modeling of the more complex fluid physics (e.g. Reynolds stresses and heat flux vectors in Reynolds-averaged Navier-Stokes (RANS) simulations) are less expensive than scale-resolving methods such as Large-Eddy Simulation (LES) and can be used in parametric optimization studies. However, the models used within these lower-fidelity methods are almost universally calibrated in equilibrium turbulence and require careful tuning to accurately predict the production, transport, and dissipation of turbulence in complex flowfields. Shock-wave/boundary-layer interactions (SWBLI) are typically identified as a problematic case for RANS solvers due to their large departure from an equilibrium turbulence state[1].

A dearth of high quality experimental data in supersonic and hypersonic shock-wave/boundary-layer interactions for use in code validation efforts was identified by Settles and Dodson [2]. There, many of the candidate datasets were rejected due to the lack of well-defined boundary conditions, undocumented 3D effects, inconsistency between repeated measurements, or a lack of repeated measurements. A specific methodology was laid out in Ref. 3 for planning useful CFD code validation experiments which acknowledges the interdependency between the requirements and capabilities of experimental and computational results.

In addition to the overall lack of high-quality experimental data, the influence of the glancing sidewall interaction is commingled with many nominally 2D SWBLI datasets. References 4 and 5 show just two examples where blockage generated by corner separations influence the strength of the primary SWBLI. Thus, the current campaign aims to use an axisymmetric wind tunnel test section and shock generator cone to circumvent this issue.

The High-Mach Validation Experiments (HMVE) are a follow-on to the Turbulent Computational Fluid Dynamics Validation Experiment (TCFDVE) campaign which was reported on in several papers [6–10]. These test entries comprise an ongoing effort funded by the Transformation Tools and Technologies project at NASA Glenn Research Center (GRC) to provide a high-quality experimental dataset of a SWBLI which is free of sidewall effects. A key component of a high-quality CFD validation dataset is the corroboration of a multitude of independent redundant measurements. This manuscript extends upon the previously reported results by exploring interactions at increased freestream Mach number.

II. Apparatus and Procedure

This report provides a complete summary of the particle image velocimetry (PIV) data collected in the test campaign completed in February and March of 2025 as part of the High-Mach Validation Experiments. PIV measurements were performed in the NASA Glenn Research Center 225 cm^2 Wind Tunnel. A schematic of the flowfield being studied

is shown in Fig. 1. Simple cone-cylinder bodies were used to generate the initial shock wave which impinges on the naturally-occurring test section wall boundary layer. This provides a relatively thick profile in which to perform the detailed measurements required. The cone half-angle, α, was varied to provide both unseparated and separated interactions.

Figure 1 also gives a pictorial reference for the coordinate system and nomenclature used throughout this manuscript. Spatial coordinate are shown in both Cartesian (gray) and cylindrical (blue) systems to connect between the measurements and the axisymmetric geometry. While x is indicated to reference from the test section leading edge, the data is presented relative to the location of the inviscid shock impingement station near $x = 19.5$". The directions for the defined velocity components which align with the typical convention for Cartesian coordinates are represented in green.

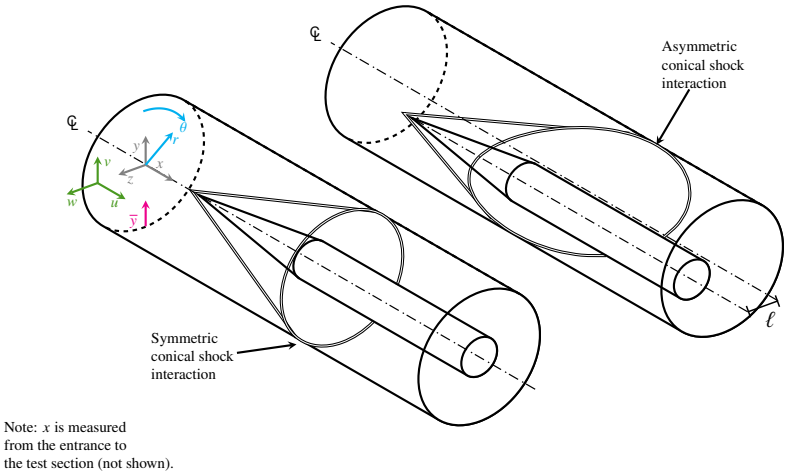

Fig. 1 Basic geometry and coordinate systems.

A. Test Facility

For the test results presented herein, the tunnel was configured with its axisymmetric 17 cm diameter test section and one of three converging-diverging nozzles: Mach 2.5, 3.0, or 3.5. The wind tunnel and the specific test section geometry used for this test has been described thoroughly in Refs. 6–9.

The cone-cylinder centerbodies used to generate the impinging shock waves were highly configurable. Three tip cone half-angles were available to generate interactions of various strengths: 10° for an unseparated interaction, 13.5° for incipient separation, and 16° for a fully separated interaction. Typically, the cylindrical portion of the body was 5 cm in diameter and was comprised of a collection of spacer pieces to generate the desired axial length. A specific length of spacer stack was selected for each cone angle and Mach number to place the inviscid impingement at approximately the same axial station, with one key exception: for the current HMVE campaign, a larger version of the $\alpha = 16°$ cone was fabricated which continued the conical expansion out to a 6 cm diameter in an attempt to increase the compression length at the wall. This part contained the same length of cylindrical section as the smaller diameter version, resulting in the cone tip residing in a more forward position when using the same set of spacers. Thus, the inviscid impingement station for the $\alpha = 16°$ cases at Mach 3.0 and 3.5 are shifted forward in the test section by 17.44 mm.

The cone-cylinders were cantilevered from a support strut spanning the aft end of the section. This strut had a sharp leading edge to reduce blockage and, thus, lower the minimum Reynolds number condition available for testing. Three mounting positions are available on the strut. A centerline position allows for the generation of an axisymmetric interaction (left side of Fig. 1) while two offset positions generate swept interactions at distance ℓ from the tunnel axis (right side of Fig. 1). The near-wall measurements were made at the $\theta = 180°$ position. Thus, a secondary vertical coordinate, $\overline{y} = y + R_{TS}$, is defined (magenta in Fig. 1) which aligns the presented data with typical wall-referenced coordinates used when presenting boundary layer data.

The axisymmetric cases require sampling only in one x-r plane to fully describe the flowfield. The probe-based measurements took advantage of this feature to reduce the reach required for the probe traversing apparatus. Likewise, this enabled the application of PIV measurement in this facility using a fixed laser sheet position and a local seeding technique. Due to the strong local flow angularity (see Ref. 9), the PIV technique was the only flowfield measurement applied in the swept interactions.

B. Measurement Techniques

The PIV system utilized herein has no notable changes from previous data collection for a Mach 2.5 freestream condition [9]. The design process for the PIV system and the constraints for implementing the technique in this particular facility are described in Ref. 11.

C. Test Parameters

In this entry, PIV data was collected for all 3 conical shock generator tips installed on the tunnel axis to create axisymmetric interactions for each facility nozzle. Additionally, the shock generator was offset to the $\ell = R_{TS}/4$ and $\theta = 90^\circ$ position to study swept interaction for the $\alpha = 16^\circ$ configurations. For each test configuration, the facility total temperature was tightly controlled at (311.0 ± 0.3) K ((100.0 ± 0.5) °F) in order to create a nearly adiabatic condition at the test section walls. This serves two purposes: simplifying the boundary conditions applied in companion CFD calculations and also minimizing the collection of condensation on the exterior of the test section which can occlude the windows through which the PIV cameras view the flowfield. For each fixed-geometry nozzle, the total pressure of the supply air was controlled to maintain specific Reynolds number values at the exit station. These are referred to in terms of test section diameter as Re_D and the specific values at which tests were operated are summarized below in Table 1. As expected, the nozzle Mach number value has very little scatter since it is mostly determined by the nozzle geometry and varies only slightly with total pressure and temperature. These values are known very precisely due to the averaging of 8 pressure measurements made around the nozzle circumference. The Reynolds number condition is set somewhat less precisely since it is more sensitive to fluctuations in the supplied pressure and temperature (both of which are being feedback controlled simultaneously). However, the test conditions are still quite accurate to the intended set point.

For the Mach 2.5 case, the nozzle exit Mach number has a slight sensitivity to Reynolds number. The agreement of the nozzle Mach number with the design value at $Re_D = 4 \times 10^6$ is exemplary of the fact that the CFD simulation used to make the viscous correction to the nozzle contour was performed at that condition. As the nozzle is operated at lower total pressures, the boundary layer at the exit station thickens, thus reducing the Mach number at that station. For the other two nozzles, the behavior is not quite as straightforward. For each, the exit station Mach number closely matches the design value at the higher Reynolds number condition. However, as the Reynolds number is decreased for the Mach 3.0 nozzle, the exit condition is nearly unchanged indicating a relatively unchanged boundary layer displacement. For the Mach 3.5 nozzle, Mach number at the exit station increases at reduced Reynolds number, indicating a reduction in boundary layer scale. This could be symptomatic of a change in the transition location along the nozzle contour and will be checked against the flowfield and wall pressure data in the test section in Section III.

The low Reynolds number conditions were selected such that the blockage sustained in the diffuser by the PIV apparatus does not cause significant incursion of the shock train into the test section. At Mach 2.5, there is significant headroom between a minimum Reynolds number and the capability of the air supply system. However, the latitude between these two limits wanes with increasing Mach number (vacuum pressure is unchanged). The new conditions introduced herein at reduced Reynolds number were selected as the minimum total pressure condition which maintained the mean location of the shock train leading edge at least $3\delta_{99.5}$ downstream of the PIV measurement region.

Table 1 Freestream test conditions.

Nominal		Actual	
$M_{0,\infty}$	$Re_D \times 10^{-6}$	$M_{0,\infty}$	$Re_D \times 10^{-6}$
2.5	1	$2.486 \pm 0.005^{*}(\pm 3.5 \times 10^{-4})^{\dagger}$	1.007 ± 0.032 (± 0.016)
2.5	2	2.494 ± 0.004 ($\pm 1.8 \times 10^{-4}$)	2.002 ± 0.042 (± 0.016)
2.5	4	2.500 ± 0.004 ($\pm 8.8 \times 10^{-5}$)	4.014 ± 0.032 (± 0.016)
3	1	3.003 ± 0.008 ($\pm 6.0 \times 10^{-4}$)	1.008 ± 0.016 (± 0.026)
3	2.25	2.994 ± 0.003 ($\pm 2.7 \times 10^{-4}$)	2.253 ± 0.008 (± 0.026)
3.5	1.5	3.518 ± 0.012 ($\pm 6.8 \times 10^{-4}$)	1.504 ± 0.010 (± 0.042)
3.5	3	3.501 ± 0.008 ($\pm 3.4 \times 10^{-4}$)	3.007 ± 0.014 (± 0.042)

[*] Ranges indicate 2 standard deviation scatter in the values calculated by facility data system simultaneously with PIV data collection.
[†] Values in parentheses indicate the measurement uncertainty bounds (95% confidence) based on instrument accuracy.

III. Results and Discussion

Analysis of the PIV data first requires a precise determination of the wall position within the PIV vector fields. This is obtained by close inspection of the near-wall mean axial velocity and turbulent shear behavior in the incoming boundary layer. Then, the inviscid shock location can be ascertained by tracing the region of peak negative divergence to correct for minor variations in the shock generator position, as described in the following section.

A. Axial Alignment of the Data

As described in Ref. 9, the optical access required for PIV measurements necessitated the inclusion of a longer centerbody to provide enough axial clearance for the cameras to be placed between the region of interest and the flange at the aft end of the test section. Thus, while the test configurations are equivalent from the plenum tank to the interaction, the PIV configuration is more susceptible to misalignment of the cone-cylinder tip due to the longer cantilevered length. Great care was taken to ensure that the centerbody was aligned with the test section pre-test at atmospheric pressure and the methods used were validated in the TCFDVE campaign where very little shifting of the centerbody was observed. However, in the HMVE campaign, a small offset was observed in both the wall pressure and PIV data. This was investigated and reported upon in Ref. 12 in detail. Following the procedure outlined therein for determining the true shock position, axial shifts in the inviscid impingement station were quantified for this dataset from the PIV data. In this entry, a precise wall location was determined from the turbulent shear stress information.

Table 2 summarizes the shifts observed over all the configurations sampled with PIV in this campaign. Typically, the configurations requiring the largest cantilever exhibit the largest shift from the nominal tip location. Since the cone tip station was kept constant between the axisymmetric and swept configurations, there is an aftward shift in the nominal impingement station in the measurement plane of $R_{TS} \cot\beta \sqrt{1 + \frac{\ell}{R_{TS}}}$ which is typically on the order of 5 to 8 mm for the $\ell = R_{TS}/4$ offset over the range of shock angles.

Table 2 Summary of measured inviscid impingement stations, x_i, inferred from PIV data.

		M2.5			M3.0		M3.5	
		Re_D	Re_D	Re_D	Re_D	Re_D	Re_D	Re_D
α	θ	1×10^6	2×10^6	4×10^6	1×10^6	2.25×10^6	1.5×10^6	3×10^6
10°	℄	491.8 (−2.6)	492.0 (−2.4)	492.2 (−2.2)		491.8 (−2.9)		490.2 (−5.0)
13.5°	℄	495.0 (−1.1)	494.7 (−1.4)	494.5 (−1.6)		492.4 (−1.8)		490.2 (−4.3)
16°	℄	491.4 (−3.8)	493.2 (−2.0)	492.4 (−2.7)	476.2 (−3.1)	476.0 (−3.2)	476.7 (−1.4)	474.4 (−3.6)
	90°	498.8 (−1.0)	497.8 (−2.1)		482.9 (−1.6)	482.5 (−2.1)	482.4 (−1.5)	482.2 (−1.7)

Units are mm. Parenthetical is deviation from nominal location based on model geometry.

To make comparisons between the PIV and probe sampling test section configurations, data will be presented and compared in axial coordinates referenced to the inviscid impingement station determined for that particular configuration.

B. Wall Pressure Profiles

Figure 2 shows a comparison of the wall pressure data, corrected by the shock location derived from PIV, across several test campaigns at a common test condition of Mach 2.5 and $Re_D = 2 \times 10^6$. This is analogous to Figure 5 in Ref. 12. Clearly, the profiles are consistent between the three test entries which were carried out over several years. The typical features are an increase in the initial pressure jump at the reflected shock foot and overall pressure rise from the conical compression with increase shock generator angle. The axial separation of the incident shock and the expansion fan from the "shoulder" where the centerbody transitions from conical to cylindrical shape decreases with α thus decreasing the length of the linear ramp from the initial jump to the pressure peak.

Beyond the specific case compared in Fig. 2, an overall summary of wall pressure behavior corresponding to the current PIV dataset is presented in Fig. 3. For the higher-Mach conditions, comparisons with the previous HMVE entry at the common Reynolds number operating conditions are included to show repeatability. For Mach 2.5, the

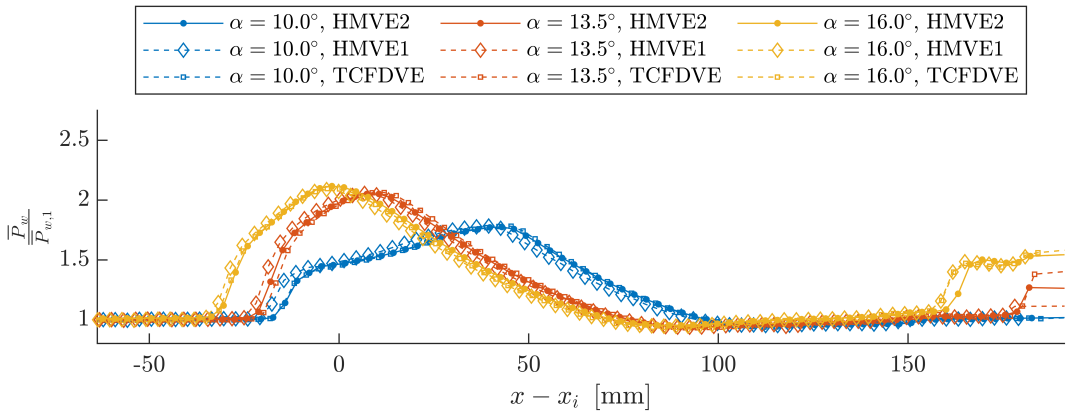

Fig. 2 Wall pressure profiles from instrumented window installed at $\theta = 0°$ in the axisymmetric configurations at Mach 2.5 and $Re_D = 2 \times 10^6$ from current and previous test campaigns.

abundance of test points precludes the inclusion of comparisons to previous test entries. As in Fig. 2, the profiles are quite repeatable between test entries for the higher Mach number nozzles. A key feature of Fig. 3a is the trend of increasing upstream influence of the interaction with decreases in core flow Reynolds number. This is in agreement with the previously observed increase in test section boundary layer scale as the Reynolds number is reduced [9]. At higher Reynolds number, the peak pressure achieved in the interaction is also enhanced across all shock generator angles at Mach 2.5. Conversely, the interactions appear quite insensitive to Reynolds number changes for the limited data available for the higher Mach number nozzles (Reynolds number reduction explored at $\alpha = 16°$ only). This is indicative of a relatively unchanged incoming boundary layer profile, which agrees with the nozzle exit Mach number values in Table 1 and observations from the PIV data, as will be discussed in subsequent sections. When looking across the Mach numbers, the reduction in compression length from the impingement of initial shock to the expansion from the conical shoulder of the centerbody with increasing freestream Mach number becomes apparent, especially in the $\alpha = 10°$ cases. The convergence of the compression and expansion features was the primary motivation for the creation of the larger $\alpha = 16°$ cone used in both HMVE entries, as mentioned in Section II.A.

Wall pressure profiles for the swept interactions studied in this entry are shown in Fig. 4 in comparison with common test points from the previous entry and also their axisymmetric counterparts. As with the axisymmetric cases, the behavior is quite repeatable after removal and re-installation of the test hardware. Similarly, the Reynolds number sensitivity of the interactions trends the same as in Fig. 3, being much more pronounced at Mach 2.5 than with the other two nozzles. For all the swept interactions, the peak compression is reduced relative to the axisymmetric case due to the out-of-plane pressure relief permitted in the azimuthal direction. Another universal feature is the increase in upstream influence from the inviscid impingement point which will be studied in the flowfield data from PIV in subsequent sections.

An interesting feature of both Figs. 3 and 4 is that the interaction at Mach 3.0 and $\alpha = 16°$ seems to have a larger upstream influence than the case with a higher pressure rise across the incident shock for $M_{0,\infty} = 3.5$. To investigate the dependence of these profiles on Mach number, Fig. 5 re-plots the profiles collected during the most recent test entry from Fig. 3 onto common axes for each shock generator angle. For all cases except the aforementioned outlier, a clear trend appears of upstream movement of the mean reflected shock foot location as the incident shock strength rises. This effect may also have a co-mingled Reynolds number effect, as that quantity is also increasing along with Mach number across the case since the $Re_D = 2 \times 10^6$ case was selected for display at Mach 2.5 so that the Reynolds number is monotonically decreasing with Mach number, as in Ref. 12. This trend will be investigated further through normalization by the incoming boundary layer scale in subsequent sections. Returning to the anomolous behavior in Fig. 5c, wall pressure profiles from probe testing are included to isolate whether the effect is repeatable across configurations (or perhaps an artifact of the x_i determination method from PIV). The selected profiles were obtained while the probe is located well outside the boundary layer and aft of the current region of interest so there is minimal influence at the wall. These profiles show a much greater deviation from the PIV configuration at Mach 3.0 than at Mach 3.5. While the Mach 3.0 profiles agree quite well in peak pressure and align in the expansion region, there is a clear stretching of the forward portion of the PIV configuration profile out to a further upstream extent. As shown in

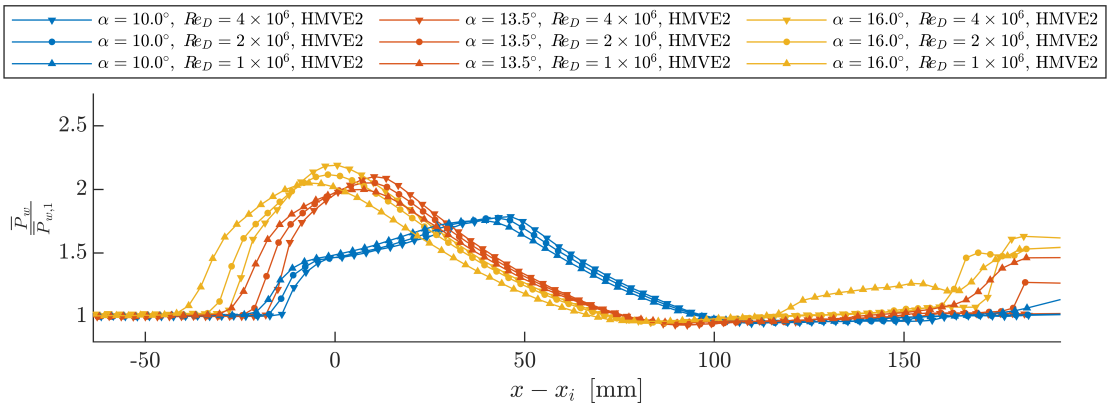

(a) $M_{0,\infty}$ = 2.5

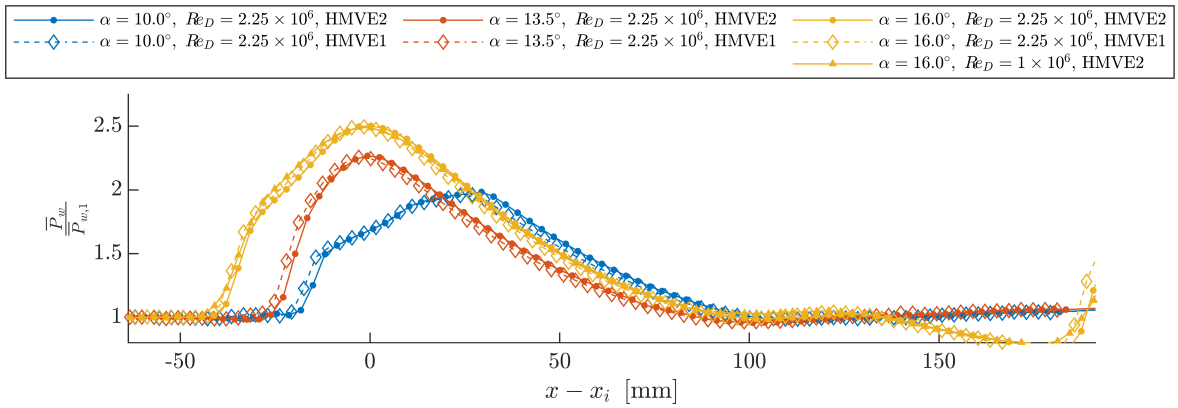

(b) $M_{0,\infty}$ = 3.0

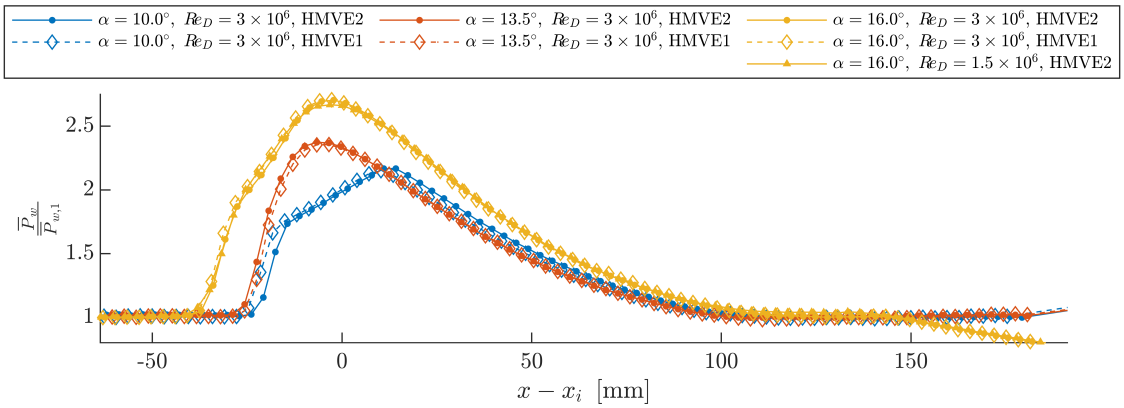

(c) $M_{0,\infty}$ = 3.5

Fig. 3 Wall pressure profiles from instrumented window installed at θ = 0° in axisymmetric interactions compared across the α range at all three freestream Mach number values.

Fig. 3, the profile is quite consistent in the PIV configuration across both HMVE entries, further indicating that the x_i value is not to blame. Further investigation utilizing the flowfield surveys through probe measurements will provide key insight into whether the origin of this behavior is due to some difference in the incoming boundary layer behavior between configurations.

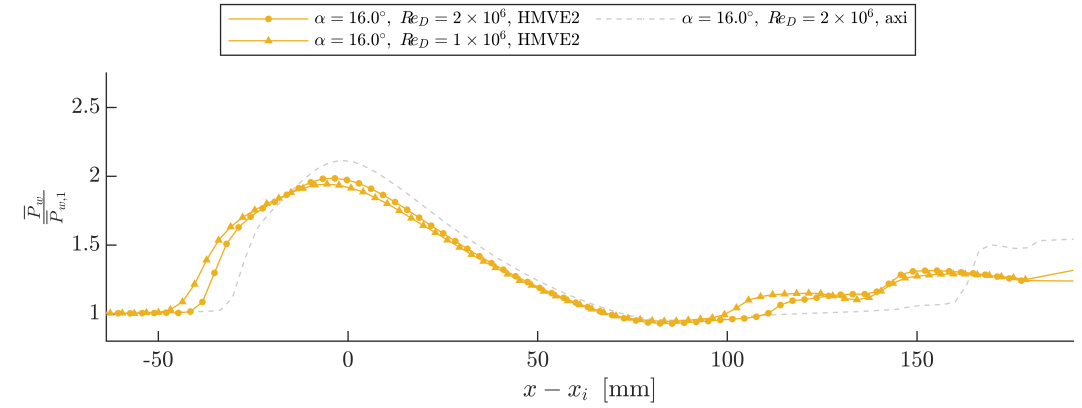

(a) $M_{0,\infty}$ = 2.5

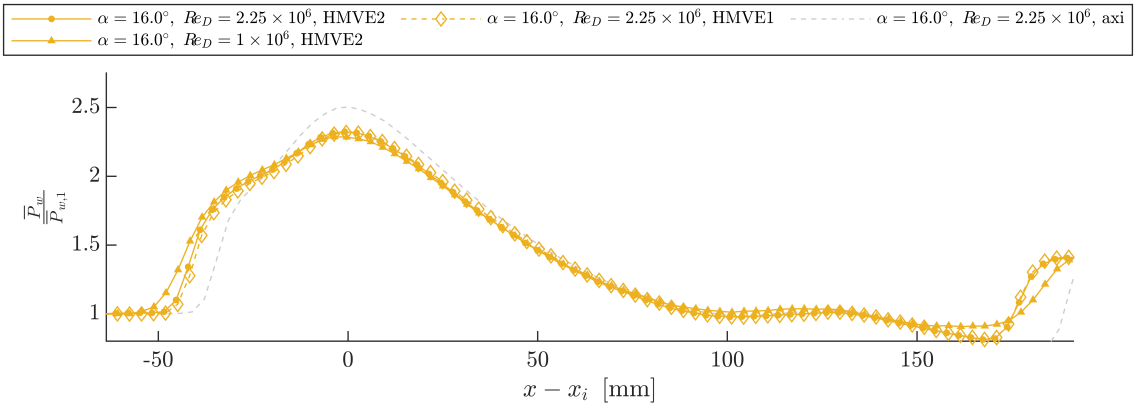

(b) $M_{0,\infty}$ = 3.0

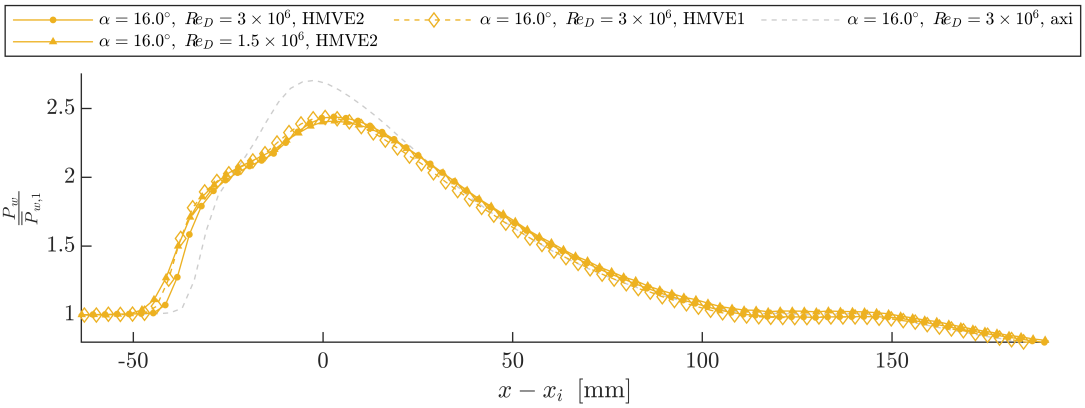

(c) $M_{0,\infty}$ = 3.5

Fig. 4 Wall pressure profiles from instrumented window installed at $\theta = 0°$ in swept ($\ell = R_{TS}/4, \theta = 90°$) interactions all three freestream Mach number values relative to axisymmetric behavior.

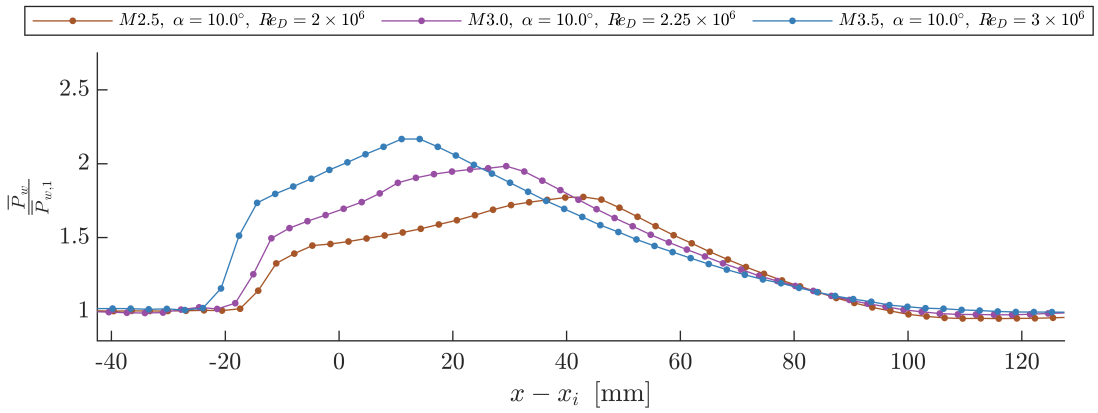

(a) α = 10°

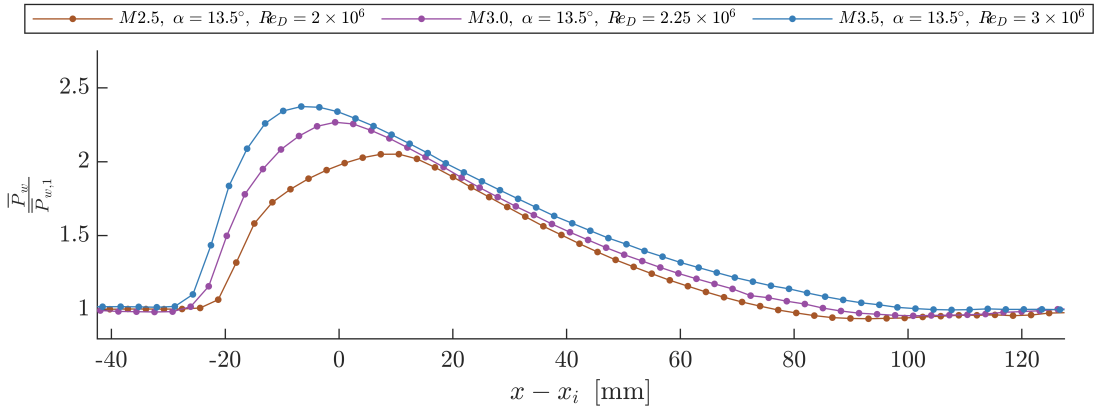

(b) α = 13.5°

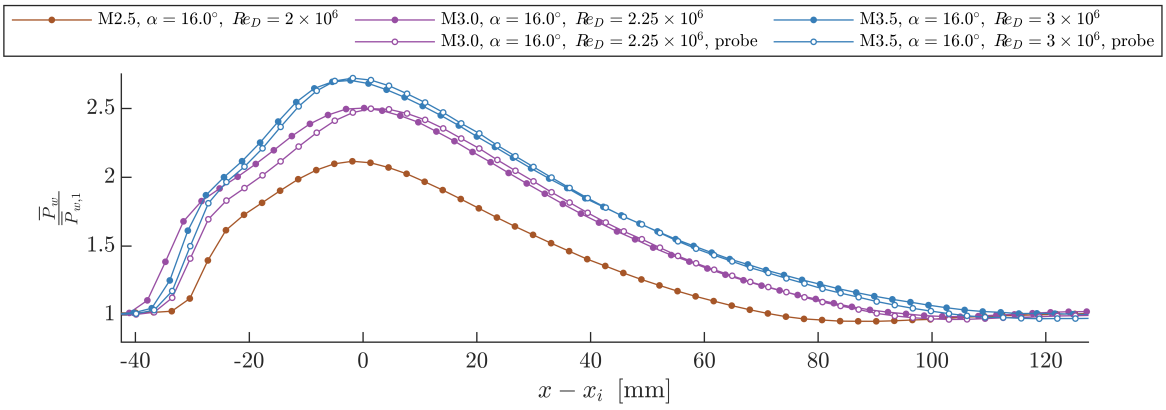

(c) α = 16°

Fig. 5 Wall pressure profiles from instrumented window installed at θ = 0° in axisymmetric interactions compared across the freestream Mach number range at all three shock generator angles.

C. General Flowfield Topology

In the appendix, stitched PIV fields from all camera views are presented for all three values of freestream Mach number across the various shock generator configurations to provide relative comparisons. For each, mean flow streamlines are overlaid to illustrate the overall flow behavior underlying the individual velocity components. These figures follow the format presented in Ref. 12 so that direct comparisons can be made. However, the addition of new cases at reduced Reynolds number has expanded the scope and, thus, the subsections are reorganized to include the additional test points. Instead of grouping the figures by shock generator angle and comparing across freestream Mach number values, the data herein is grouped by freestream Mach number to include the additional variable of Reynolds number and illustrate the variations in flowfield behavior produced thereof. Broad observations on the flowfield topology are discussed in this section while detailed quantitative comparisons are deferred to subsequent sections.

It is important to note that the limits of the color scales for turbulence quantities change with shock generator angle due to the drastic difference in peak normalized turbulence levels. The color maps are consistent with Ref. 12 for direct comparison with results from the previous entry, where applicable. Thus, if turbulence levels are elevated from what was previously observed, the color scale may become saturated in some regions. The true peak values will be better resolved in the following sections which plots detailed profiles of the data extracted at select axial stations.

In corroboration of the wall pressure profiles presented in Figs. 3a and 4a, the upstream influence observed in the Mach 2.5 interactions is increased at lower Reynolds number conditions. Looking closely at the upstream region in Figs. A1, A4 and A7, the change in boundary layer height becomes clear. This will be studied more quantitatively in subsequent sections of this report. Similarly, the trends observed in Figs. 3b, 3c, 4b and 4c are confirmed in the PIV results, where the comparisons across Reynolds number in Figs. A19 to A24 and Figs. A31 to A36 show very little change in the length of upstream influence forward of the inviscid impingement location. Figures A11, A12, A23, A24, A35 and A36 also illustrate the further upstream influence and overall weakening of the interaction (reduced mean velocity deficit and turbulence intensity) in the swept configurations.

Inspection of these contour plots does not provide confirmation of the unexpectedly large upstream influence observed in the wall pressure profiles at Mach 3.0 in Fig. 5c. In fact, close comparison of Figs. A19b to A21b and Figs. A31b to A33b reveals that the forward-most influence of the shock occurs at a very similar location between the Mach 3 and 3.5 cases at $\alpha = 16°$. Corroboration for the wall pressure rise occurring ≈ 1 mm forward in the Mach 3.0 case is only provided by the $\overline{u'v'}$ field, which does show a forward shift in the high shear region at the reflected shock foot. This suggests that the effect seen in the wall pressure could be driven by transient motion of the reflected shock foot combined with a low-pass filtering effect from pneumatic lag or seed oil infiltration in the capillary tubing. Proof of such would require a statistical analysis of the flowfield data, which is beyond the scope of this report. Additionally, the 15 Hz data acquisition rate of the PIV system will only provide a partial view of the shock foot transient behavior. Thus, further analysis of this behavior is deferred to future reports which include the high-bandwidth turbulence measurements facilitated by the hot-wire probes.

As for general trends across the Mach and Reynolds number range tested, the effect of increased boundary layer thickness at reduced Reynolds number for the Mach 2.5 cases provides better resolution of the interaction behavior for a fixed camera sensor scale and magnification. At other freestream Mach number values, with the boundary layer changing very little, the interaction scale is relatively unchanged. The primary difference observed with varying Reynolds number in these interactions is an increase in peak turbulence levels, which is likely an artifact of seed droplet differences induced by operating the particle generator at different pressures. At all freestream Mach number conditions tested, the streamwise normal turbulence stress is increased by approximately 50% and the turbulent shear stress approximately doubles from the levels measured in the incoming boundary layer for the 10° case. For the interactions containing some degree of separation, the magnitude of turbulence enhancement becomes stronger with increasing freestream Mach number while the general shape and scale of the regions of high turbulence look quite similar. This will be analyzed in subsequent sections in further detail.

In interactions where separation occurs ($\alpha = 13.5°$ and 16°), the PIV measurements are sometimes polluted by an imaging artifact which arises from pooled seed material at the separation line. This is inevitable with the downward viewing angle of the cameras and the axisymmetric shape of the test section. The oil droplets, acting as faithful tracers of the flowfield, are entrained into the separated region and begin to collect at the $\theta = 180°$ location due to gravity. This results in a region of bright scattering in the PIV images not just in the separation bubble itself (as they would in even a 2D near-wall PIV measurement with appreciable pooling) but also along a line in the background which approximately traces the separation line through some extent around the test section azimuth. In the mean velocity fields, this manifests as a region of low streamwise velocity which is delineated by sharp gradients which stand out from the smoothly-varying velocity field. Similarly, a region of strong streamwise turbulence intensity is also manifested near

the reflected shock foot location. A typical example of this behavior is highlighted in Figs. A19a, A20a and A21a where the artifacts are circled. This portion of the data was not masked out in this section to avoid biasing the results with the selection of an arbitrary metric for rejecting non-physical data. Thus, the reader is cautioned to consider this aspect of the data when making comparisons with other test or simulation data.

D. Detailed Flowfield Profiles

In order to perform detailed comparisons between flowfield realizations, PIV results are extracted at select stations which align with the discrete sampling stations used in the companion probe measurements (as in Ref. 10). In an effort to distribute the data in a format with a manageable file size, this is also how the data is structured in the files accompanying this report.

1. Incoming Boundary Layer

One of the primary requirements for this dataset was to ensure that the state of the undisturbed boundary layer entering the interactions was well-characterized. Any quantitative comparison between CFD solutions of the SWBLI and the experimental data will require matching of at least the mean streamwise velocity profile. Because the precise location of the transition point within the facility nozzle is difficult to ascertain experimentally, a simple solution to match the experimental boundary layer in a CFD solution is to add a length of cylindrical pipe upstream of the converging-nozzle whose length is tuned to match the experimental state just upstream of the interactions, as in Ref. 13. Figure 6 shows representative streamwise velocity profiles at $x = 419.1$ mm (16.5"). These profiles are provided in dimensional units to illustrate the small range of scatter in freestream velocity across the Reynolds number range for each nozzle. As noted from the wall pressure profiles, the boundary layer is much more sensitive to the Reynolds number condition when using the Mach 2.5 nozzle than the other two. The Mach 2.5 behavior follows the expected trend and the boundary layer thickening is corroborated by both $M_{0,\infty}$ calculations from the nozzle exit static pressure (Table 1) and $M_{1,\infty}$ trends observed with Pitot probe measurements. For the other two nozzles, the relatively unchanged displacement thickness is also in line with the sensitivity of nozzle exit Mach number to Reynolds number condition. The integral parameters in the undisturbed boundary layer profiles are quantified in Table 3. There, a summary of typical turbulent boundary layer parameters derived from the PIV measurements is provided. Due to the lack of near-wall data, the profiles are not directly integrated, but instead a log-law profile is fit to the measurements as in Ref. 9 and integral parameters are derived thereof with the additional near-wall data provided by the canonical profile. While this adds fidelity to the derived integral parameters, the friction coefficient values have the noted caveat of being based on only a few points within the logarithmic region of the boundary layer. Probe-based measurements are much better-suited to accurately obtaining this quantity. Similarly, the near-wall viscous scale is estimated from using the derived friction velocity values to illustrate the scales required to resolve the boundary layer across the cases.

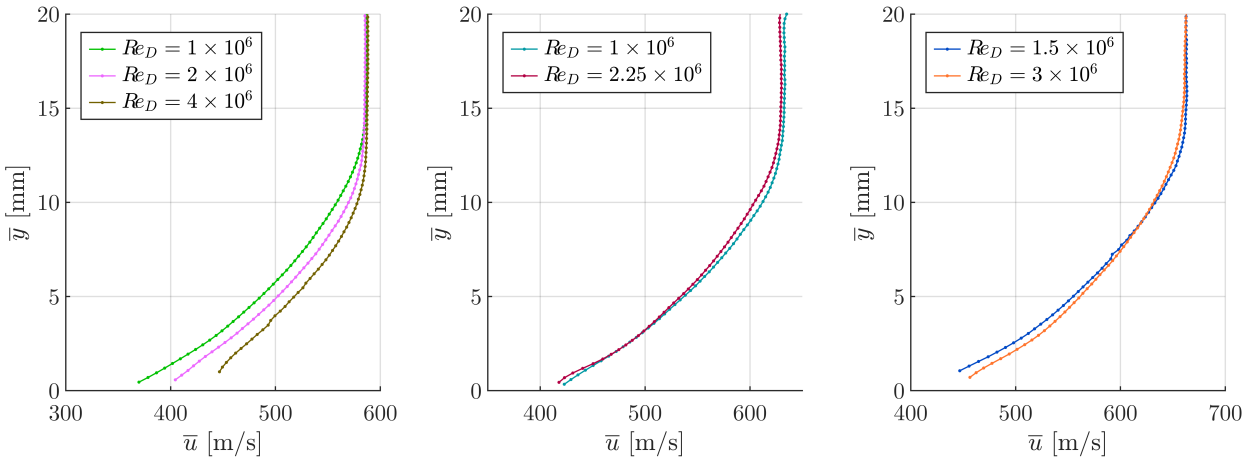

(a) $M_{0,\infty}$ = 2.5. **(b) $M_{0,\infty}$ = 3.0.** **(c) $M_{0,\infty}$ = 3.5.**

Fig. 6 Upstream boundary layer mean velocity profiles for the various facility nozzles tested.

Table 3 Incoming boundary layer velocity profile parameters.

Nominal		Measurements					
$M_{0,\infty}$	$Re_D \times 10^{-6}$	$\delta_{99.5}$ [mm]	δ^* [mm]	θ [mm]	Re_{δ_2}	$c_f \times 10^3$	δ_ν [µm]
2.5	1	13.7	3.90	1.01	3,160	1.68	15.9
2.5	2	12.1	3.33	0.88	5,550	1.53	8.29
2.5	4	11.4	2.94	0.79	9,770	1.42	4.37
3	1	12.7	4.13	0.82	2,080	1.56	22.6
3	2.25	13.4	4.17	0.85	4,850	1.34	10.6
3.5	1.5	13.9	4.94	0.80	2,500	1.31	21.9
3.5	3	13.9	4.83	0.78	4,750	1.12	12.2

These PIV results will be supplemented by probe measurements which have better near-wall capability in a future all-encompassing report. Preliminary analysis of Pitot probe data shows similar overall trends boundary layer height across the facility Reynolds number range at Mach 3.5 with a slightly increased displacement thickness at lower values and a relatively unchanged overall boundary layer height ($\delta_{99.5}$). The overall boundary layer height values from the probe measurements agree with the PIV to within 0.1% and the integral parameters within 2.5%. For the Mach 3.0 nozzle, the boundary layer is a bit more sensitive to Reynolds number with a slight decrease in $\delta_{99.5}$ and integral parameters at lower pressure. This is opposite to the expected trend which has been repeatedly observed for the Mach 2.5 nozzle in both probe and PIV measurements, as has been discussed. However, these results are also backed up by the probe measurements, which show the same trends and agree with the PIV to within 4%.

Similarity of the profiles in Fig. 6 is evaluated in Fig. 7 where the dimensionless equivalent incompressible velocity defect, $\left(\overline{u}^*_\infty - \overline{u}^*\right)/u_\tau$, given by the van Driest transform of the data is plotted against a non-dimensional wall-normal distance. The selection of ideal parameters by which to normalize the data is still a subject of active research, especially when working with compressible boundary layers [14]. The most obvious outer scale for the boundary layer is $\delta_{99.5}$, which is used in Fig. 7a. The collapse for $y/\delta > 0.3$ appears quite good across the Mach and Reynolds number range. Closer to the wall, the data becomes a bit more scattered with no clear dependence on tunnel operating condition. In comparison with the universal behavior suggested by Pirozzoli & Smits [14], a general trend is observable that the velocity defect is a bit higher in the quadratic portion of the profile and falls below the expected logarithmic behavior at the points nearest the wall. As suggested by Fernholz & Finley [15], the Rotta-Clauser [16, 17] integral length scale, Δ, is used in Fig. 7b to scale the wall-normal height. This scale is sometimes preferred over $\delta_{99.5}$ since that parameter is highly sensitive to the accuracy of the measurement. To match the magnitude used for the x-axis of the plots, the scale in Fig. 7b is multiplied by 3.6, the value of $\Delta/\delta_{99.5}$ for a zero pressure gradient boundary layer [17]. In this normalization, the profiles are more tightly grouped throughout the quadratic region. Also, the mismatch from the (incompressible) empirical profile is greatly reduced with the data only diverging from the correlation for $(3.6y/\Delta) < 0.1$. This behavior is common among compressible boundary layer experiments, as surveyed in Ref. 18.

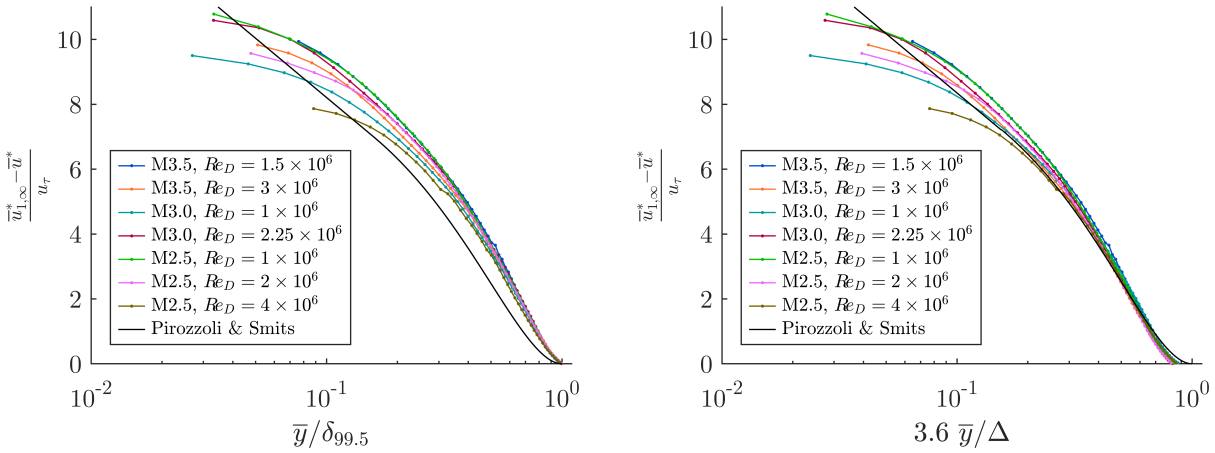

(a) Classical wall-normal scaling. **(b) Rotta-Clauser scaling.**

Fig. 7 Boundary layer defect profiles using various scaling methods.

2. Interaction Region - Comparison Across Freestream Conditions

For direct visualization of the flowfields' sensitivity to the incident shock strength, Figs. 8 to 10 gather profiles across the Mach number range. These figures present the higher Reynolds number case for the high Mach number conditions since that is where data was collected at all three shock generator angles. As in Fig. 5, the intermediate Reynolds number case is displayed for Mach 2.5 so that the Reynolds number is monotonically decreasing with Mach number. Also following previous publications from this test campaign, the spatial coordinates are non-dimensionalized by the incoming boundary layer displacement thickness, δ_1^*, to eliminate overall scale of the experiment from the results.

Figure 8 shows the relative change in the streamwise mean velocity through the interactions at the various shock generator angles. As expected, the maximum deficit in the mean streamwise velocity induced near the wall becomes deeper not only with α but also with increasing freestream Mach number for 10° and 13.5° as the incident shock wave is strengthened. For example, shock pressure ratio increases from 1.38 at Mach 2.5 to 1.84 at Mach 3.5 in the case of the α = 13.5° cone. For the α = 16° case, the boundary layer becomes fully separated at all freestream Mach numbers and mean velocities near zero are attained. Across the plots, there is a clear trend for the velocity-deficient region to spread further from the wall at lower Mach number. This is likely a Reynolds number effect and will be discussed further subsequently.

At each freestream Mach number setting, the expected trend is observed with the velocity deficit initiating further upstream and reaching deeper levels with increasing α. Comparing across the plots, it becomes clear that the pressure rise across the incident shock and its reflection are not the only influence upon the upstream extent of the interaction. Rather, the case which contains the weakest incident shock (Mach 2.5) exhibits the greatest upstream influence when normalized by the incoming boundary layer scale. Figure 11 shows that the mean wall pressure profiles show a similar behavior with a subtle forward movement of the initial pressure rise at lower freestream Mach number except for the outlier at Mach 3.0 and α = 16° previously noted in Fig. 5c. The flowfield data is better suited to determine the most upstream location of the reflected shock foot, as it is an ensemble average of individual snapshots rather than a pneumatically-averaged measurement, and thus displays this effect with more contrast. In the end, this trend is attributed to a Reynolds number (which trends with freestream Mach number here) effect and could be further analyzed with application of the pressure from PIV technique used in Ref. 10.

At the furthest downstream station shown, the profiles have not recovered to a universal behavior, with the lower Mach number cases scattered further. The downstream boundary layer edge velocity also remains further suppressed from the incoming value at lower Mach number. Both of these effects are due to the larger spatial separation between the incident shock and the expansion fan which emanates from the cone-cylinder shoulder.

Figures 9 and 10 illustrate the behavior of the turbulent stresses of primary importance in these interactions at sampling stations identical to that of Fig. 8. While the relatively sparse spacing of the profiles herein limits the ability to compare the true peak turbulence levels across the cases, the expected trend is still clearly visible: stronger turbulence persisting over a larger streamwise extent for increasing α. The streamwise turbulence intensity tends to appear like

boundary layer turbulence with a monotonic increase toward the wall in unseparated interactions. For interactions where the boundary layer separates, the intensity peaks further from the wall and decays into the separation zone. In-plane shear behaves similarly, resembling boundary layer behavior up to the location of the reflected shock foot. The $\alpha = 10°$ results show only a mild enhancement of the turbulence (Figs. A3, A6 and A9 show that further enhancement occurs downstream of the stations selected here) while $\alpha = 13.5°$ and 16° exhibit a common behavior — a strong negative stress (same sign as incoming boundary layer shear) which traces the reflected shock foot mean position with a small underlying region of positive shear which becomes most pronounced in the strongest interaction ($M_{0,\infty} = 3.5,\ \alpha = 16°$, see Fig. A33b). The existence of a positive shear region is in congruence with other impinging SWBLI results in experiments [19, 20] and simulations [21].

The larger separation induced at higher angles tends to shift the location of maximum $\overline{u'u'}$ and $\overline{u'v'}$ away from the wall at a given station as the peaks track the shear layer above the forward side of the separation bubble. As shown in the contour plots of Section III.C, the streamwise turbulence intensity peak tends to wrap around the bubble and move back toward the wall near the inviscid impingement point while the region of high *positive* shear stress abruptly ends at the apex of the low-velocity region. A secondary negative shear region is established in the recovering layer beyond reattachment. This is most obvious at $\alpha = 16°$ (cf. Figs. A8, A20 and A32 against Figs. A9, A21 and A33).

As with the mean velocity, at lower Mach numbers the turbulent region is spread over a larger wall-normal extent with increasing peak intensity and sharper gradients as Mach number increases. In both turbulence quantities shown, the profiles at the final station ($x - x_i = 0.5\delta_1^*$) return to a similar form across α and $M_{0,\infty}$ conditions. The peak streamwise normal stress appears further from the wall for increasing α and appears to attain a similar maximum value for the $\alpha = 13.5°$ and 16° cases. The final ($\overline{u'v'}$) profiles match this trend with the peak also moving further from the wall for increasing shock generator angle. In this quantity, however, there is a clear trend of higher maximum stress as well. This is confirmed when looking at the overall field in Section III.C where the turbulent shear stress appears to be the quantity for which the departure from the upstream state persists most.

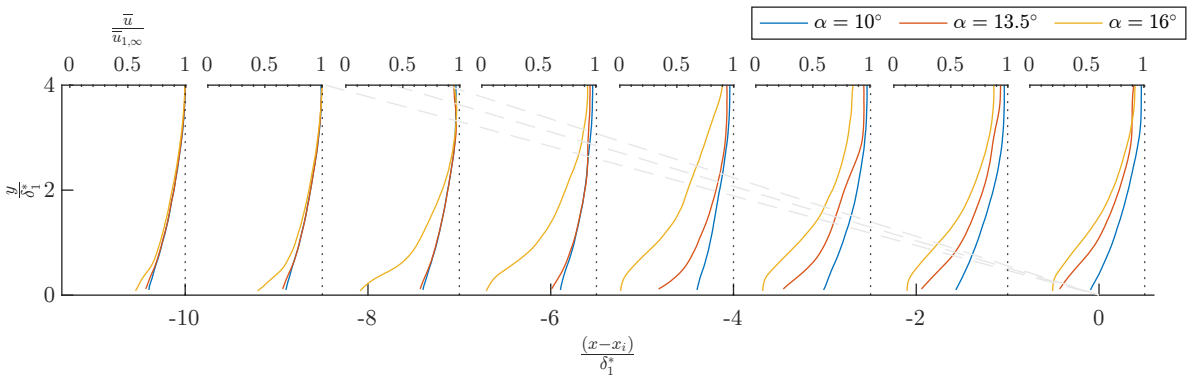

(a) $M_{0,\infty} = 2.5$, $Re_D = 2 \times 10^6$

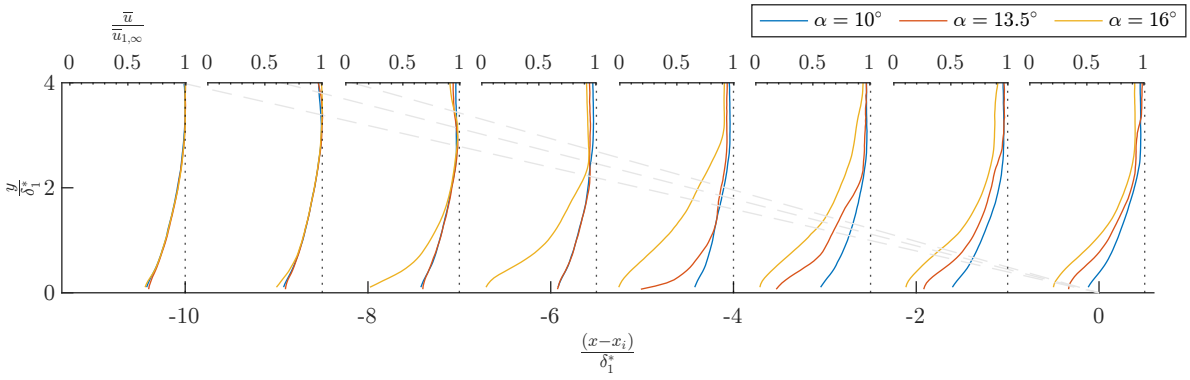

(b) $M_{0,\infty} = 3.0$, $Re_D = 2.25 \times 10^6$

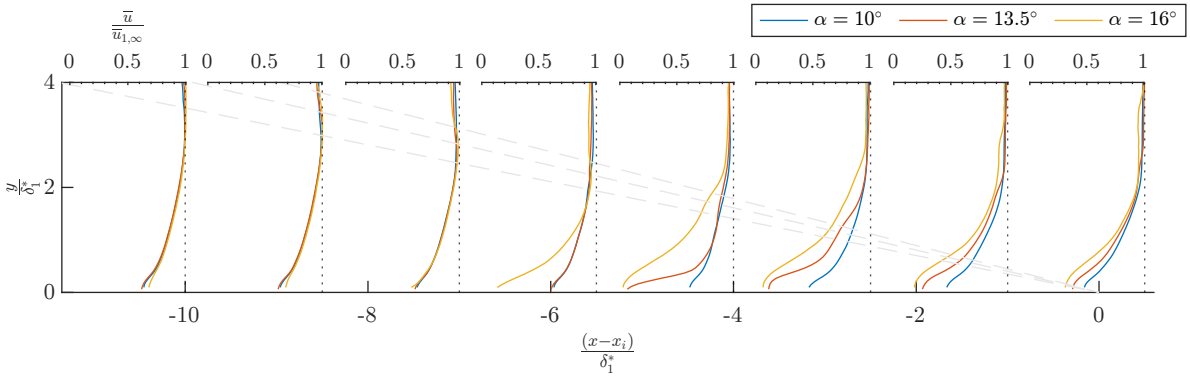

(c) $M_{0,\infty} = 3.5$, $Re_D = 3 \times 10^6$

Fig. 8 Mean streamwise velocity profiles for axisymmetric interactions across the Mach number range.

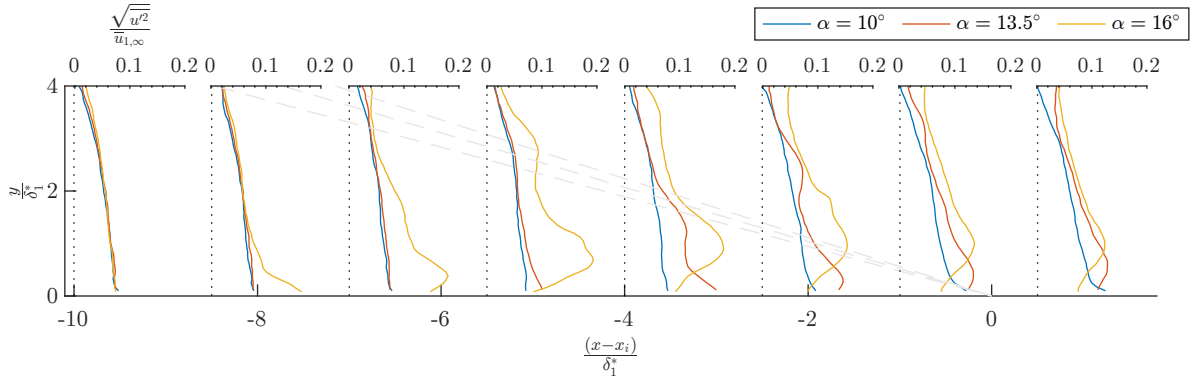

(a) $M_{0,\infty} = 2.5$, $Re_D = 2 \times 10^6$

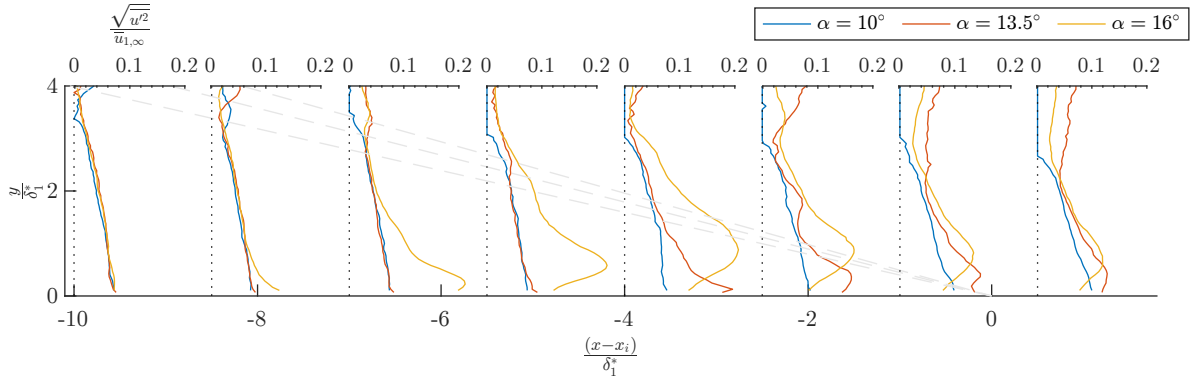

(b) $M_{0,\infty} = 3.0$, $Re_D = 2.25 \times 10^6$

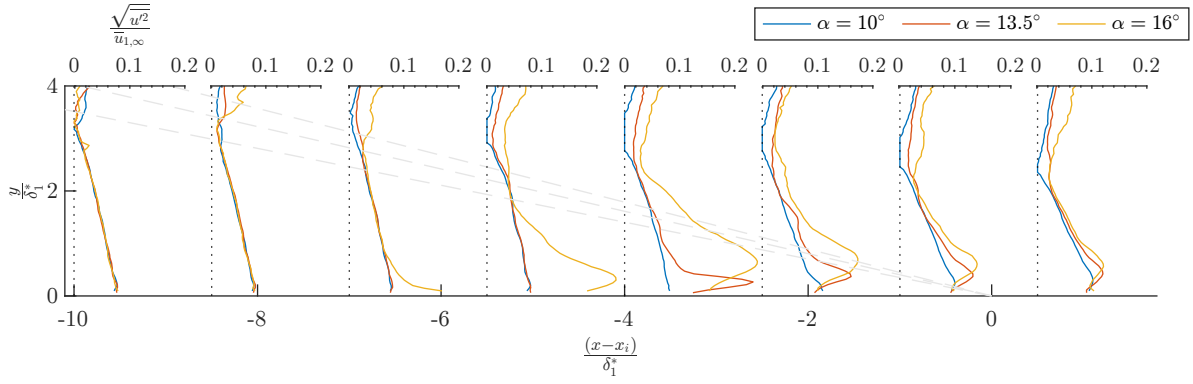

(c) $M_{0,\infty} = 3.5$, $Re_D = 3 \times 10^6$

Fig. 9 Streamwise turbulence intensity profiles for axisymmetric interactions across the Mach number range.

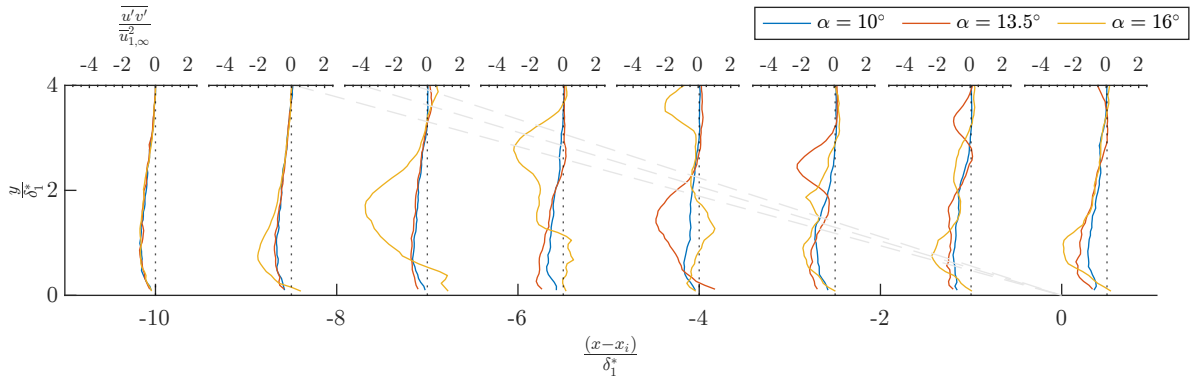

(a) $M_{0,\infty} = 2.5$, $Re_D = 2 \times 10^6$

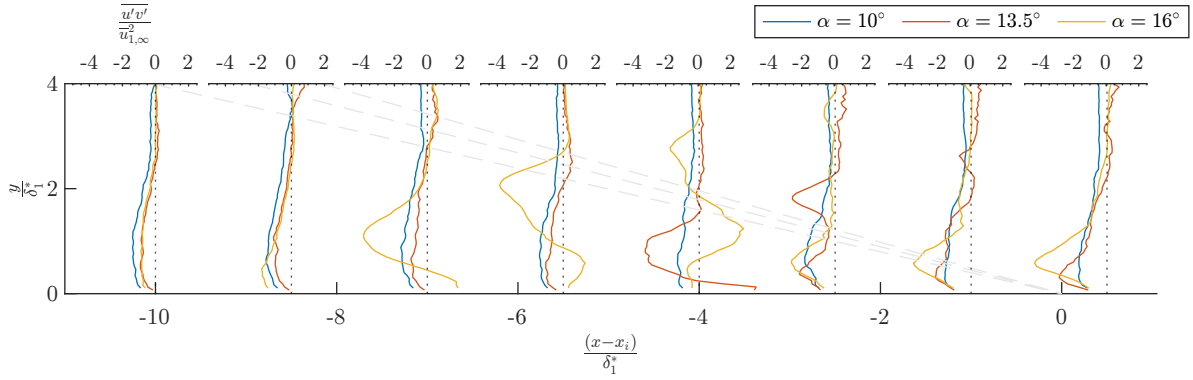

(b) $M_{0,\infty} = 3.0$, $Re_D = 2.25 \times 10^6$

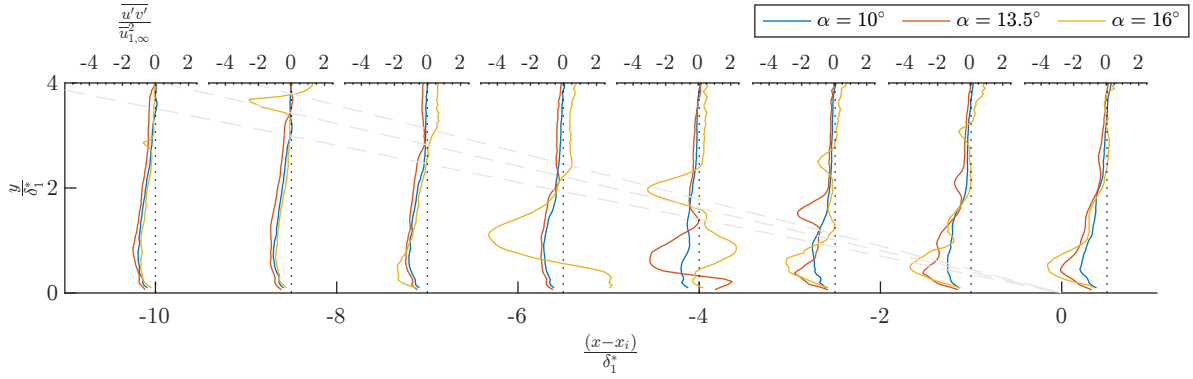

(c) $M_{0,\infty} = 3.5$, $Re_D = 3 \times 10^6$

Fig. 10 In-plane turbulent shear stress profiles for axisymmetric interactions across the Mach number range.

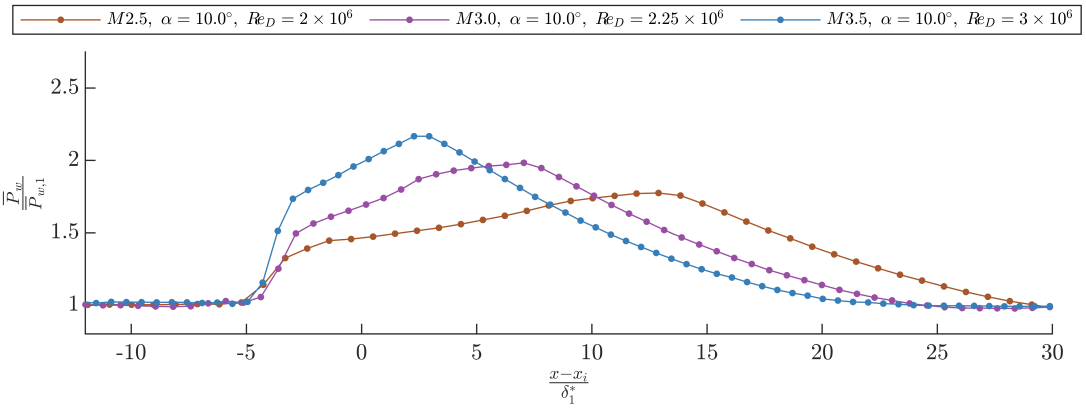

(a) α = 10°

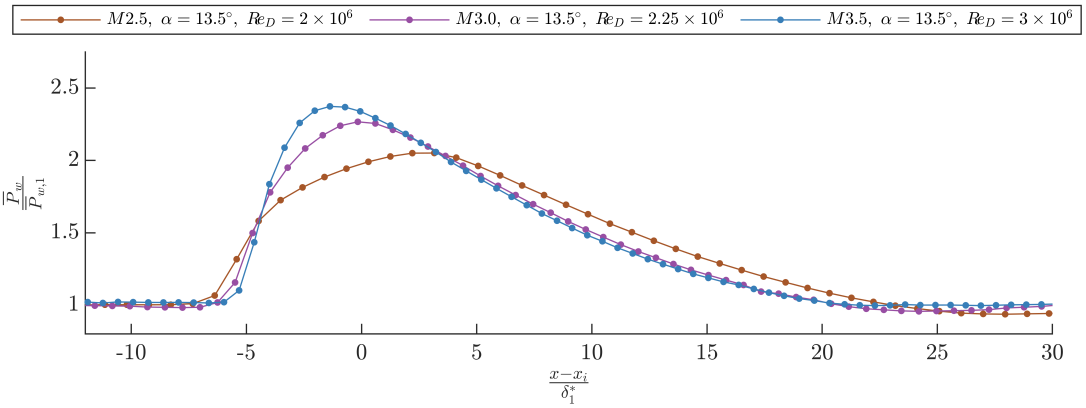

(b) α = 13.5°

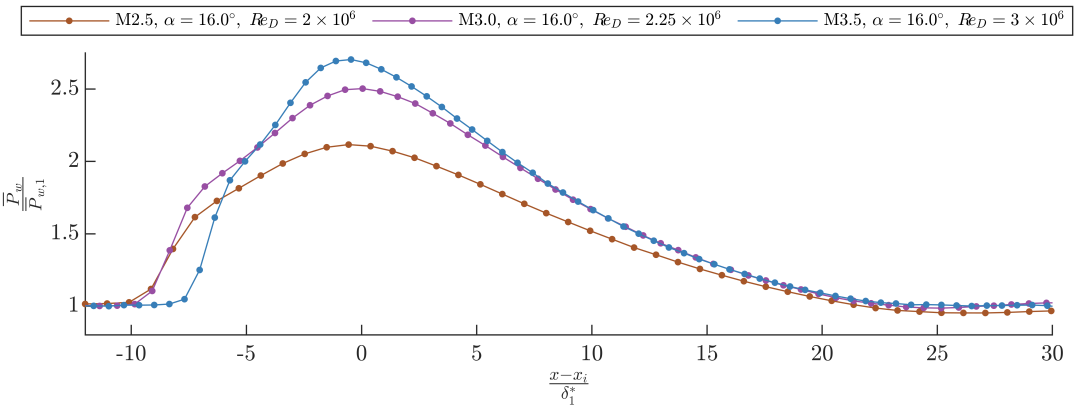

(c) α = 16°

Fig. 11 Wall pressure profiles from instrumented window installed at θ = 0° in axisymmetric interactions compared across the freestream Mach number range with axial coordinate normalized by incoming boundary layer scale.

As discussed in Section III.C, the scale of the upstream influence of the interaction is highly coupled with the scale of the incoming boundary layer. If a spatial or velocity normalization can eliminate these effects, comparisons can be made across cases operated at different Reynolds number, which is especially advantageous for generating scale-resolving CFD simulations of this flow with tractable grid size. Figures 12 to 20 show how well scaling by the incoming boundary layer displacement thickness, δ_1^*, collapses the mean and turbulent velocity profiles at each freestream Mach number condition. This is the normalization method used previously for small boundary layer differences between experiments and computations [13]. For the Mach 2.5 case, data was collected at multiple Reynolds numbers for each shock generator cone angle. This data is grouped by velocity component into Figs. 12 to 14. For the higher Mach numbers, Reynolds number was only varied for the strongest shock wave case ($\alpha = 16°$).

Looking broadly across the set of figures it is clear that spatial scaling alone cannot collapse the data completely. At Mach 2.5 (Figures 12 to 14), while the incoming profiles and aft-most profiles collapse to a common behavior, the agreement is not good within the primary interaction region. This is not unexpected, as the interaction will not only scale with the overall boundary layer scale, but also the ratio of outer to inner scale which is a strong function of Reynolds number (itself commonly termed the "friction Reynolds number"). Thus, while some outer effects may be collapsed by the current non-dimensionalization, the increasingly disparate outer and inner length scales will drive additional effects which cannot be simultaneously accounted for with normalization by a single scalar factor. Here, it would appear that these effects manifest most in a greater upstream influence at lower Reynolds number which drives a corresponding shift of the shear layer away from the wall for a fixed sampling station. The Reynolds number sensitivity of SWBLI upstream influence has been previously noted in both compression corner experiments [22], impinging shock simulations [23], and universal analytical scaling arguments [24].

At the higher freestream Mach numbers, the mean velocity profiles in Fig. 15 and Fig. 18 do not indicate nearly the same Reynolds number dependence as that observed for Mach 2.5. In particular, the Mach 3.0 data shows very little change in the upstream influence of the interaction while Mach 3.5 shows a slight increase at lower Reynolds number. Additionally, the wall-normal coordinate of the peak streamwise normal turbulent stress and in-plane turbulent shear stress appear to match quite well across the Reynolds number range. Since the test section wall boundary layer scale was little affected by Reynolds number at these Mach numbers, the normalization by δ_1^* is making very small relative changes to the profiles. Thus, the result here can be summarized as both the incoming boundary layer and SWBLI being unaffected by halving the Reynolds number. The SWBLI behavior is confounding in light of the trend observed at Mach 2.5 and results in the literature, suggesting that these conditions are beyond some asymptotic state where Reynolds number no longer affects the scaling of the upstream influence, or possibly, the same phenomenon causing the insensitivity of the boundary layer to pressure changes is also manifesting in the SWBLI behavior. Hopefully further study including the probe measurements or detailed simulations may help elucidate the cause of this behavior.

As for the turbulence quantities, the peak streamwise normal stress which appears in the shear layer above the separated region in the $\alpha = 13.5°$ and $16°$ cases is attenuated as Reynolds number is reduced (see Figs. 13c, 14c, 16, 17, 19 and 20). This is in agreement with the recent LES simulations of Laguarda et al. [23] which showed a the location of peak streamwise stress to move very near to the reflected shock foot mean position for a Reynolds number reduction similar to the largest range explored here (Mach 2.5). Figures 16 and 19 illustrate a key artifact of pushing the limits of low Reynolds number operation — the difficulty in delivering sufficient particles into the core flow to properly seed the upper regions of the field of view behind the incident shock wave. For the strong turning at the shock in these cases, flow angles up to 9.5° are incurred, which brings flow far outside the original boundary layer into the measurement region. This is observable in Figs. A20a and A32a, where both the downward-running streamlines and enhanced turbulence are evident in the region of $\overline{y} > 12$ mm aft of the incident shock wave. Unseeded flow entering the field of view reduces the quality of correlation thus adding noise to the measurement. For mean flow quantities, this averages out over the large number of samples, but statistical measures, such as the turbulent normal stresses, are enhanced. Thus, the increase in $\overline{u'^2}$ observed in the outer part of the profiles is a Reynolds number effect only in the manner that the tunnel operating condition affects the seed dispersion. It is not a property of the flowfield. The shear stress plots are relatively unaffected since stochastic noise in the correlation should be uncorrelated between the two velocity components. Instead, the profiles generally agree across Reynolds number where the lack of smoothness in the profiles at low Reynolds number is attributed to a reduction in valid vectors. As the wall is approached, the profiles come into agreement for $\overline{y} \lessapprox 11$ mm. This effect is also mitigated further downstream as the reflected shock and expansion fan from the shoulder of the cone-cylinder centerbody counteract the initial negative $\overline{v}$ which brought unseeded freestream flow into the measurement region, as shown in the figures contained in the Appendix.

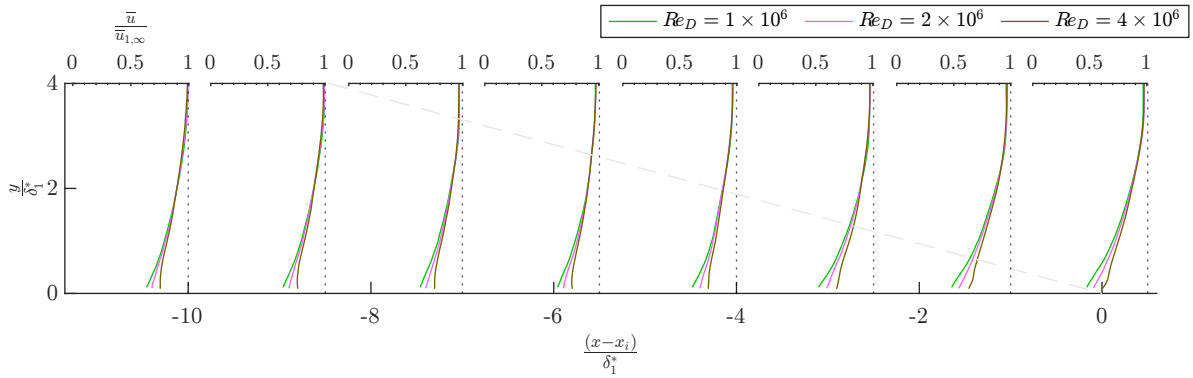

(a) α = 10°

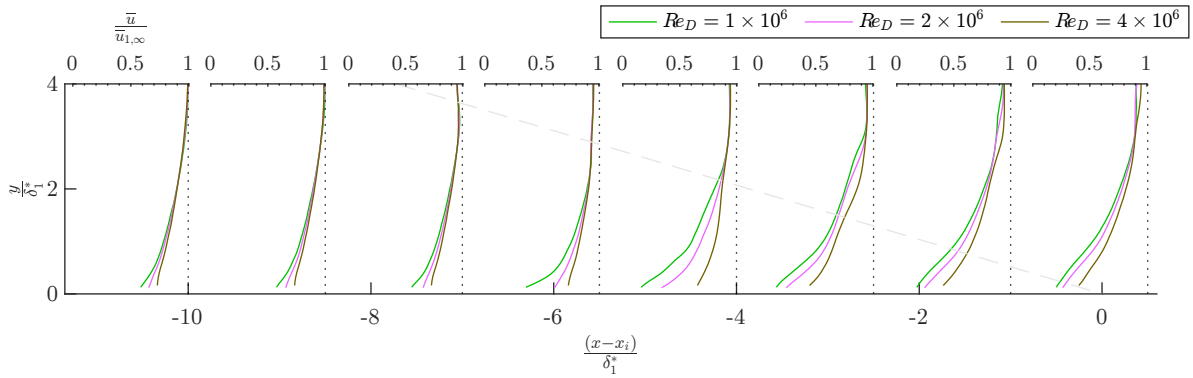

(b) α = 13.5°

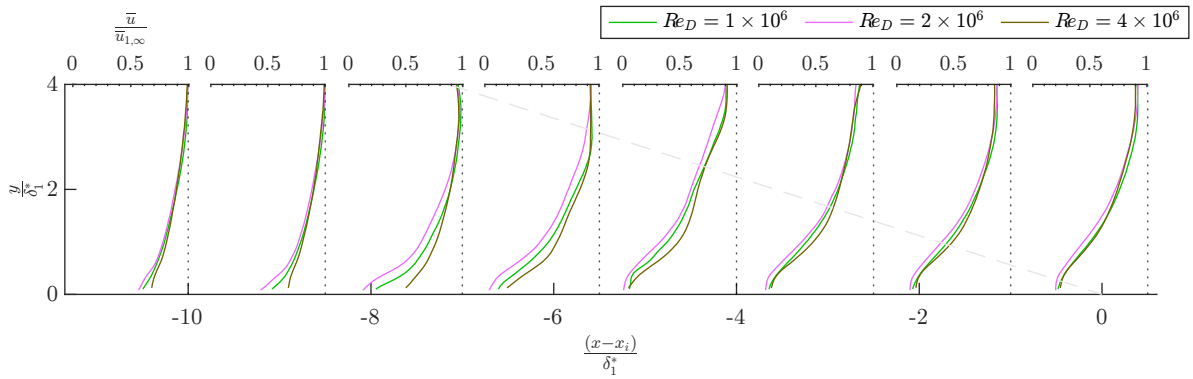

(c) α = 16°

Fig. 12 Mean streamwise velocity profiles for Mach 2.5 axisymmetric interactions across the Reynolds number range for all three shock generator angles.

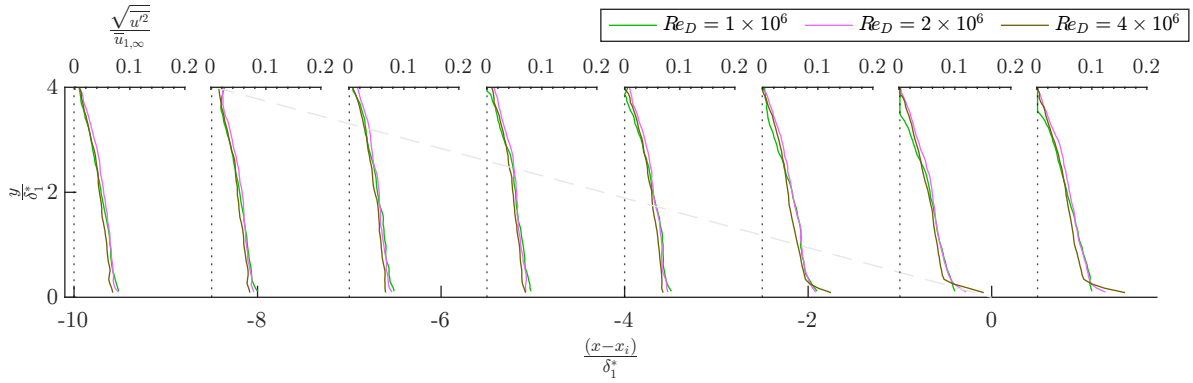

(a) α = 10°

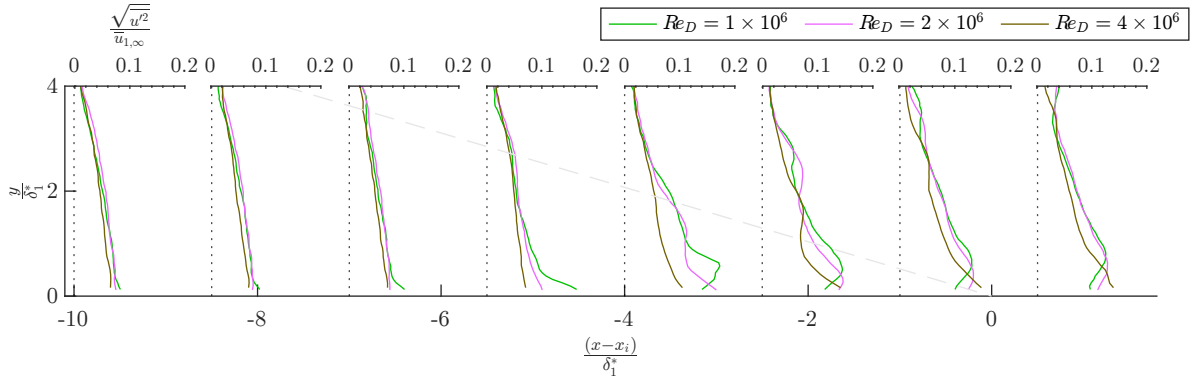

(b) α = 13.5°

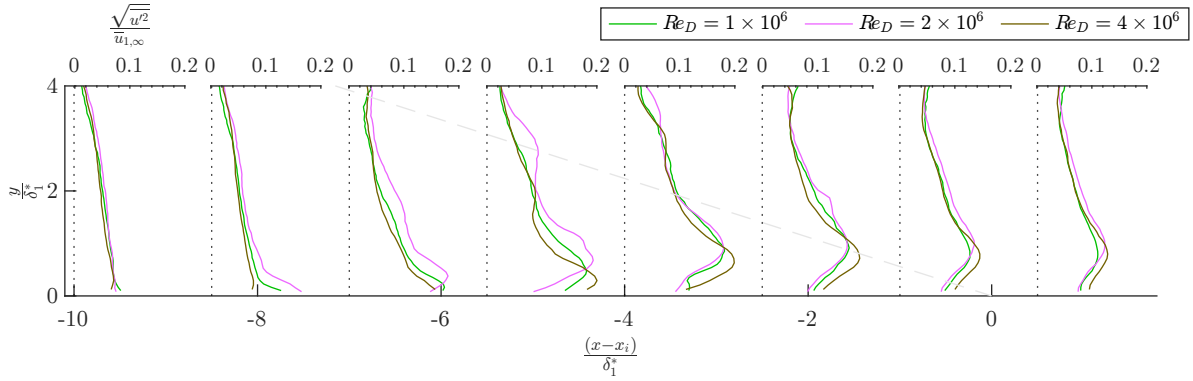

(c) α = 16°

Fig. 13 Streamwise turbulent normal stress profiles for Mach 2.5 axisymmetric interactions across the Reynolds number range for all three shock generator angles.

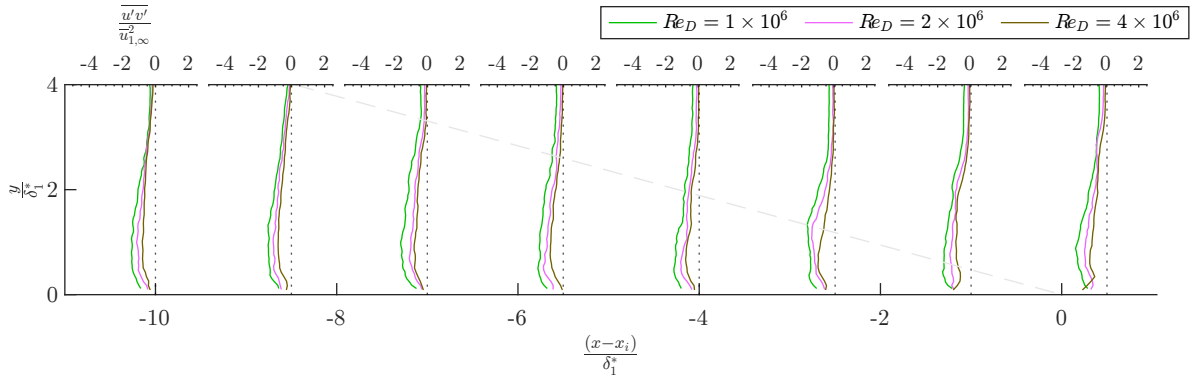

(a) α = 10°

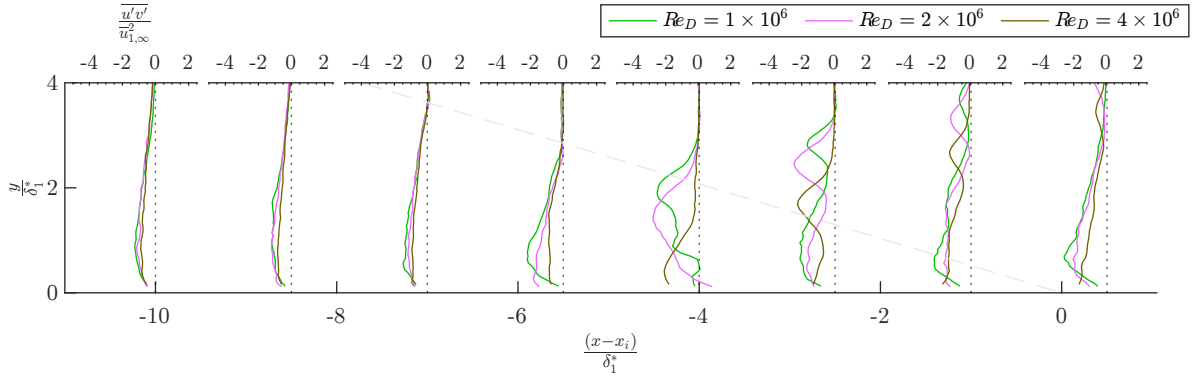

(b) α = 13.5°

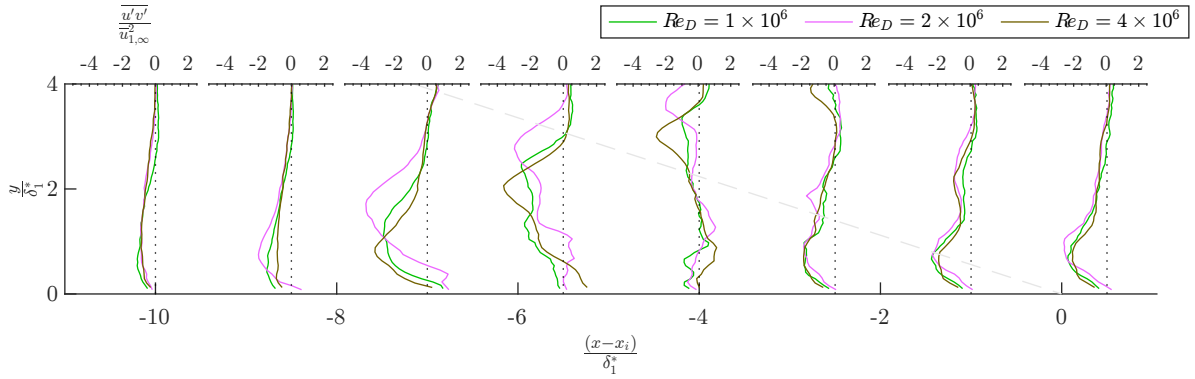

(c) α = 16°

Fig. 14 In-plane turbulent shear stress profiles for Mach 2.5 axisymmetric interactions across the Reynolds number range for all three shock generator angles.

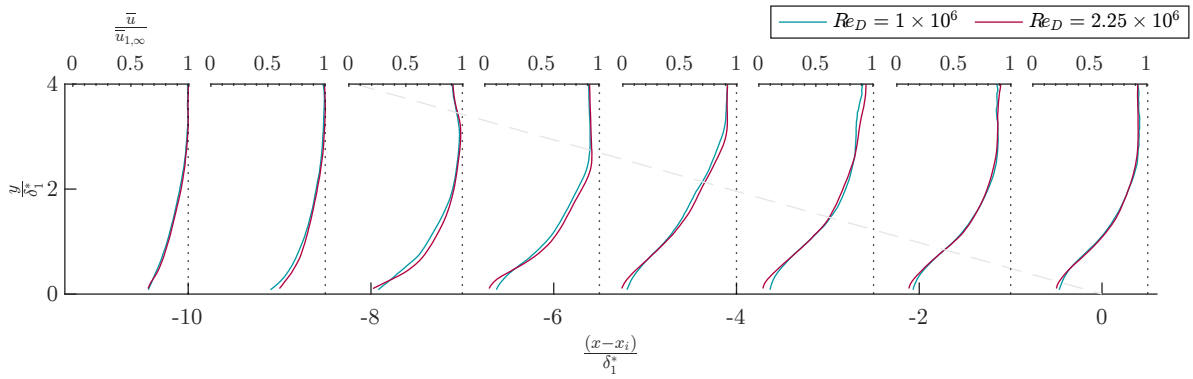

Fig. 15 Mean streamwise velocity profiles for Mach 3.0 axisymmetric interactions across the Reynolds number range at α = 16°.

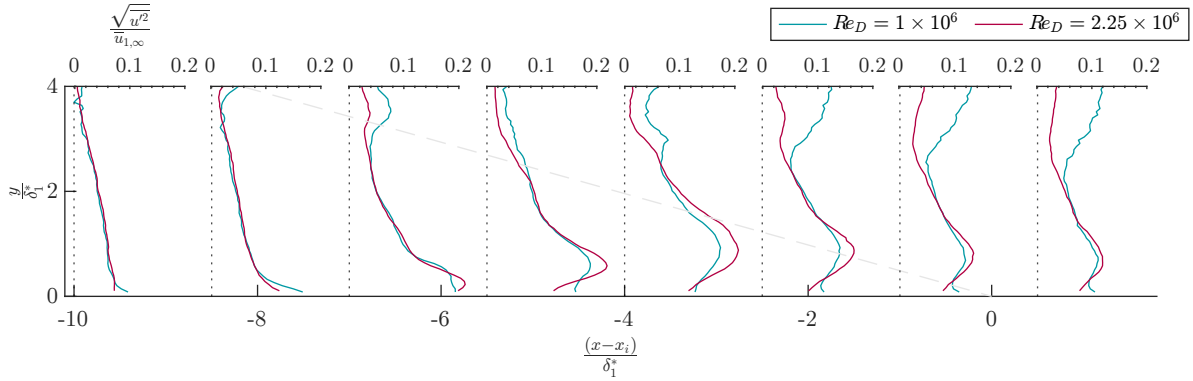

Fig. 16 Streamwise turbulent normal stress profiles for Mach 3.0 axisymmetric interactions across the Reynolds number range at α = 16°.

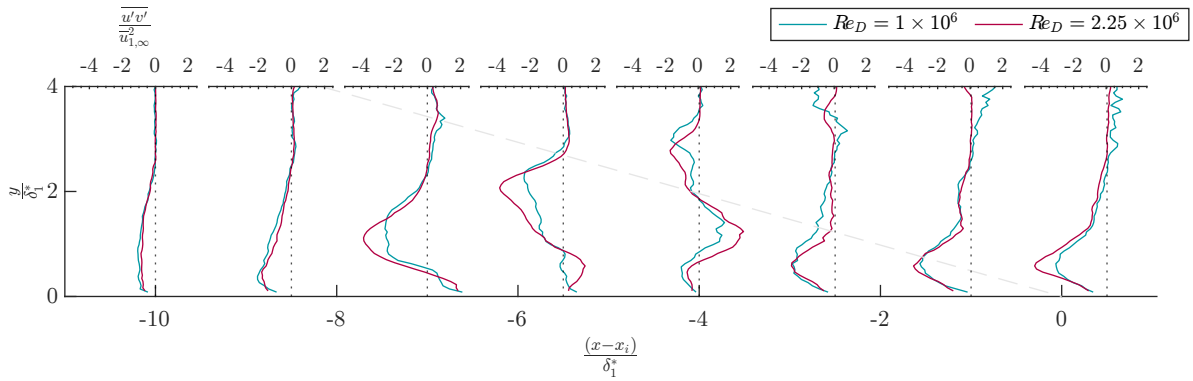

Fig. 17 In-plane turbulent shear stress profiles for Mach 3.0 axisymmetric interactions across the Reynolds number range at α = 16°.

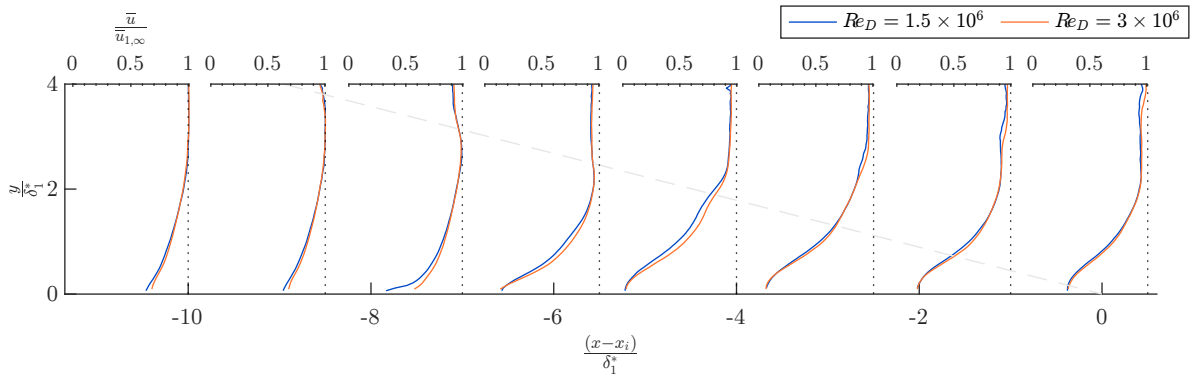

Fig. 18 Mean streamwise velocity profiles for Mach 3.5 axisymmetric interactions across the Reynolds number range at α = 16°.

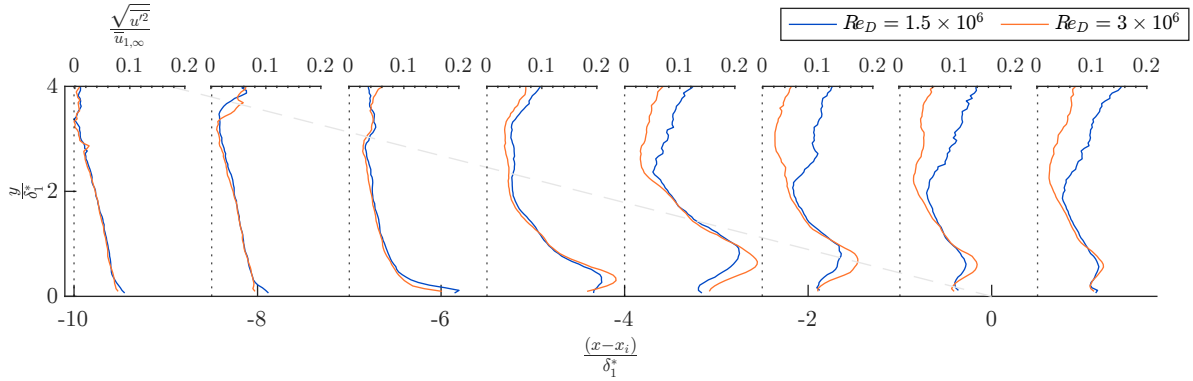

Fig. 19 Streamwise turbulent normal stress profiles for Mach 3.5 axisymmetric interactions across the Reynolds number range at α = 16°.

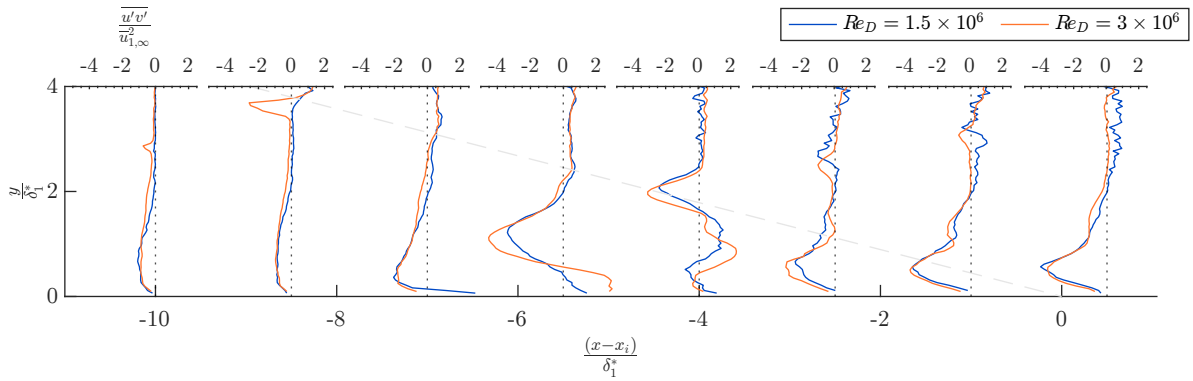

Fig. 20 In-plane turbulent shear stress profiles for Mach 3.5 axisymmetric interactions across the Reynolds number range at α = 16°.

3. Interaction Region - Fixed Stations

In the previous section, data was extracted at stations which matched a non-dimensionalized axial position. While convenient for comparison across tests run at different conditions, this uses a posteriori information about the incoming boundary layer integral parameters which is not available at the time of selecting sampling stations for probe surveys. Additionally, the time-intensive nature of probe testing limits the number of discrete sampling stations which can be explored and a balance must be struck between using close spacing within the interaction region to resolve sharp features and fully covering the behavior of the recovering boundary layer downstream of the interaction. To ensure consistency with the probe measurements which will be reported upon separately, PIV data is sampled at the same set of fixed discrete stations (6.35 mm spacing) and plotted in this section. Additionally, this data is attached in standard Tecplot® ASCII data format for public use.

As shown in Section III.A, the shock position varies slightly in the PIV configuration due to the long cantilevered length of the shock generator body. To alleviate the effect this might have on comparison between PIV results and probe or CFD data, the PIV data is extracted at physical locations which match the shock-referenced axial station, $x - x_i$, from the probe configuration. Figures 21 to 26 illustrate the data contained in the attached data files. Stepping through the mean velocity profiles from undisturbed upstream boundary layer (dark blue) to post-interaction recovery (red), the level of velocity defect and the subsequent recovery are visualized.

While the number of profiles makes these plots a bit crowded, the tighter axial sampling here allows for a more precise identification of interaction features such as the incident shock or the near-wall upstream influence extent. The larger velocity defects incurred in the stronger interactions better resolves these features. This is obvious when comparing Figs. 25b to 25d where the rapid axial velocity gradient at the reflected shock foot yields a jump from the undisturbed behavior to the profile containing peak velocity decrement from one station to the next in the $\alpha = 10°$ and 13.5° cases. At $\alpha = 16°$, this occurs across 4 profiles. Due to the larger velocity jump and greater spatial separation between the initial shock and the expansion around the cone-cylinder shoulder at Mach 2.5, Figs. 21c, 21f and 21i are the best examples to illustrate the behavior at the boundary layer edge. There, the incident shock wave can be seen intersecting the profiles progressively nearer to the wall with downstream distance up to the point of maximum edge velocity defect, which coincides with the station of minimum near-wall velocity (also approximately the same streamwise station as the apex of the separation bubble). Proceeding through the remaining profiles, the edge velocity begins to increase again up to an asymptotic value which is approximately $0.98\overline{u}_{1,\infty}$.

Similarly, the peak streamwise turbulence intensity is quantified best in these figures, as discussed in Section III.C. For the Mach 2.5 cases (Fig. 22), the maximum r.m.s. values are approximately 10%, 15%, and 20% of the freestream velocity for $\alpha = 10°$, 13.5°, and 16°, respectively, and relatively insensitive to the Reynolds number condition. As the Mach number increases to 3 in Fig. 24, the peak values become 10%, 18%, and 22%, with a slight sensitivity to Reynolds number which was noted in Section III.D.2. Finally, Fig. 26 shows that the strongest turbulence intensity appears in the Mach 3.5 cases. There, the $\alpha = 10°$ profiles shows a similar maximum value to the other Mach numbers while the $\alpha = 13.5°$ and 16° results both peak at 24% of $\overline{u}_{1,\infty}$. For all cases, the profile maximum returns approximately to the level of the incoming boundary layer with a notable shift away from the wall in the peak location.

Because these profiles continue further beyond the primary interaction region, the far-field behavior of the recovering layer is also better visualized. An interesting overall observation is that the near-wall mean velocity re-attains the value from the incoming boundary layer by the aft-most station for all but the $\alpha = 10°$ cases. Among those cases, there is also a trend with freestream Mach number, which is likely driven by the change in wave angles giving rise to a longer conical compression before the expansion from the cone-cylinder shoulder. Indeed, the Mach 2.5 result, which has the largest separation between these features, shows the slowest recovery in mean velocity.

While Figs. 21 to 26 only show streamwise velocity information for brevity, the attached files contain the three components of the mean velocity field and all six turbulent stress quantities. The files are formatted such that each sampling station is a distinct "zone" which is labeled by the probe station index and the shock-referenced axial coordinate. Within each zone, a wall-normal profile is provided at the exact spacing of the PIV cross-correlation grid. To perform non-dimensionalization of the spatial coordinates as in Section III.D.2, boundary layer parameters contained in Table 3 may be utilized. A unique file exists for each test condition with the nominal test condition identified in the filename. For specific information on the precise test condition, refer to Table 1.

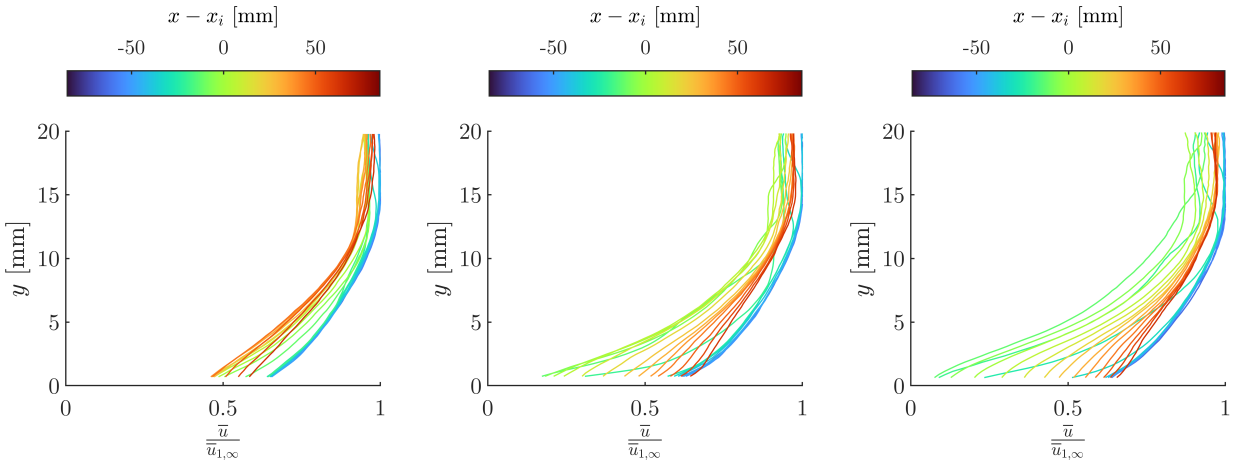

(a) $\alpha = 10°$, $Re_D = 1 \times 10^6$. **(b)** $\alpha = 13.5°$, $Re_D = 1 \times 10^6$. **(c)** $\alpha = 16°$, $Re_D = 1 \times 10^6$.

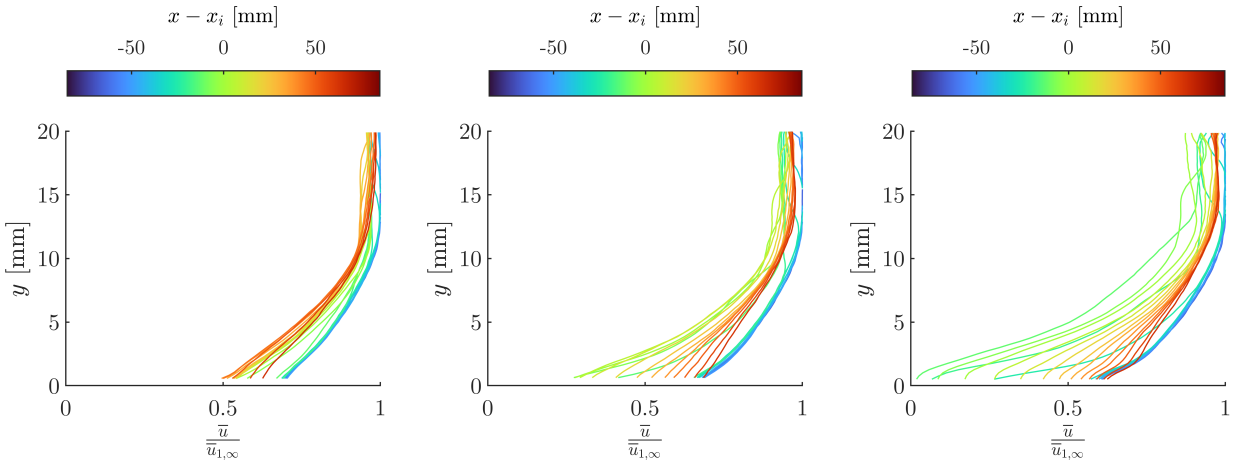

(d) $\alpha = 10°$, $Re_D = 2 \times 10^6$. **(e)** $\alpha = 13.5°$, $Re_D = 2 \times 10^6$. **(f)** $\alpha = 16°$, $Re_D = 2 \times 10^6$.

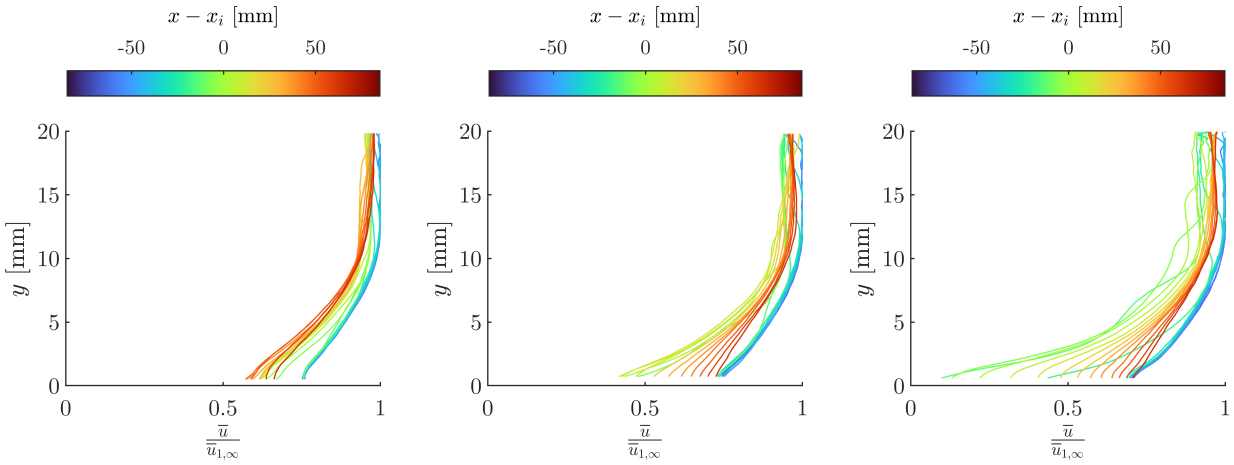

(g) $\alpha = 10°$, $Re_D = 4 \times 10^6$. **(h)** $\alpha = 13.5°$, $Re_D = 4 \times 10^6$. **(i)** $\alpha = 16°$, $Re_D = 4 \times 10^6$.

Fig. 21 Mean streamwise velocity profiles for $M_{0,\infty} = 2.5$ extracted at fixed stations matching probe sampling.

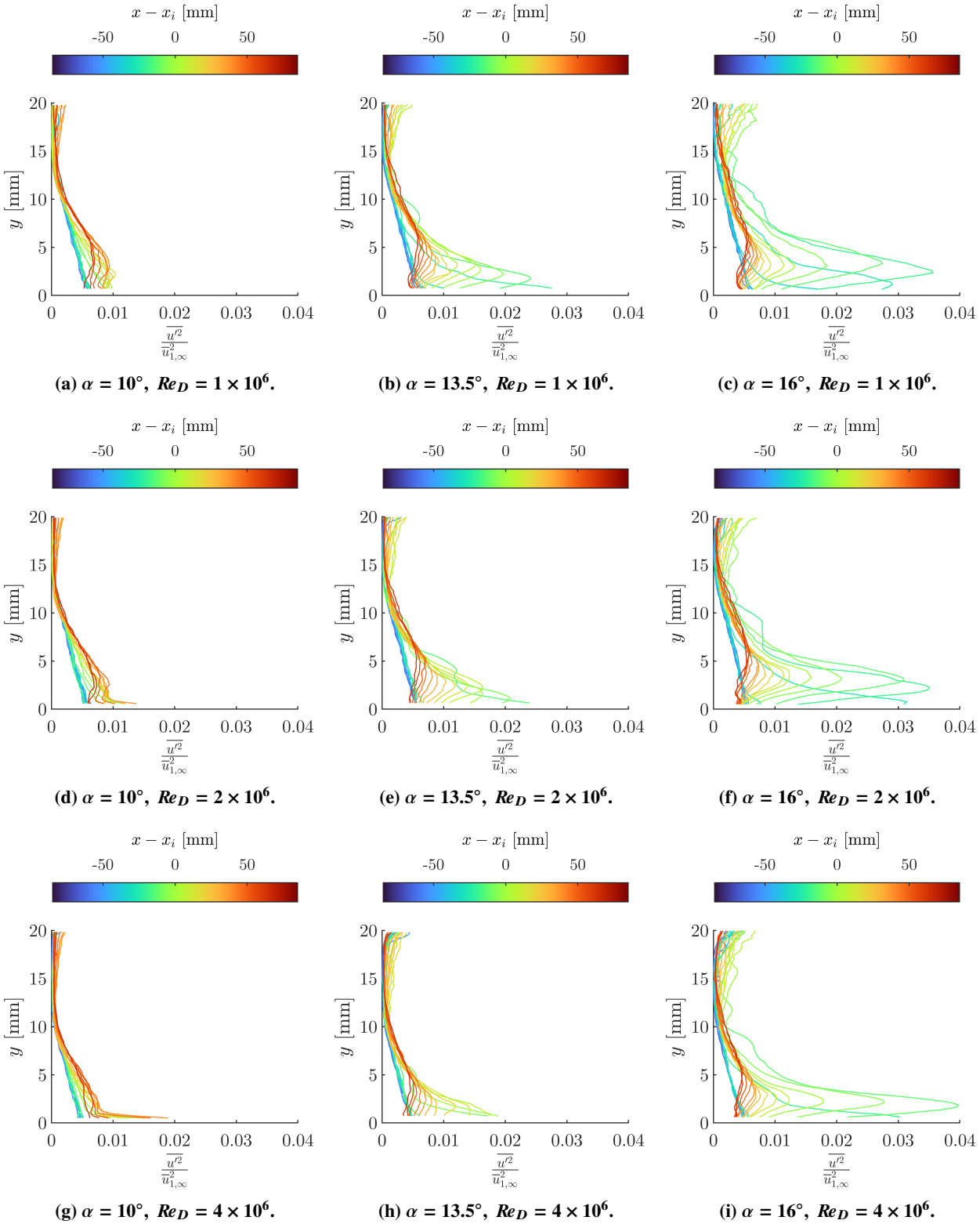

(a) $\alpha = 10°$, $Re_D = 1 \times 10^6$. **(b)** $\alpha = 13.5°$, $Re_D = 1 \times 10^6$. **(c)** $\alpha = 16°$, $Re_D = 1 \times 10^6$.

(d) $\alpha = 10°$, $Re_D = 2 \times 10^6$. **(e)** $\alpha = 13.5°$, $Re_D = 2 \times 10^6$. **(f)** $\alpha = 16°$, $Re_D = 2 \times 10^6$.

(g) $\alpha = 10°$, $Re_D = 4 \times 10^6$. **(h)** $\alpha = 13.5°$, $Re_D = 4 \times 10^6$. **(i)** $\alpha = 16°$, $Re_D = 4 \times 10^6$.

Fig. 22 Streamwise turbulence intensity profiles for $M_{0,\infty} = 2.5$ extracted at fixed stations matching probe sampling.

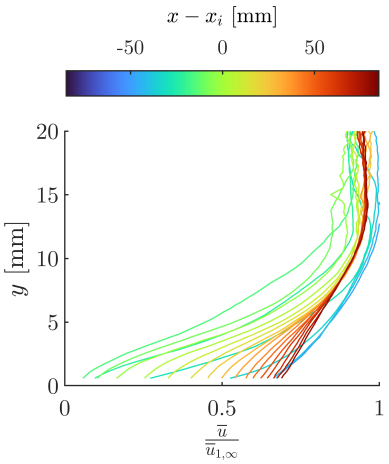

(a) α = 16°, Re_D = 1 × 10^6.

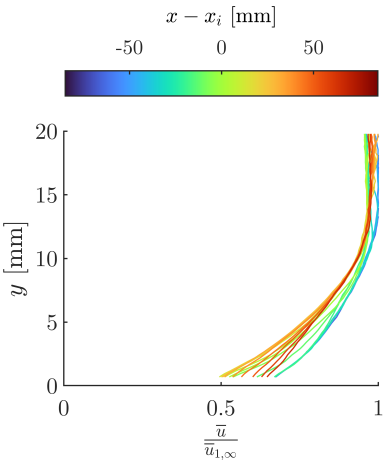

(b) α = 10°, Re_D = 2.25 × 10^6.

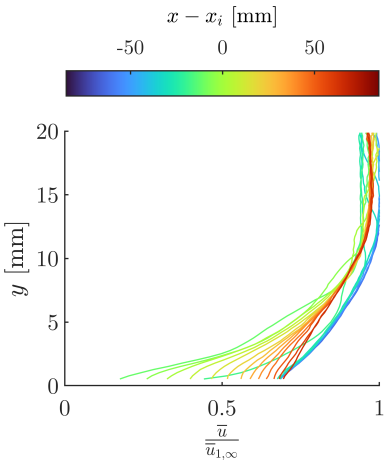

(c) α = 13.5°, Re_D = 2.25 × 10^6.

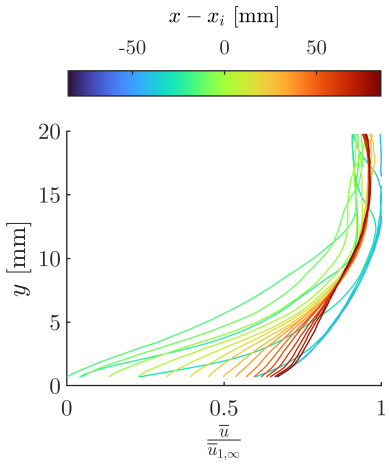

(d) α = 16°, Re_D = 2.25 × 10^6.

Fig. 23 Mean streamwise velocity profiles for $M_{0,\infty}$ = 3.0 extracted at fixed stations matching probe sampling.

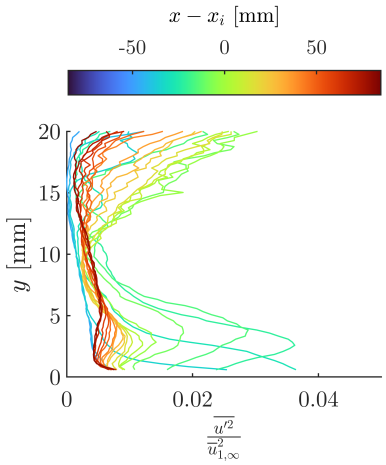

(a) α = 16°, Re_D = 1 × 10^6.

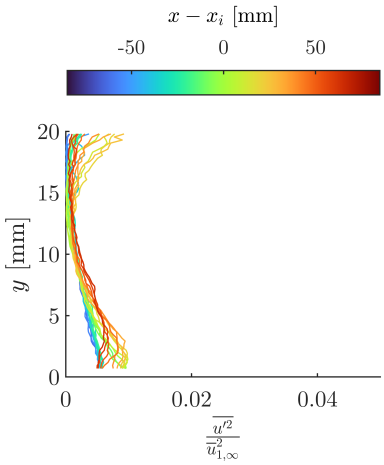

(b) α = 10°, Re_D = 2.25 × 10^6.

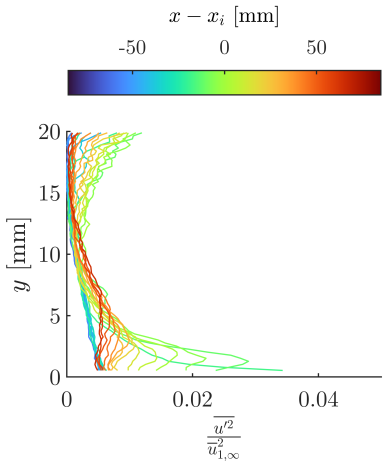

(c) α = 13.5°, Re_D = 2.25 × 10^6.

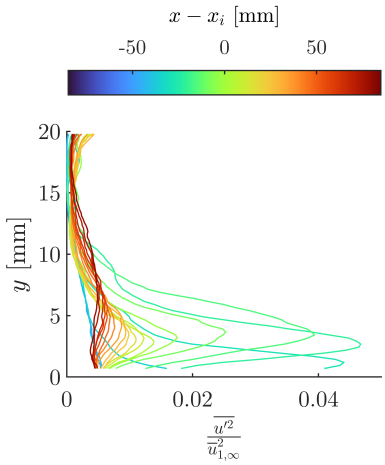

(d) α = 16°, Re_D = 2.25 × 10^6.

Fig. 24 Streamwise turbulence intensity profiles for $M_{0,\infty}$ = 3.0 extracted at fixed stations matching probe sampling.

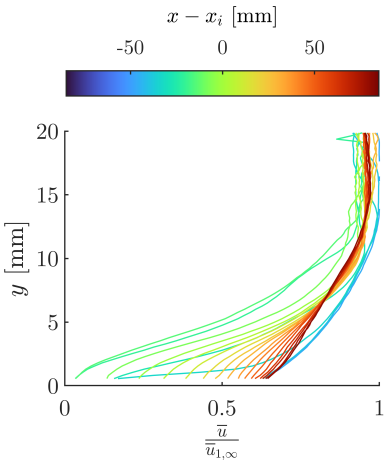

(a) α = 16°, $Re_D = 1.5 \times 10^6$.

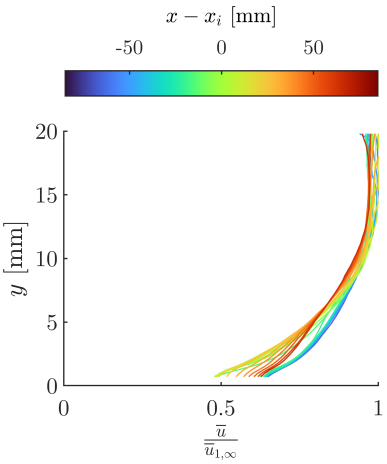

(b) α = 10°, $Re_D = 3 \times 10^6$.

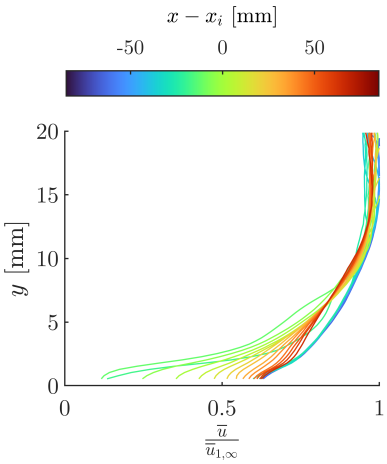

(c) α = 13.5°, $Re_D = 3 \times 10^6$.

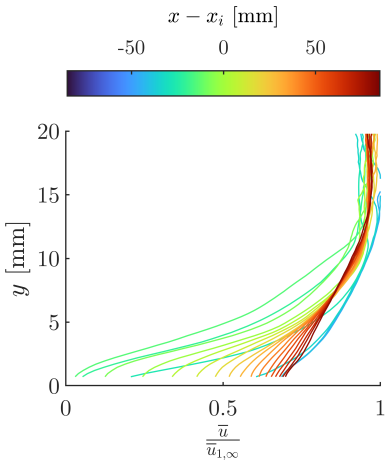

(d) α = 16°, $Re_D = 3 \times 10^6$.

Fig. 25 Mean streamwise velocity profiles for $M_{0,\infty}$ = 3.5 extracted at fixed stations matching probe sampling.

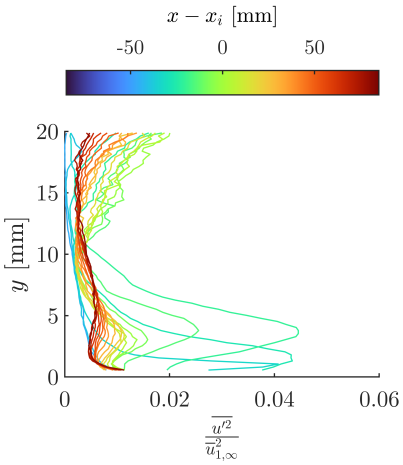

(a) α = 16°, $Re_D = 1.5 \times 10^6$.

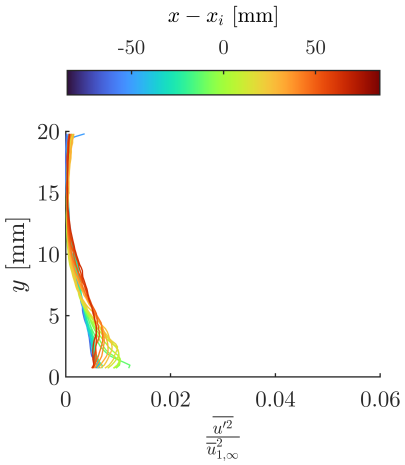

(b) α = 10°, $Re_D = 3 \times 10^6$.

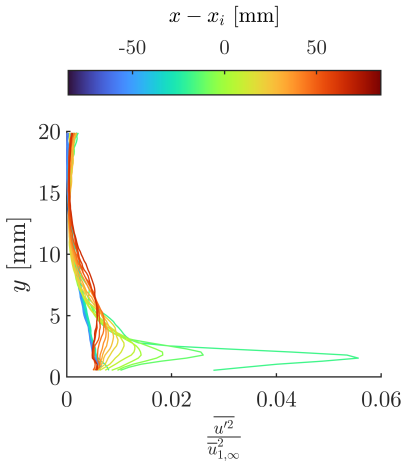

(c) α = 13.5°, $Re_D = 3 \times 10^6$.

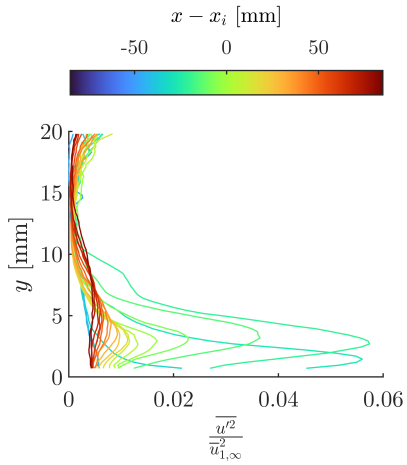

(d) α = 16°, $Re_D = 3 \times 10^6$.

Fig. 26 Streamwise turbulence intensity profiles for $M_{0,\infty}$ = 3.5 extracted at fixed stations matching probe sampling.

IV. Conclusions

This document summarizes the PIV data collection test entry completed in the spring of 2025 as part of the ongoing SWBLI experiments in the GRC 225 cm^2 Wind Tunnel at three nominal freestream Mach number conditions of 2.5, 3.0, and 3.5. Detailed post-processing methods utilized to quantify small offsets in the shock generator tip position are outlined and the results are collated herein. Thereafter, accounting for these small offsets, data are presented in coordinates which are referenced to consensus best-fit inviscid impingement locations to remove any sensitivity to small variations in the shock generator tip location.

PIV data are presented across the matrix of freestream Mach number, Reynolds number, and shock generator configurations in order to infer macroscopic trends in the data. In this report, emphasis is placed on the resultant flowfield changes with reduction in Reynolds number, as those cases are unique to this test entry. Overall, the flow behavior observed in the stitched velocity fields is in agreement with previous test entries and impinging shock interaction literature. To further explore the flow behavior in more detail, wall-normal profiles were extracted at select stations and compared directly across flow conditions. In an attempt to remove boundary layer scale effects, data were extracted at stations which matched a non-dimensional coordinate, $(x - x_i)/\delta^*$. While removing gross effects of Reynolds number on interaction scale, Reynolds number effects were found to persist within the interaction with this normalization, especially at lower freestream Mach number.

In order to facilitate use of this dataset in comparisons with CFD and other measurements, slices of the PIV data across the range of flow conditions are collated into a set of files which are attached to this document and hosted by the NASA STI office on the NASA Technical Reports Server (NTRS). A final overarching report from the HMVE campaign is forthcoming which combines results from all PIV entries along with comparisons to probe-based measurements to assess the congruence of the various datasets and elucidate flowfield behavior in regions where a particular technique is better suited.

Acknowledgments

Support for this work was provided by NASA's Transformative Aeronautics Concepts Program through the Transformational Tools & Technologies (T^3) Project. These tests were facilitated by the tireless work of the facility staff. The assistance provided by Jason Bryant, Molly Fenik, John Friscat, Celia Otero, and Brent Seifert is gratefully acknowledged. Conceptualization of the axisymmetric configuration and implementation in the 225 cm^2 Wind Tunnel is credited to David Davis, who provided invaluable support in the planning and execution of the PIV measurements.

References

[1] DeBonis, J. R., Oberkampf, W. L., Wolf, R. T., Orkwis, P. D., Turner, M. G., Babinsky, H., and Benek, J. A., "Assessment of Computational Fluid Dynamics and Experimental Data for Shock Boundary-Layer Interactions," *AIAA Journal*, Vol. 50, No. 4, 2012, pp. 891–903. doi:10.2514/1.J051341.

[2] Settles, G. S., and Dodson, L. J., "Supersonic and hypersonic shock/boundary-layer interaction database," *AIAA Journal*, Vol. 32, No. 7, 1994, pp. 1377–1383. doi:10.2514/3.12205.

[3] Aeschliman, D. P., and Oberkampf, W. L., "Experimental Methodology for Computational Fluid Dynamics Code Validation," *AIAA Journal*, Vol. 36, No. 5, 1998, pp. 733–741. doi:10.2514/2.461.

[4] Babinsky, H., Oorebeek, J., and Cottingham, T., "Corner effects in reflecting oblique shock-wave/boundary-layer interactions," *51st AIAA Aerospace Sciences Meeting including the New Horizons Forum and Aerospace Exposition*, 2013, pp. 1–11. doi:10.2514/6.2013-859.

[5] Garnier, E., "Stimulated detached eddy simulation of three-dimensional shock/boundary layer interaction," *Shock Waves*, Vol. 19, No. 6, 2009, pp. 479–486. doi:10.1007/s00193-009-0233-7.

[6] Davis, D. O., "CFD Validation Experiment of a Mach 2.5 Axisymmetric Shock-Wave/Boundary-Layer Interaction," *Proceedings of the ASME/JSMA/KSME 2015 Joint Fluids Engineering Conference*, Fluids Engineering Division Summer Meeting, Vol. Volume 1: Symposia, 2015. doi:10.1115/AJKFluids20156342, v001T06A001.

[7] Sasson, J., "Conical Shock Wave Turbulent Boundary Layer Interactions in a Circular Test Section at Mach 2.5," Ph.D. thesis, Case Western Reserve University, 2022.

[8] Sasson, J., Reising, H. H., Davis, D. O., and Barnhart, P. J., "Summary of Shock Wave Turbulent Boundary Layer Interaction Experiments In a Circular Test Section," *AIAA SciTech 2023*, 2023. doi:10.2514/6.2023-0442.

[9] Reising, H. H., and Davis, D. O., "PIV Measurements of Shock-Wave/Boundary-Layer Interactions at Mach 2.5 in a Circular Test Section," *AIAA SCITECH 2024 Forum*, American Institute of Aeronautics and Astronautics, 2024. doi:10.2514/6.2024-2554.

[10] Reising, H. H., Sasson, J. S., Davis, D. O., Friedlander, D. F., and Howerton, L. W., "Cross-Measurement Comparisons for a CFD Validation Dataset on Mach 2.5 Axisymmetric Turbulent Shock-Wave/Boundary-Layer Interactions," *AIAA SciTech 2025*, 2025. doi:10.2514/6.2025-0474.

[11] Reising, H. H., and Davis, D. O., "Development and Assessment of a New Particle Image Velocimetry System in the NASA GRC 225 cm^2 Wind Tunnel," *AIAA SciTech 2023*, National Harbor, MD, 2023. doi:10.2514/6.2023-0631.

[12] Reising, H., "Turbulent Shock-Wave/Boundary-Layer Interactions Without Sidewall Effects at Mach 2.5, 3.0, and 3.5 — PIV Measurements from 2024 Test Entry," *NASA/TM-20250004046*, 2025.

[13] Friedlander, D. J., Georgiadis, N. J., Howerton, L. W., and Reising, H. H., "Numerical Simulations of an Axisymmetric Shock-Wave/Boundary-Layer Interaction," *AIAA SciTech 2025 Forum*, 2025. doi:10.2514/6.2025-2065.

[14] Pirozzoli, S., and Smits, A. J., "Outer-layer universality of the mean velocity profile in turbulent wall-bounded flows," *Physical Review Fluids*, Vol. 8, No. 6, 2023, p. 064607. doi:10.1103/physrevfluids.8.064607.

[15] Fernholz, H., and Finley, P., "The incompressible zero-pressure-gradient turbulent boundary layer: An assessment of the data," *Progress in Aerospace Sciences*, Vol. 32, No. 4, 1996, pp. 245–311. doi:10.1016/0376-0421(95)00007-0.

[16] Rotta, J., "On the theory of the turbulent boundary layer," Tech. rep., National Advisory Committee for Aeronautics, 1953.

[17] Clauser, F. H., "Turbulent Boundary Layers in Adverse Pressure Gradients," *Journal of the Aeronautical Sciences*, Vol. 21, No. 2, 1954, pp. 91–108. doi:10.2514/8.2938.

[18] Fernholz, P. J., H. H. ; Finley, "A Critical Commentary on Mean Flow Data for Two-Dimensional Compressible Turbulent Boundary Layers," Tech. rep., Advisory Group for Aerospace Research and Development, 1980.

[19] Humble, R. A., Scarano, F., and Van Oudheusden, B. W., "Particle image velocimetry measurements of a shock wave/turbulent boundary layer interaction," *Experiments in Fluids*, Vol. 43, No. 2-3, 2007, pp. 173–183. doi:10.1007/s00348-007-0337-8.

[20] Baidya, R., Scharnowski, S., Bross, M., and Kähler, C. J., "Interactions between a shock and turbulent features in a Mach 2 compressible boundary layer," *Journal of Fluid Mechanics*, Vol. 893, 2020, p. A15. doi:10.1017/jfm.2020.208.

[21] Touber, E., and Sandham, N. D., "Large-eddy simulation of low-frequency unsteadiness in a turbulent shock-induced separation bubble," *Theoretical and Computational Fluid Dynamics*, Vol. 23, No. 2, 2009, pp. 79–107. doi:10.1007/s00162-009-0103-z.

[22] Settles, G. S., Bogdonoff, S. M., and Vas, I. E., "Incipient Separation of a Supersonic Turbulent Boundary Layer at High Reynolds Numbers," *AIAA Journal*, Vol. 14, No. 1, 1976, pp. 50–56. doi:10.2514/3.61331.

[23] Laguarda, L., Hickel, S., Schrijer, F., and van Oudheusden, B., "Reynolds number effects in shock-wave/turbulent boundary-layer interactions," *Journal of Fluid Mechanics*, Vol. 989, 2024. doi:10.1017/jfm.2024.361.

[24] Souverein, L. J., Bakker, P. G., and Dupont, P., "A scaling analysis for turbulent shock-wave/boundary-layer interactions," *Journal of Fluid Mechanics*, Vol. 714, 2013, pp. 505–535. doi:10.1017/jfm.2012.495.

Appendix - Stitched PIV Velocity Fields

1. Mach 2.5 Freestream

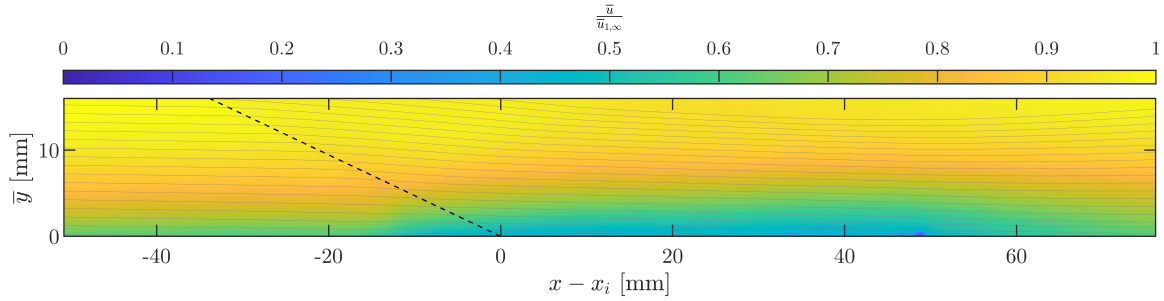

(a) $Re_D = 1 \times 10^6$

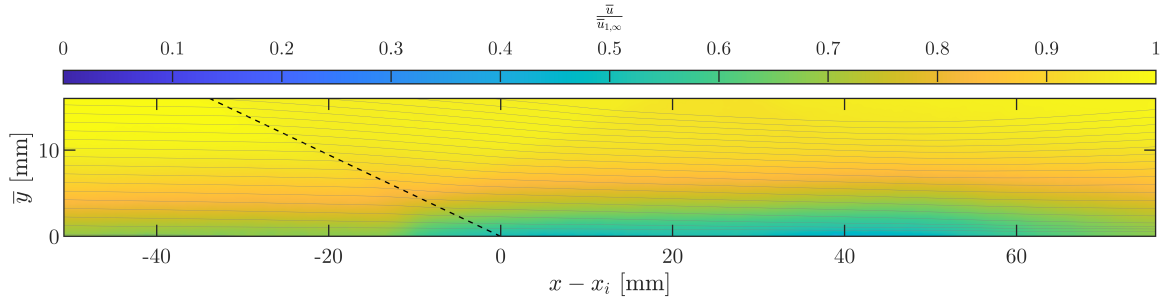

(b) $Re_D = 2 \times 10^6$

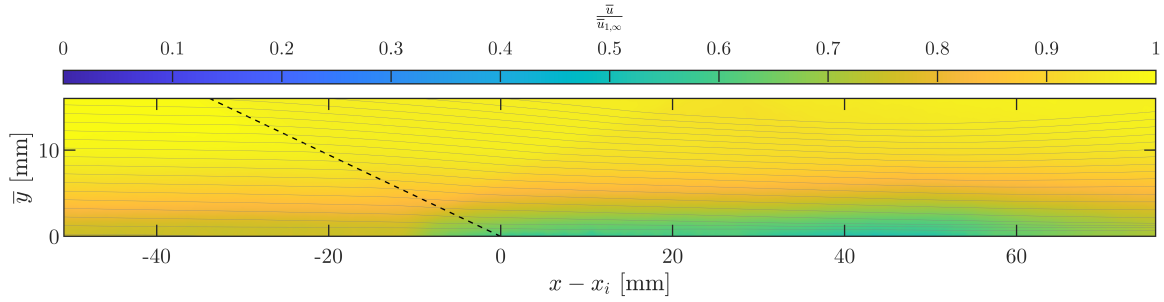

(c) $Re_D = 4 \times 10^6$

Fig. A1 Axial velocity fields in Mach 2.5 axisymmetric $\alpha = 10°$ interaction across Reynolds number settings.

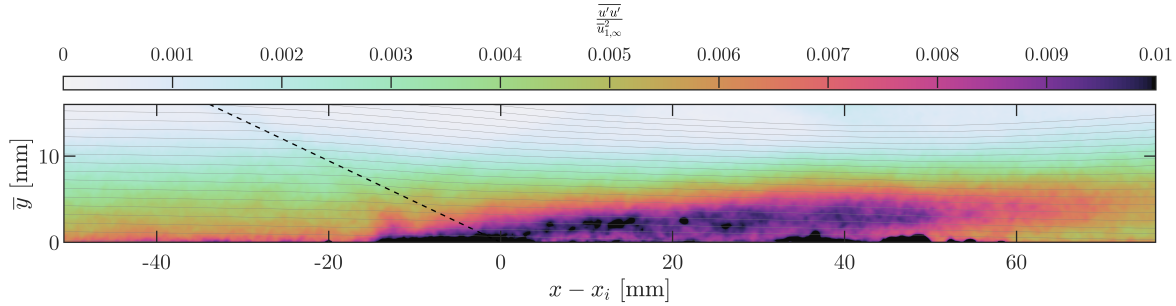

(a) $Re_D = 1 \times 10^6$

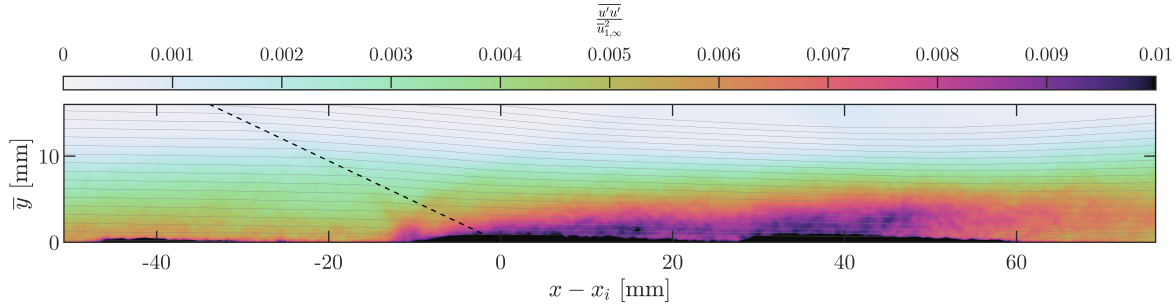

(b) $Re_D = 2 \times 10^6$

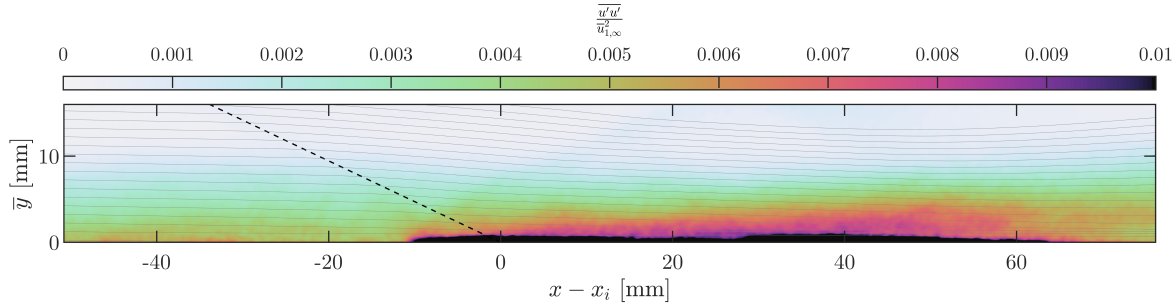

(c) $Re_D = 4 \times 10^6$

Fig. A2 Axial turbulence intensity fields in Mach 2.5 axisymmetric $\alpha = 10°$ interaction across Reynolds number settings.

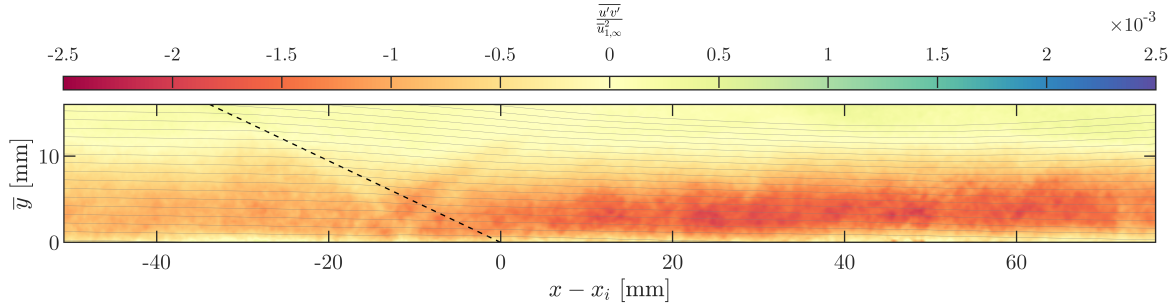

(a) $Re_D = 1 \times 10^6$

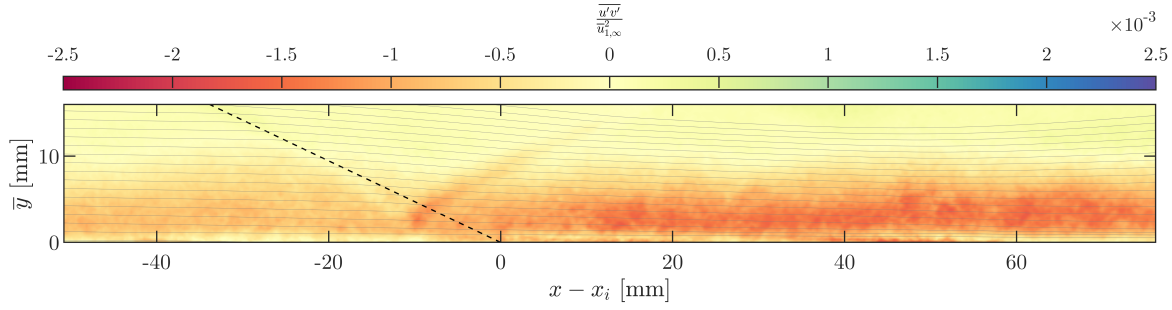

(b) $Re_D = 2 \times 10^6$

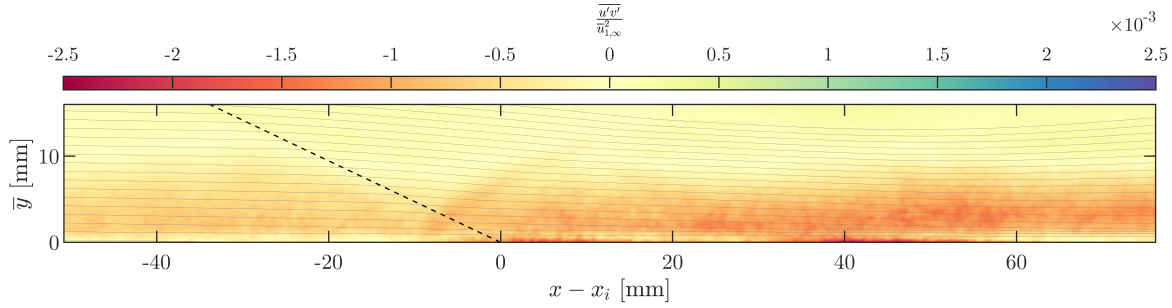

(c) $Re_D = 4 \times 10^6$

Fig. A3 Shear stress fields in Mach 2.5 axisymmetric $\alpha = 10°$ interaction across Reynolds number settings.

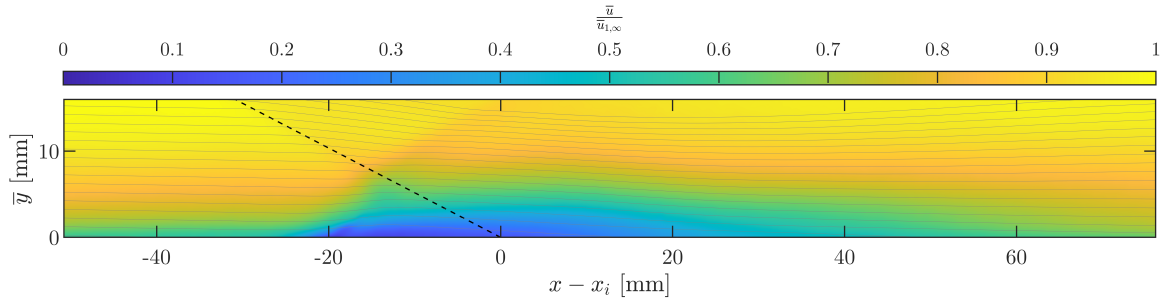

(a) $Re_D = 1 \times 10^6$

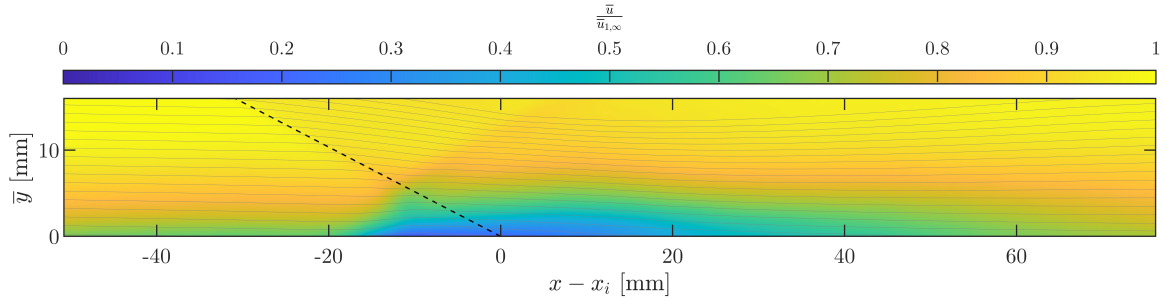

(b) $Re_D = 2 \times 10^6$

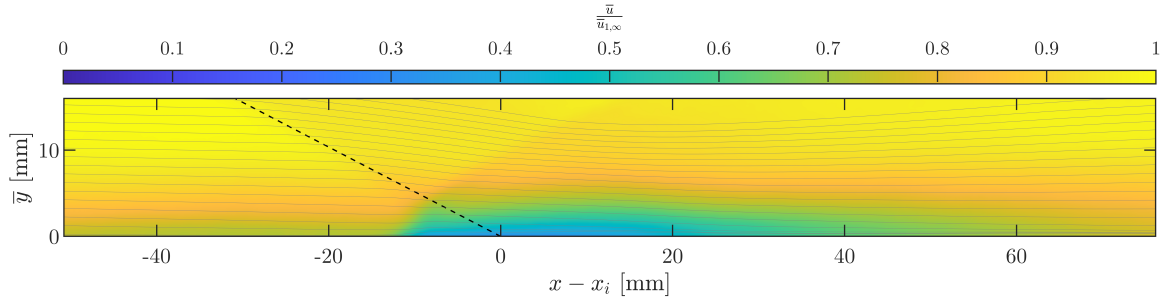

(c) $Re_D = 4 \times 10^6$

Fig. A4 Axial velocity fields in Mach 2.5 axisymmetric $\alpha = 13.5°$ interaction across Reynolds number settings.

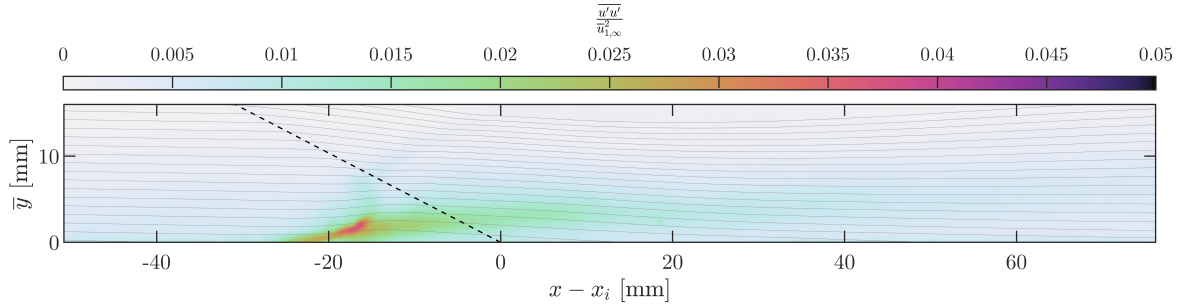

(a) $Re_D = 1 \times 10^6$

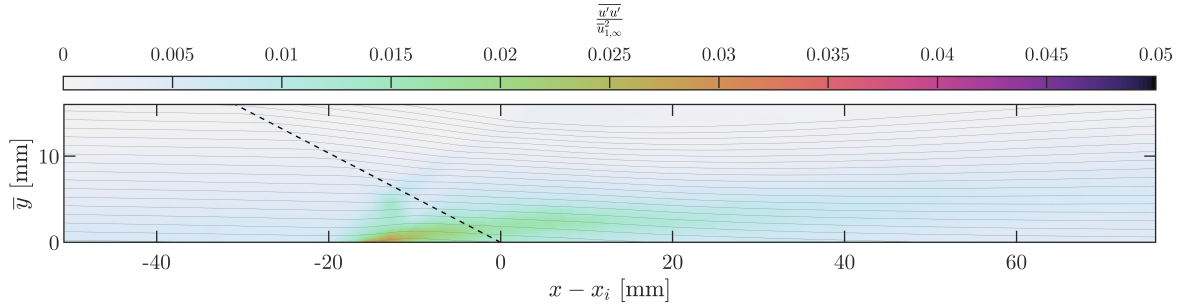

(b) $Re_D = 2 \times 10^6$

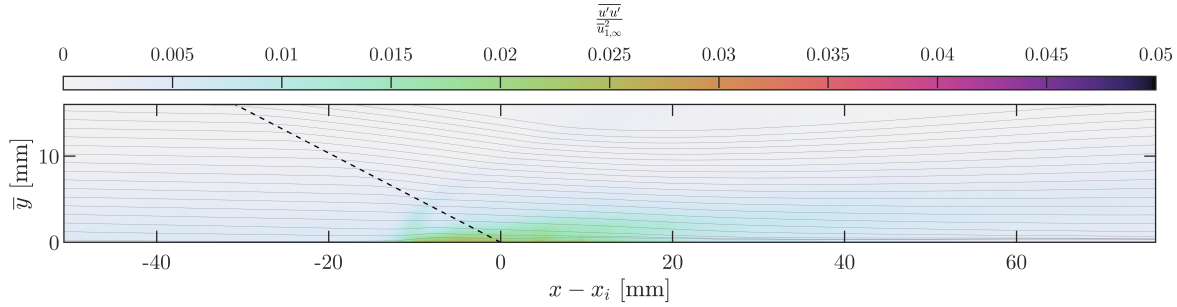

(c) $Re_D = 4 \times 10^6$

Fig. A5 Axial turbulence intensity fields in Mach 2.5 axisymmetric $\alpha = 13.5°$ interaction across Reynolds number settings.

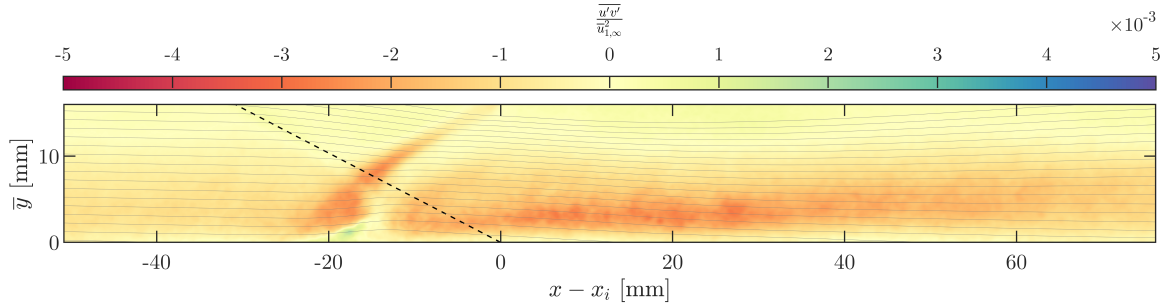

(a) $Re_D = 1 \times 10^6$

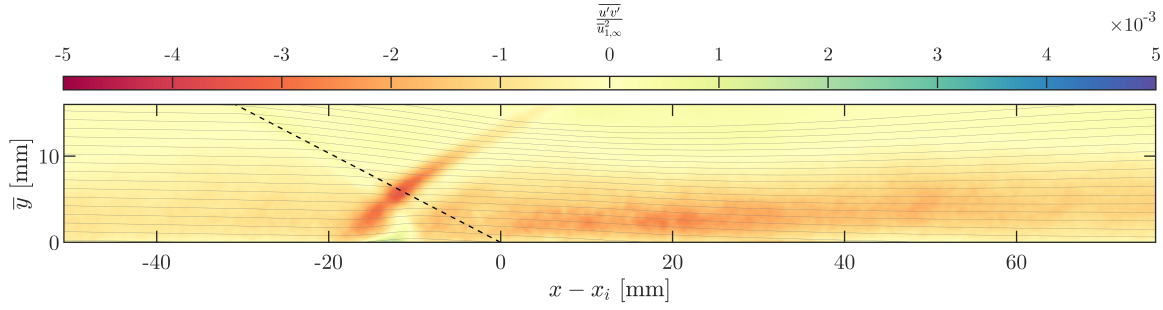

(b) $Re_D = 2 \times 10^6$

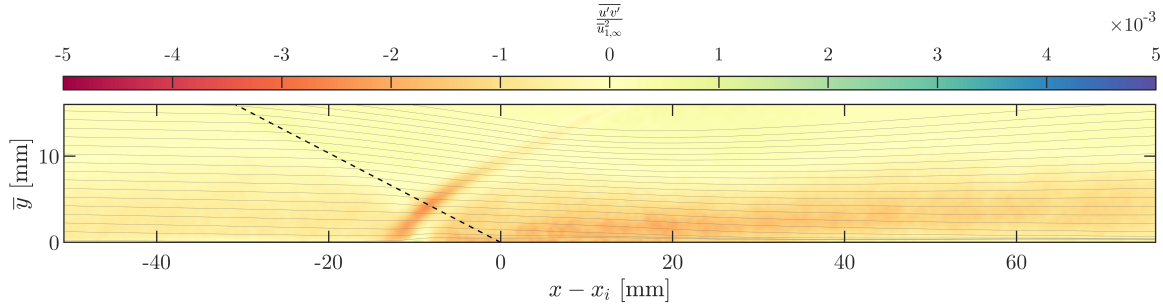

(c) $Re_D = 4 \times 10^6$

Fig. A6 Shear stress fields in Mach 2.5 axisymmetric $\alpha = 13.5°$ interaction across Reynolds number settings.

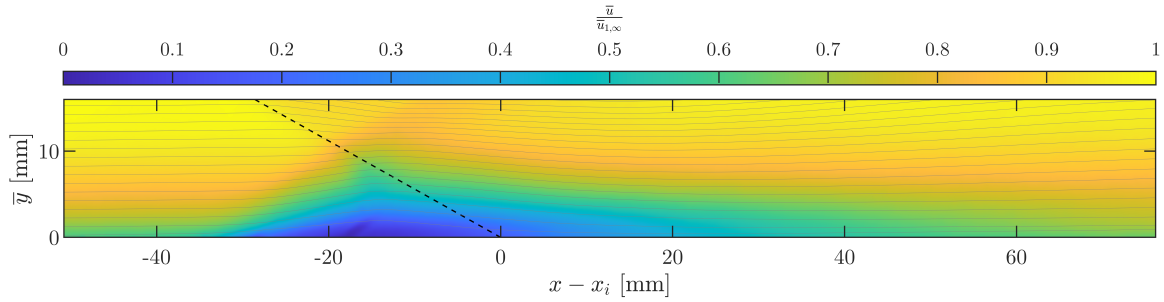

(a) $Re_D = 1 \times 10^6$

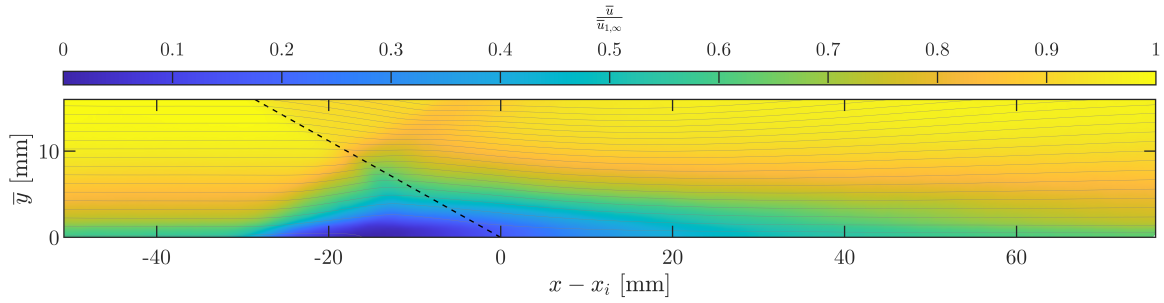

(b) $Re_D = 2 \times 10^6$

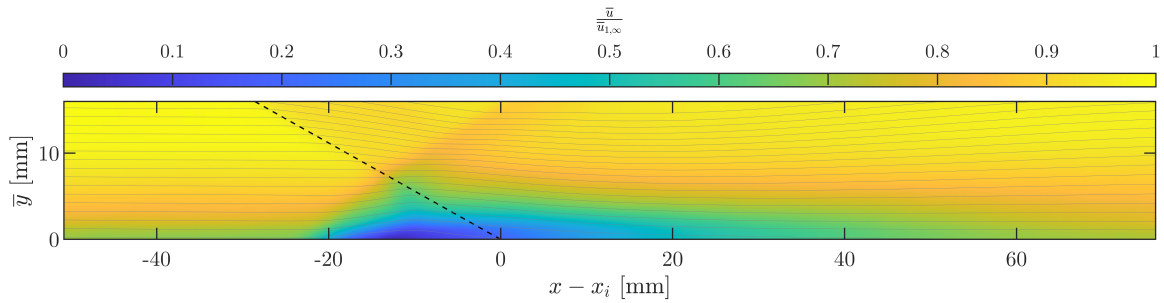

(c) $Re_D = 4 \times 10^6$

Fig. A7 Axial velocity fields in Mach 2.5 axisymmetric $\alpha = 16°$ interaction across Reynolds number settings.

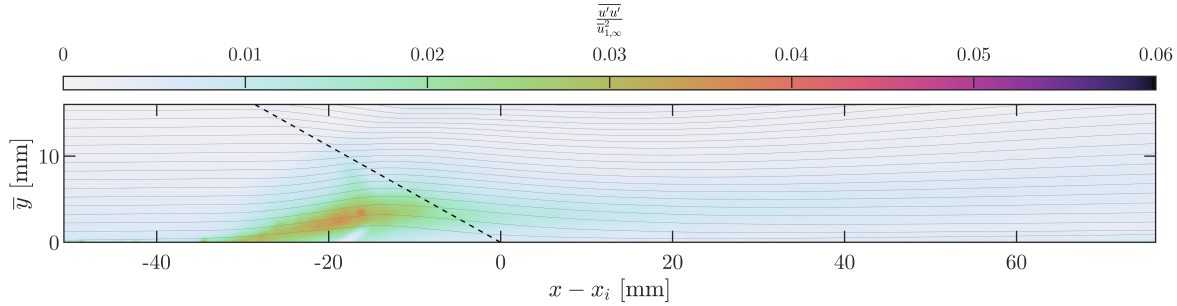

(a) $Re_D = 1 \times 10^6$

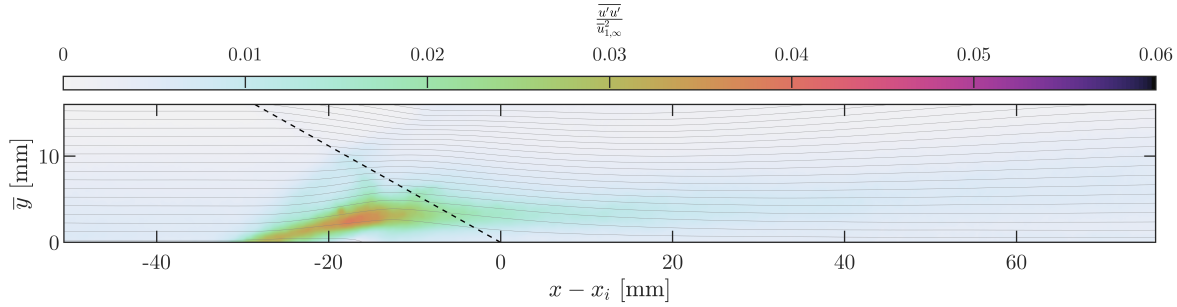

(b) $Re_D = 2 \times 10^6$

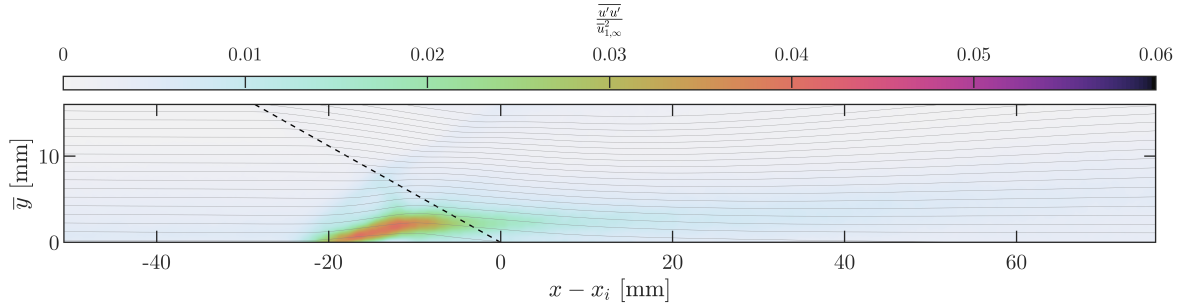

(c) $Re_D = 4 \times 10^6$

Fig. A8 Axial turbulence intensity fields in Mach 2.5 axisymmetric $\alpha = 16°$ interaction across Reynolds number settings.

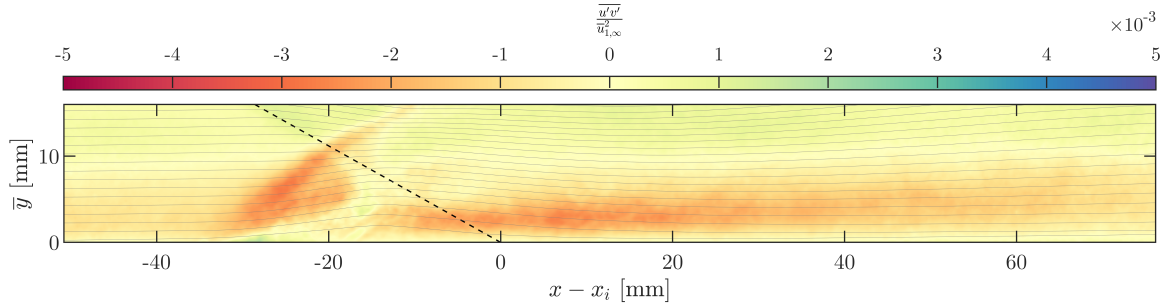

(a) $Re_D = 1 \times 10^6$

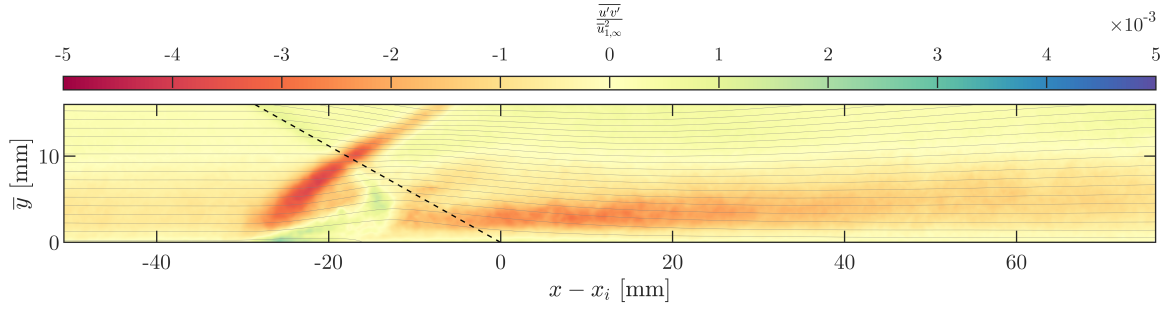

(b) $Re_D = 2 \times 10^6$

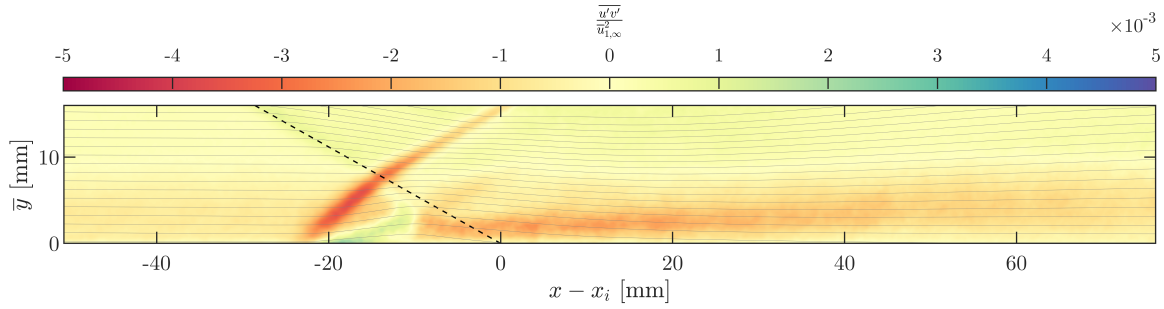

(c) $Re_D = 4 \times 10^6$

Fig. A9 Shear stress fields in Mach 2.5 axisymmetric $\alpha = 16°$ interaction across Reynolds number settings.

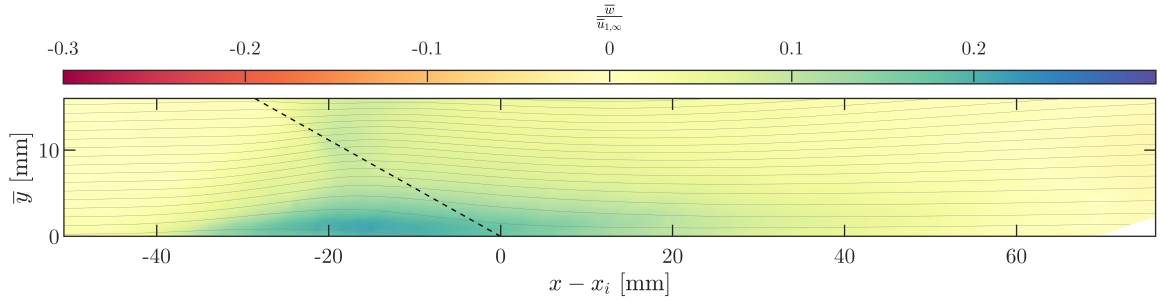

(a) $Re_D = 1 \times 10^6$

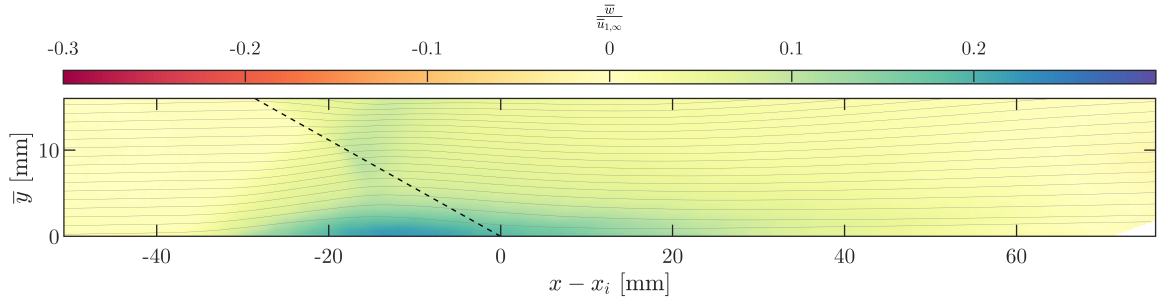

(b) $Re_D = 2 \times 10^6$

Fig. A10 Through-plane velocity fields in Mach 2.5, $\alpha = 16°$ swept ($\ell = R_{TS}/4, \theta = 90°$) interaction at the two Reynolds number conditions tested.

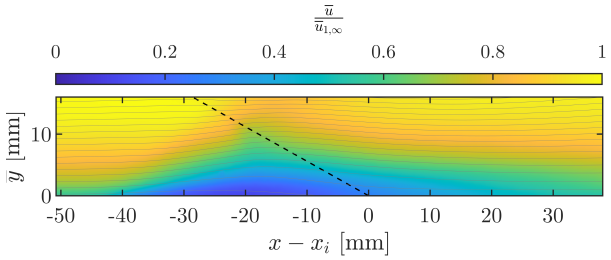

(a) $Re_D = 1 \times 10^6$, swept.

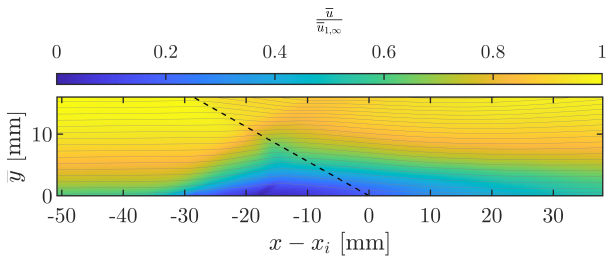

(b) $Re_D = 1 \times 10^6$, axisymmetric.

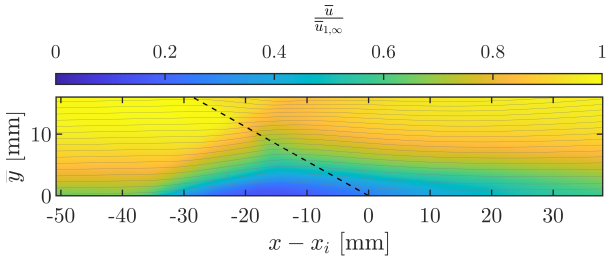

(c) $Re_D = 2 \times 10^6$, swept.

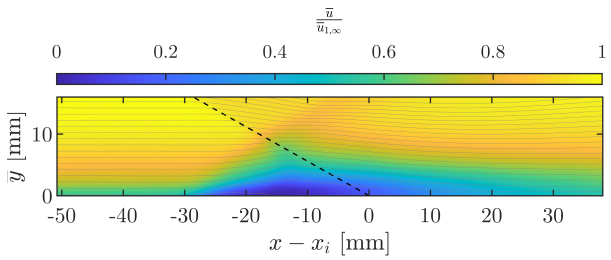

(d) $Re_D = 2 \times 10^6$, axisymmetric.

Fig. A11 Axial velocity field comparison between swept ($\ell = R_{TS}/4, \theta = 90°$) and axisymmetric ($\ell = 0$) interaction behavior near impingement at Mach 2.5 and $\alpha = 16°$.

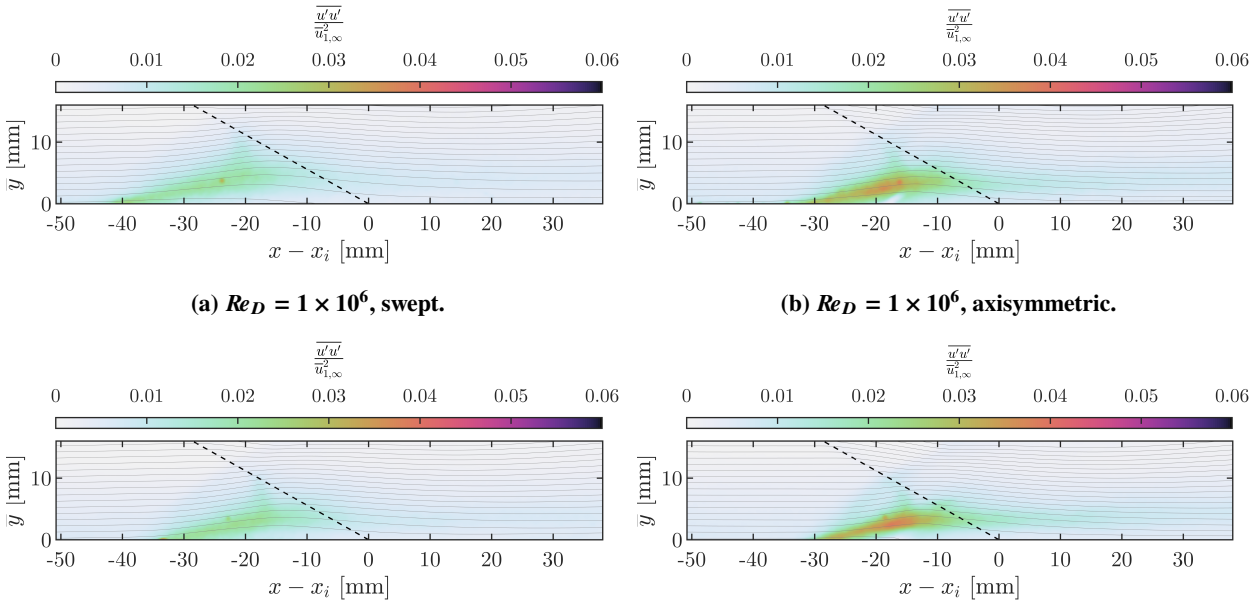

(a) $Re_D = 1 \times 10^6$, swept. **(b) $Re_D = 1 \times 10^6$, axisymmetric.**

(c) $Re_D = 2 \times 10^6$, swept. **(d) $Re_D = 2 \times 10^6$, axisymmetric.**

Fig. A12 Axial turbulence intensity comparison between swept ($\ell = R_{TS}/4, \theta = 90°$) and axisymmetric ($\ell = 0$) interaction behavior near impingement at Mach 2.5 and $\alpha = 16°$.

2. Mach 3.0 Freestream

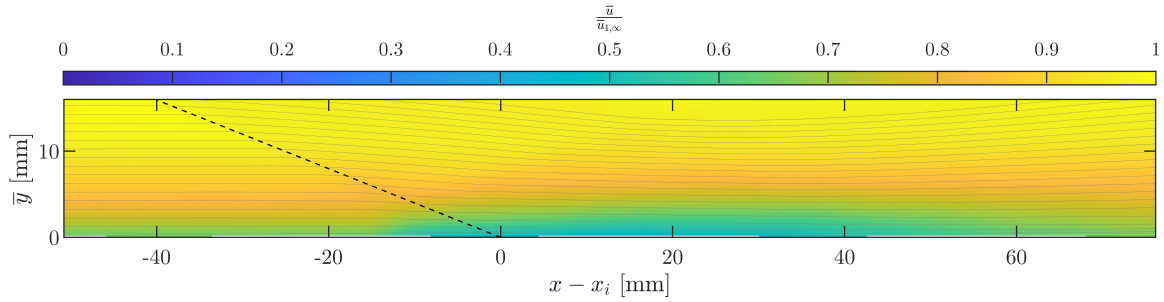

Fig. A13 Axial velocity fields in Mach 3.0 axisymmetric α = 10° interaction at $Re_D = 2.25 \times 10^6$.

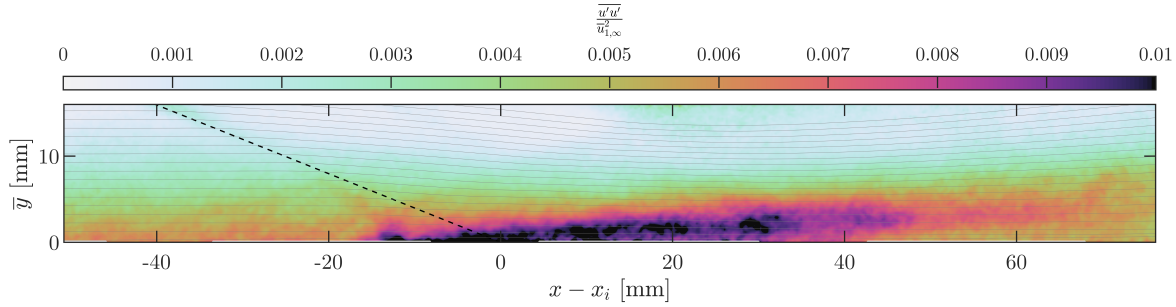

Fig. A14 Axial turbulence intensity fields in Mach 3.0 axisymmetric α = 10° interaction at $Re_D = 2.25 \times 10^6$.

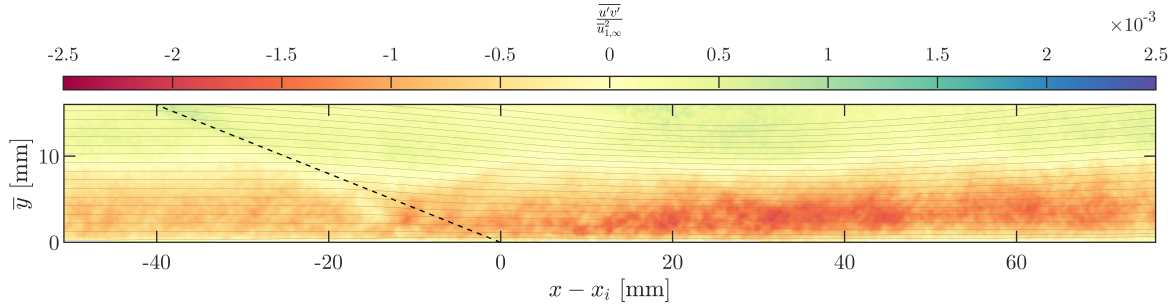

Fig. A15 Shear stress fields in Mach 3.0 axisymmetric α = 10° interaction at $Re_D = 2.25 \times 10^6$.

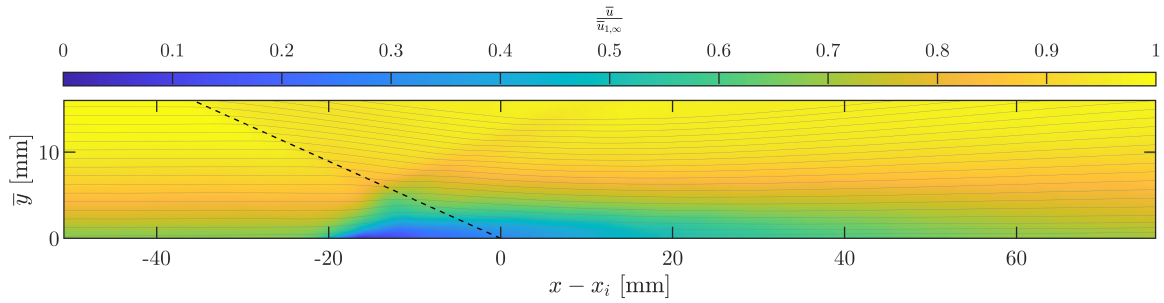

Fig. A16 Axial velocity fields in Mach 3.0 axisymmetric α = 13.5° interaction at $Re_D = 2.25 \times 10^6$.

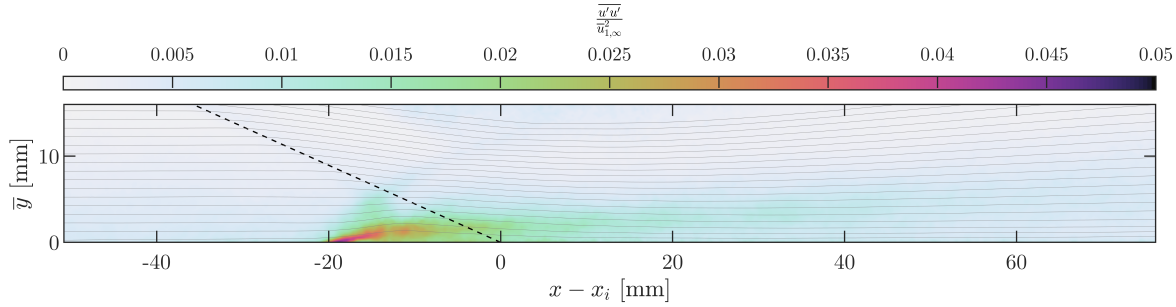

Fig. A17 Axial turbulence intensity fields in Mach 3.0 axisymmetric α = 13.5° interaction at $Re_D = 2.25 \times 10^6$.

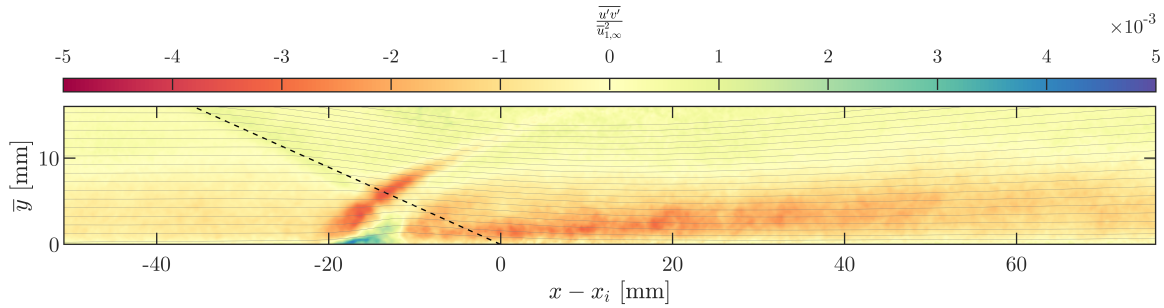

Fig. A18 Shear stress fields in Mach 3.0 axisymmetric α = 13.5° interaction at $Re_D = 2.25 \times 10^6$.

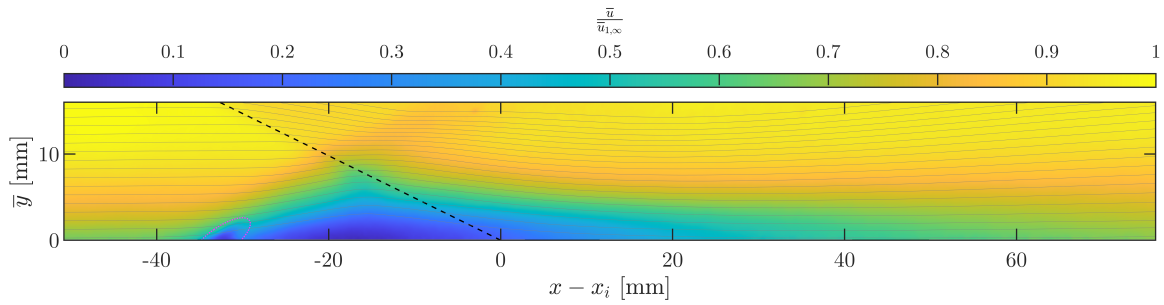

(a) $Re_D = 1 \times 10^6$

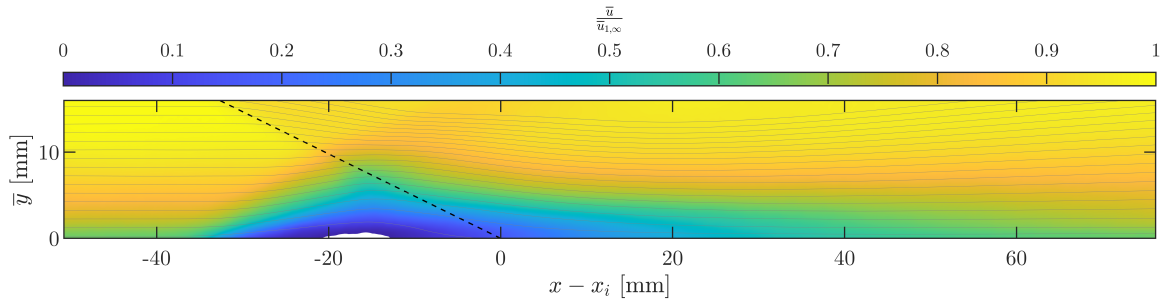

(b) $Re_D = 2.25 \times 10^6$

Fig. A19 Axial velocity fields in Mach 3.0 axisymmetric $\alpha = 16°$ interaction at the two Reynolds number conditions tested.

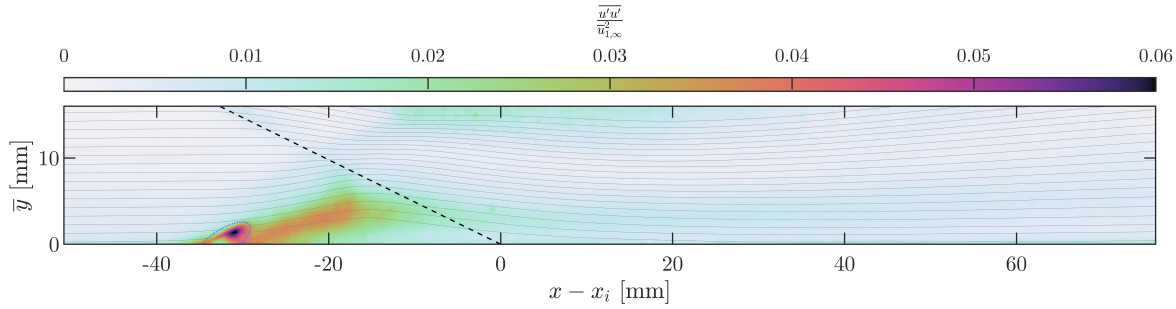

(a) $Re_D = 1 \times 10^6$

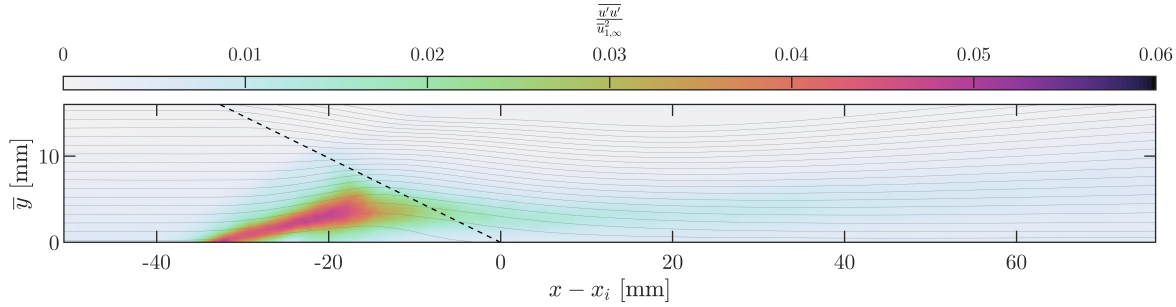

(b) $Re_D = 2.25 \times 10^6$

Fig. A20 Axial turbulence intensity fields in Mach 3.0 axisymmetric $\alpha = 16°$ interaction at the two Reynolds number conditions tested.

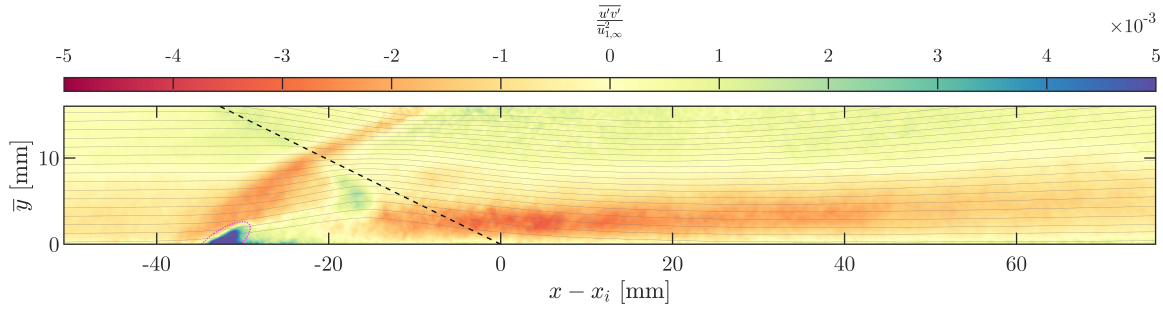

(a) $Re_D = 1 \times 10^6$

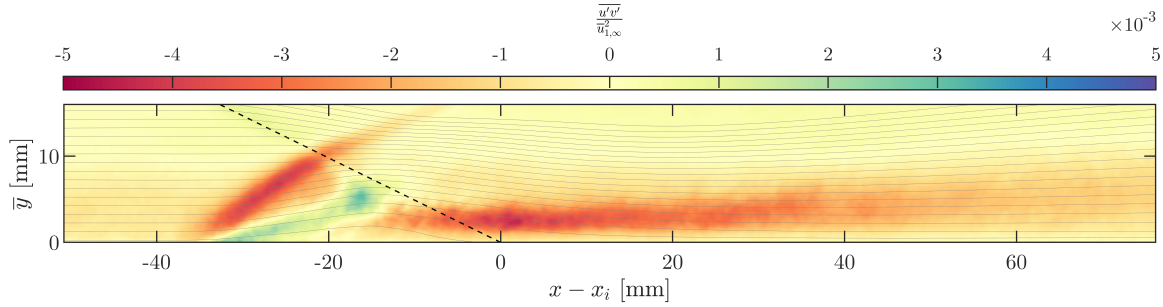

(b) $Re_D = 2.25 \times 10^6$

Fig. A21 Shear stress fields in Mach 3.0 axisymmetric $\alpha = 16°$ interaction at the two Reynolds number conditions tested.

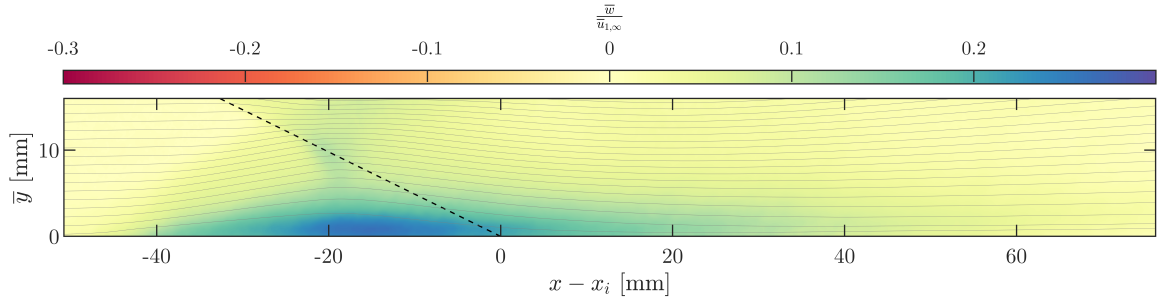

(a) $Re_D = 1 \times 10^6$

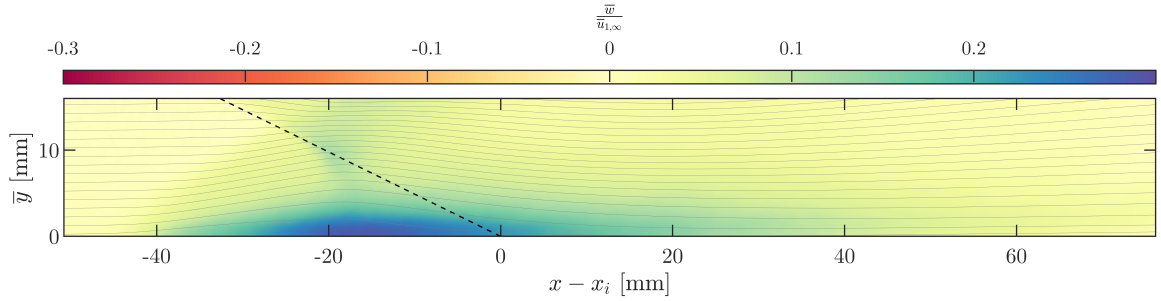

(b) $Re_D = 2.25 \times 10^6$

Fig. A22 Through-plane velocity fields in Mach 3.0, $\alpha = 16°$ swept ($\ell = R_{TS}/4, \theta = 90°$) interaction at the two Reynolds number conditions tested.

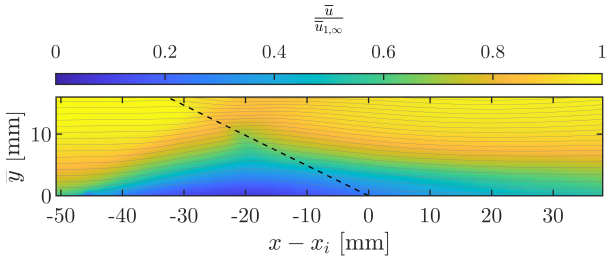

(a) $Re_D = 1 \times 10^6$, swept.

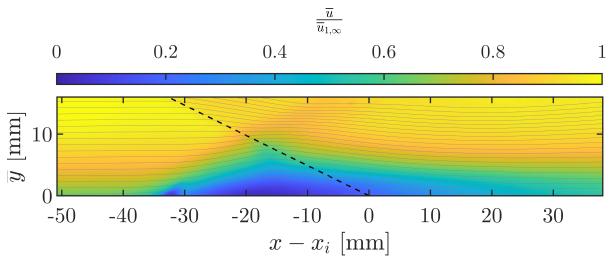

(b) $Re_D = 1 \times 10^6$, axisymmetric.

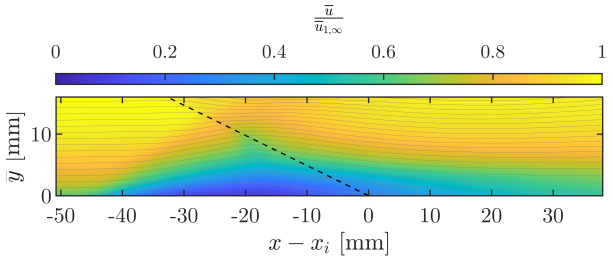

(c) $Re_D = 2.25 \times 10^6$, swept.

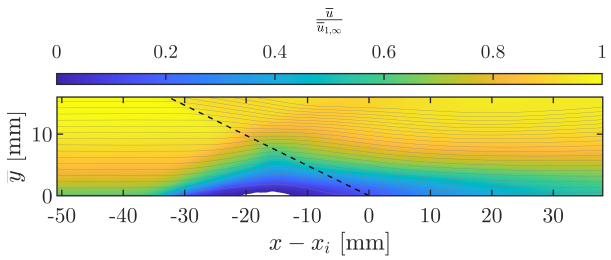

(d) $Re_D = 2.25 \times 10^6$, axisymmetric.

Fig. A23 Axial velocity field comparison between swept ($\ell = R_{TS}/4, \theta = 90°$) and axisymmetric ($\ell = 0$) interaction behavior near impingement at Mach 3.0 and $\alpha = 16°$.

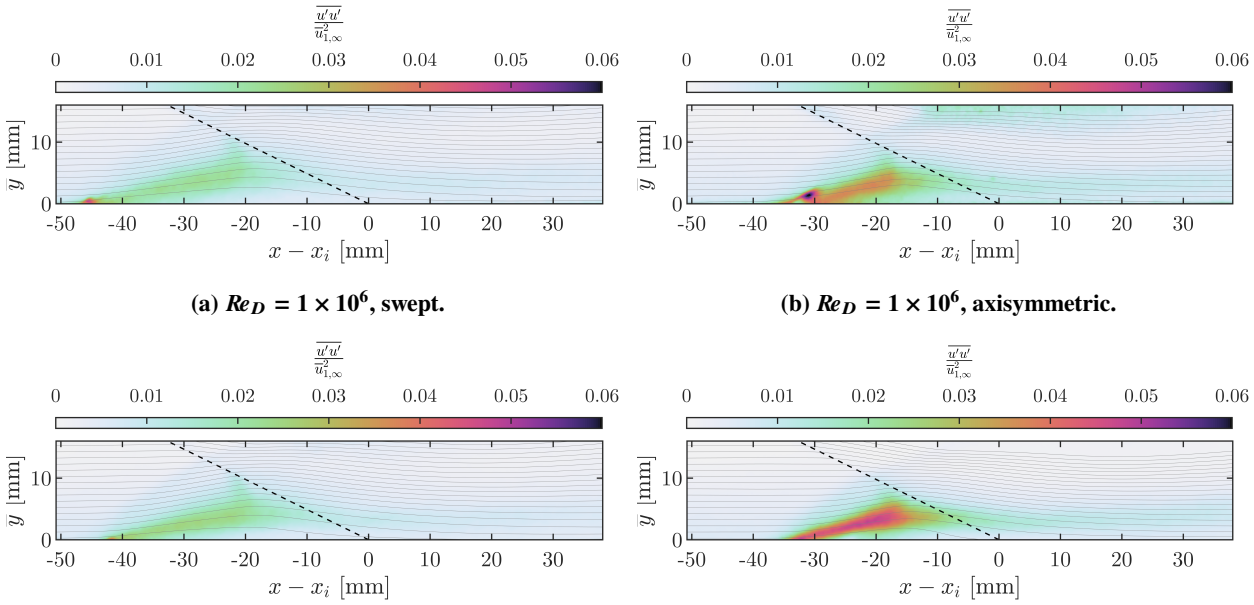

(a) $Re_D = 1 \times 10^6$, swept. **(b) $Re_D = 1 \times 10^6$, axisymmetric.**

(c) $Re_D = 2.25 \times 10^6$, swept. **(d) $Re_D = 2.25 \times 10^6$, axisymmetric.**

Fig. A24 Axial turbulence intensity comparison between swept ($\ell = R_{TS}/4, \theta = 90°$) and axisymmetric ($\ell = 0$) interaction behavior near impingement at Mach 3.0 and $\alpha = 16°$.

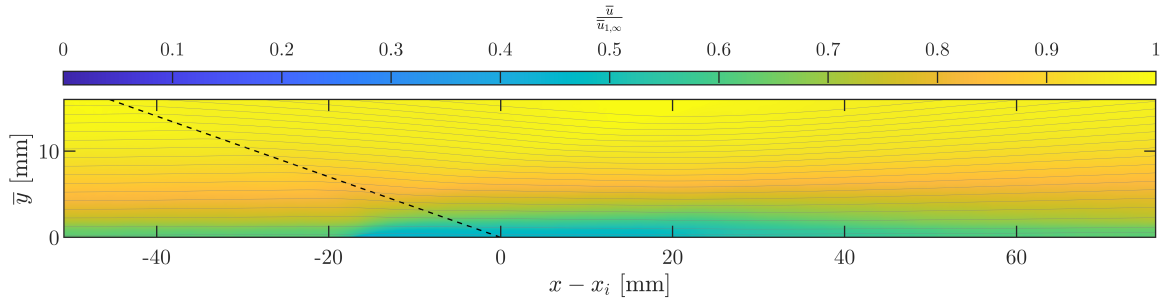

Fig. A25 Axial velocity fields in Mach 3.5 axisymmetric α = 10° interaction at $Re_D = 3 \times 10^6$.

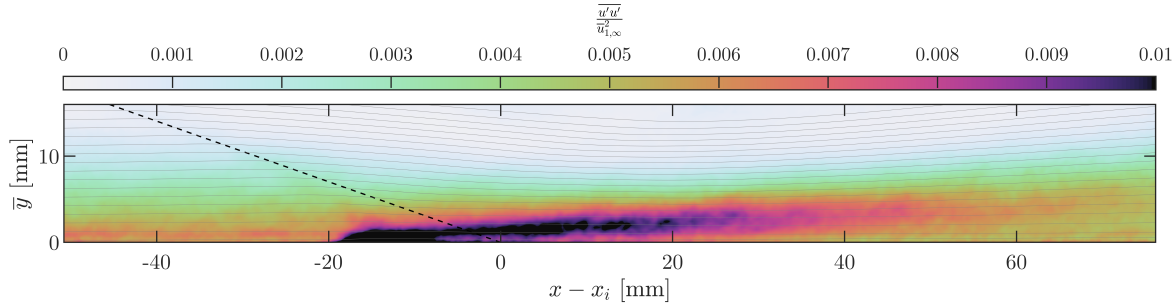

Fig. A26 Axial turbulence intensity fields in Mach 3.5 axisymmetric α = 10° interaction at $Re_D = 3 \times 10^6$.

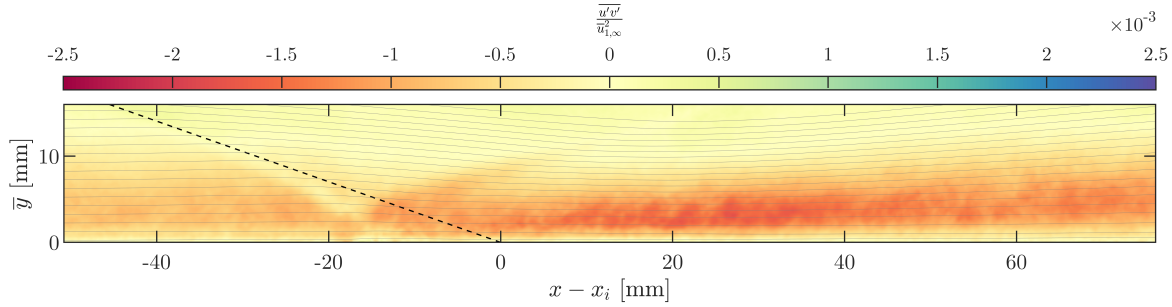

Fig. A27 Shear stress fields in Mach 3.5 axisymmetric α = 10° interaction at $Re_D = 3 \times 10^6$.

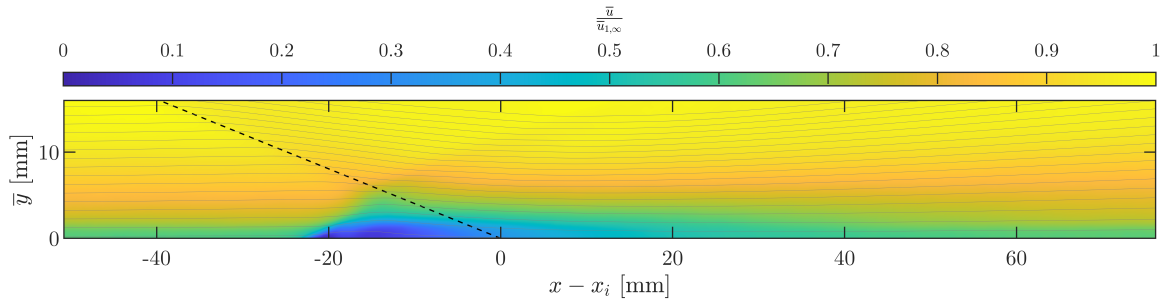

Fig. A28 Axial velocity fields in Mach 3.5 axisymmetric α = 13.5° interaction at $Re_D = 3 \times 10^6$.

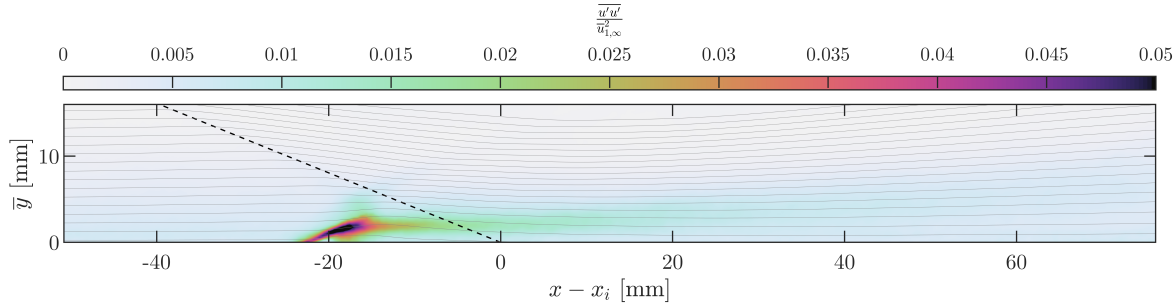

Fig. A29 Axial turbulence intensity fields in Mach 3.5 axisymmetric α = 13.5° interaction at $Re_D = 3 \times 10^6$.

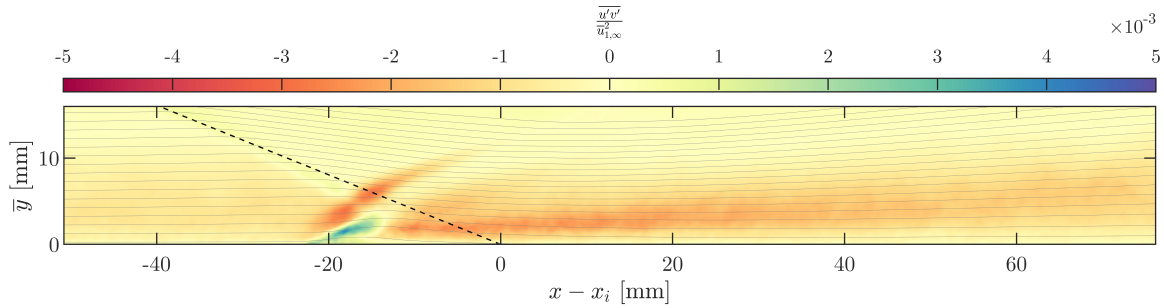

Fig. A30 Shear stress fields in Mach 3.5 axisymmetric α = 13.5° interaction at $Re_D = 3 \times 10^6$.

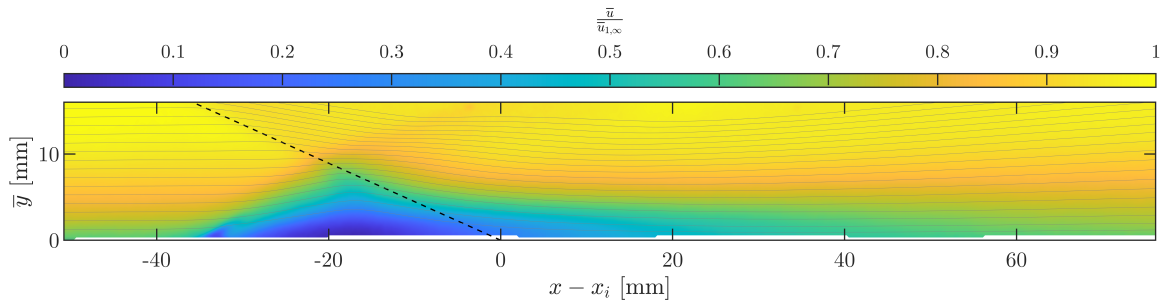

(a) $Re_D = 1.5 \times 10^6$

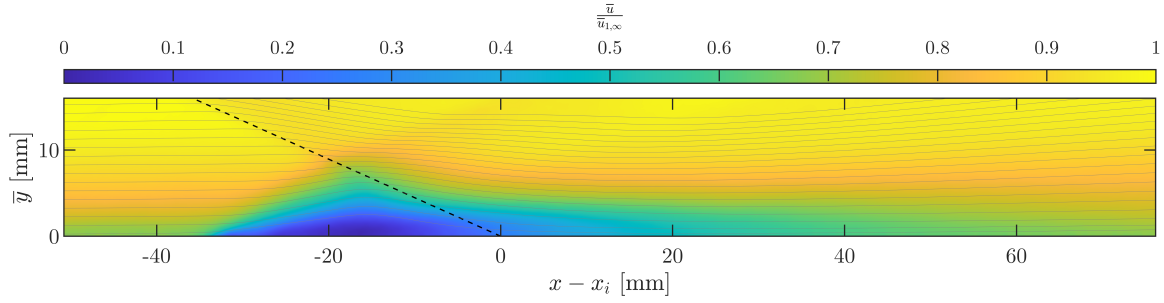

(b) $Re_D = 3 \times 10^6$

Fig. A31 Axial velocity fields in Mach 3.5 axisymmetric $\alpha = 16°$ interaction at the two Reynolds number conditions tested.

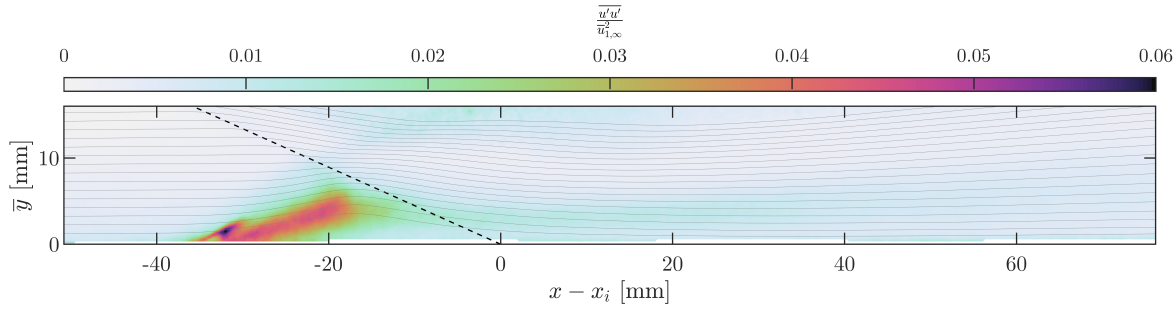

(a) $Re_D = 1.5 \times 10^6$

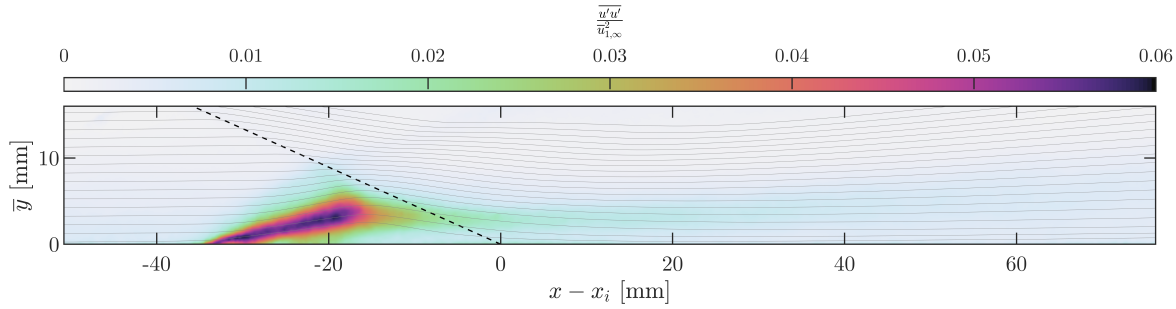

(b) $Re_D = 3 \times 10^6$

Fig. A32 Axial turbulence intensity fields in Mach 3.5 axisymmetric $\alpha = 16°$ interaction at the two Reynolds number conditions tested.

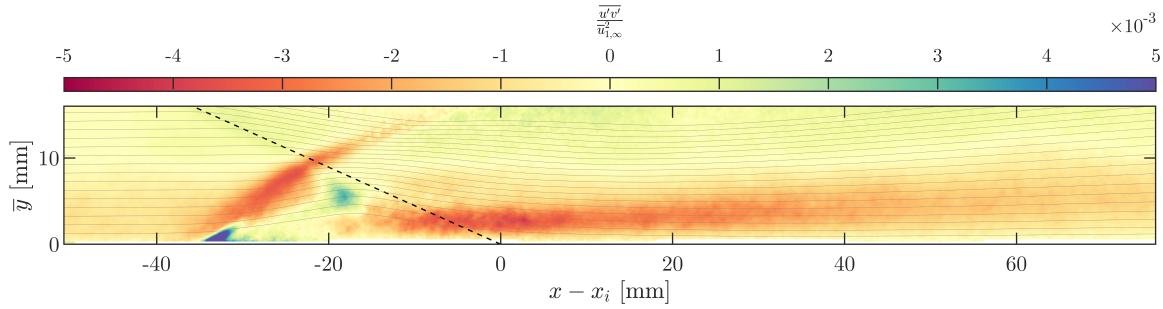

(a) $Re_D = 1.5 \times 10^6$

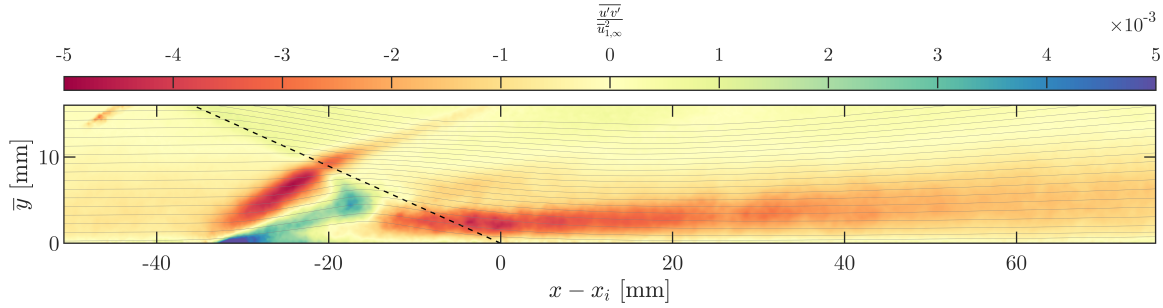

(b) $Re_D = 3 \times 10^6$

Fig. A33 Shear stress fields in Mach 3.5 axisymmetric $\alpha = 16°$ interaction at the two Reynolds number conditions tested.

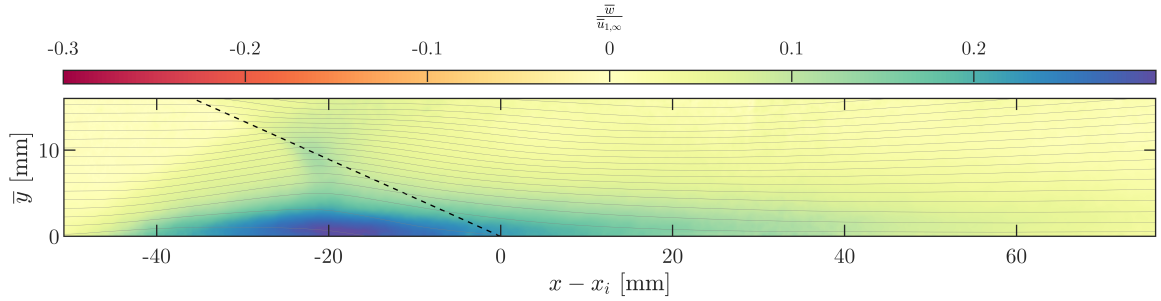

(a) $Re_D = 1.5 \times 10^6$

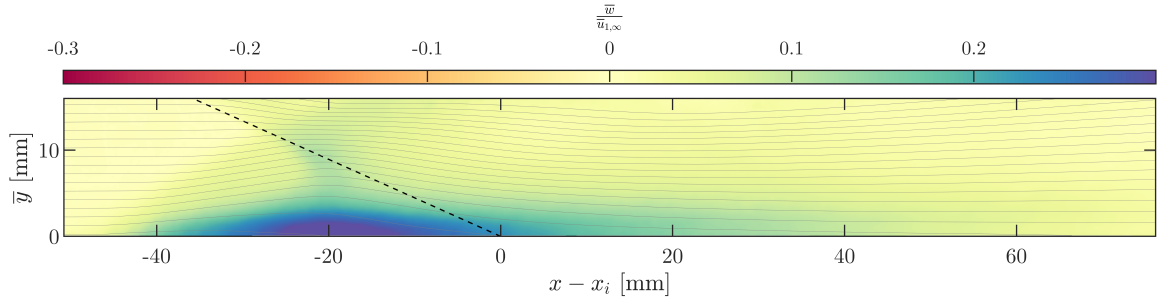

(b) $Re_D = 3 \times 10^6$

Fig. A34 Through-plane velocity fields in Mach 3.5, $\alpha = 16°$ swept ($\ell = R_{TS}/4, \theta = 90°$) interaction at the two Reynolds number conditions tested.

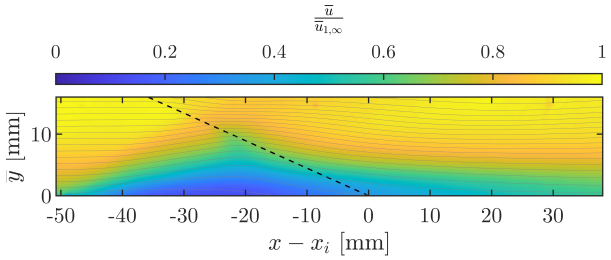

(a) $Re_D = 1.5 \times 10^6$, swept.

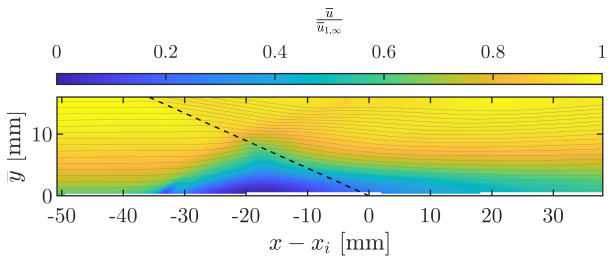

(b) $Re_D = 1.5 \times 10^6$, axisymmetric.

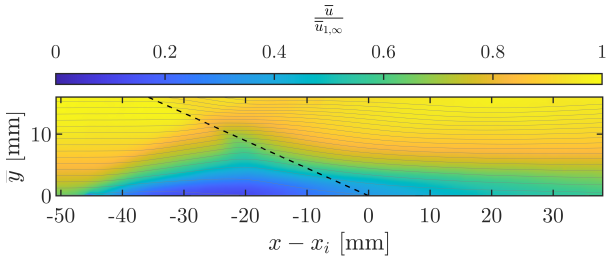

(c) $Re_D = 3 \times 10^6$, swept.

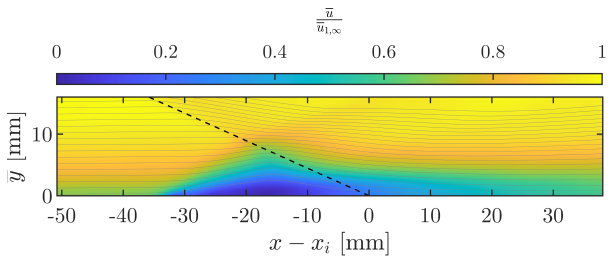

(d) $Re_D = 3 \times 10^6$, axisymmetric.

Fig. A35 Axial velocity field comparison between swept ($\ell = R_{TS}/4, \theta = 90°$) and axisymmetric ($\ell = 0$) interaction behavior near impingement at Mach 3.5 and $\alpha = 16°$.

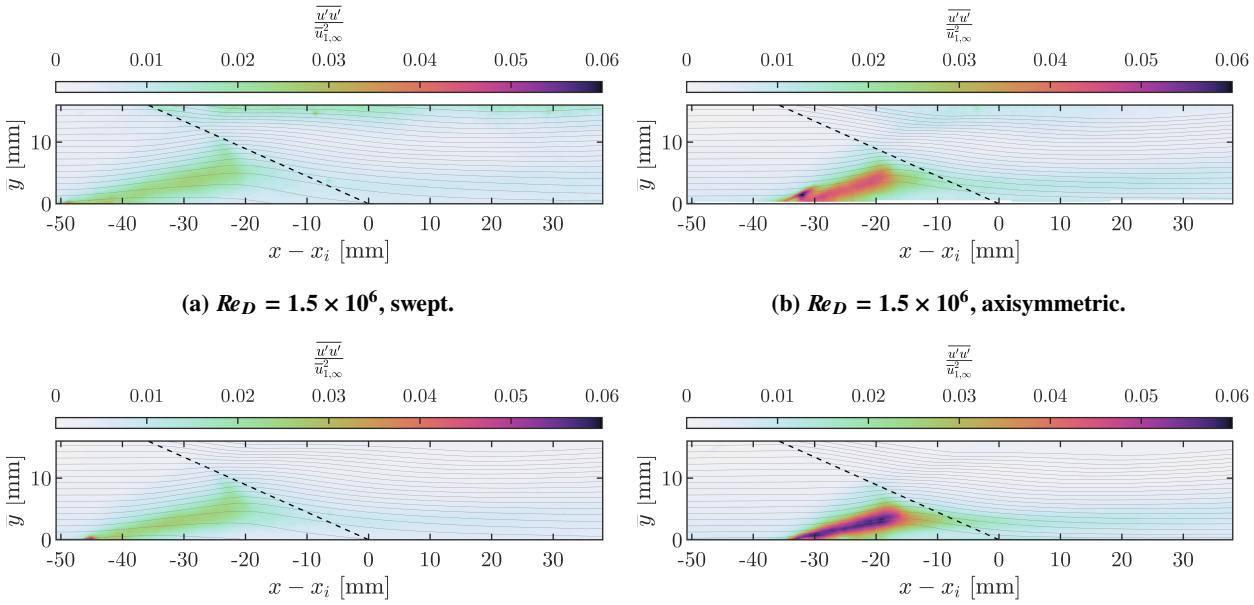

(a) $Re_D = 1.5 \times 10^6$, swept.

(b) $Re_D = 1.5 \times 10^6$, axisymmetric.

(c) $Re_D = 3 \times 10^6$, swept.

(d) $Re_D = 3 \times 10^6$, axisymmetric.

Fig. A36 Axial turbulence intensity comparison between swept ($\ell = R_{TS}/4, \theta = 90°$) and axisymmetric ($\ell = 0$) interaction behavior near impingement at Mach 3.5 and $\alpha = 16°$.